



저작자표시-비영리-변경금지 2.0 대한민국

이용자는 아래의 조건을 따르는 경우에 한하여 자유롭게

- 이 저작물을 복제, 배포, 전송, 전시, 공연 및 방송할 수 있습니다.

다음과 같은 조건을 따라야 합니다:



저작자표시. 귀하는 원저작자를 표시하여야 합니다.



비영리. 귀하는 이 저작물을 영리 목적으로 이용할 수 없습니다.



변경금지. 귀하는 이 저작물을 개작, 변형 또는 가공할 수 없습니다.

- 귀하는, 이 저작물의 재이용이나 배포의 경우, 이 저작물에 적용된 이용허락조건을 명확하게 나타내어야 합니다.
- 저작권자로부터 별도의 허가를 받으면 이러한 조건들은 적용되지 않습니다.

저작권법에 따른 이용자의 권리는 위의 내용에 의하여 영향을 받지 않습니다.

이것은 [이용허락규약\(Legal Code\)](#)을 이해하기 쉽게 요약한 것입니다.

[Disclaimer](#)

공학박사 학위논문

유기 활물질을 활용한 차세대
친환경 이차전지 개발에 관한 연구

Exploring redox-active organic materials for
the development of next-generation
rechargeable batteries

2023 년 2 월

서울대학교 대학원

재료공학부

김 지 현

유기 활물질을 활용한 차세대 친환경
이차전지 개발에 관한 연구

지도 교수 강 기 석

이 논문을 공학박사 학위논문으로 제출함

2023년 2 월

서울대학교 대학원

재료공학부

김 지 현

김지현의 공학박사 학위논문을 인준함

2023 년 2 월

위원장	<u>이 동 환</u>	(인)
부위원장	<u>강 기 석</u>	(인)
위원	<u>권 민 상</u>	(인)
위원	<u>박 찬 범</u>	(인)
위원	<u>김 천 중</u>	(인)

Abstract

Exploring redox-active organic materials for the development of next-generation rechargeable batteries

Jihyeon Kim

Department of Materials Science and Engineering

College of Engineering

The Graduate School

Seoul National University

A recent global initiative has pushed for the transition to renewable energy sources, such as solar, wind, and hydroelectric power under the global objective of carbon neutrality to combat the accelerating environmental problem along with the soaring energy demand. Due to the intermittent supply of renewable energy, these eco-friendly energy resources necessarily require an energy storage system, and lithium-ion batteries have been employed in a variety of applications ranging from portable devices to large-scale energy storage owing to their high energy density and cycling stability. For conventional transition metal (TM)-based battery systems, however, sustainability concerns have lately been highlighted due to the limited resources and associated price fluctuations, limitations in energy density due to

heavy weight, and difficulty in recycling. This apprehension led to the growing interest in alternative transition metal-free energy storage systems, and organic rechargeable batteries that utilize redox-active organic materials as an active material are regarded as promising candidates. Since organic materials are composed of earth-abundant elements such as carbon, hydrogen, oxygen, and nitrogen and generate far fewer greenhouse gases during production and recycling process, the system is sustainable and environmentally benign. In addition, chemical tunability is one of the major benefits that can considerably expand the utility of organic materials.

In this thesis, I propose several design strategies for the utilization of novel redox-active organic materials to develop eco-friendly and high-performance rechargeable organic batteries for next-generation energy storage systems. Moreover, a fundamental understanding of the reaction mechanism of ROMs is conducted using high-performed ROM and advanced analysis techniques for a leap forward in organic rechargeable batteries.

Chapter 2 introduces the molecular design strategy for developing a new redox-active organic material. Inspired by the similarity between energy transduction in biological systems and rechargeable battery systems, the well-known redox cofactor nicotinamide was introduced as redox-active material in rechargeable batteries. It was demonstrated that the intrinsically charged motif can serve as an active electrode in a lithium-ion battery system by anchoring the motif with the anions. This chapter demonstrates a novel approach for developing bio-

inspired energy storage systems by mimicking the redox-active motifs in the natural world.

Chapter 3 describes the molecular design strategy for the development of more environmentally friendly and high-performance organic rechargeable batteries. The all-organic symmetric cell is one of the enablers in environmental aspects since it utilizes identical organic material for both cathode and anode, hence reducing production costs. However, most symmetric batteries have low operating potential due to the small potential difference between oxidation and reduction reactions. In this respect, I proposed a new molecular design strategy, *p-n* fusion, to make bipolar-type materials with a large potential difference between reduction and oxidation. Due to the mutual perturbation of frontier molecular orbital energy level between *p*-type and *n*-type redox motifs, the fused molecule exhibited a higher highest occupied molecular orbital energy level than pristine *p*-type material and a lower lowest unoccupied molecular orbital energy level and it is demonstrated by first principle calculation. Based on the calculation result, a new PNZTA, which is a fused compound of phenazine and thianthrene, was synthesized and manifested successful bipolar activity. Moreover, the operating potential of the symmetric PNZTA cell was significantly greater than that of the individual phenazine and thianthrene cell.

Chapter 4 demonstrates the reaction mechanism of *p*-type redox-active materials using various advanced analysis techniques. *P*-type organic materials are an attractive candidate that has recently been in the spotlight due to their

comparable high voltage to conventional layer oxide-based systems. Since *p*-type organics undergo oxidation first, anions such as perchlorate, hexafluorophosphate, and bis(trifluoromethane)sulfonimide serve as guest ions instead of lithium or sodium ions for the charge compensation. Using multi-scale in situ analytical techniques, we elucidated for the first time the reaction mechanism of how bulky anions can be introduced into the electrode. Based on the combined structural and morphological monitoring during the reaction, the reaction process was revealed to be electrolytic dissolution, nucleation and growth, and anion migration. This fundamental study provides a guideline for the design of high-performance *p*-type organic rechargeable batteries.

This dissertation provides research insights for understanding organic battery systems as well as guidelines for the development of high-performance organic rechargeable batteries through an in-depth study of the design strategy and fundamental energy storage mechanism of organic rechargeable batteries.

Keywords: Rechargeable batteries, Organic rechargeable batteries, Redox-active organic materials, Electrochemistry, Organic chemistry

Student Number: 2017-22566

Contents

List of Tables	x
-----------------------------	---

List of Figures	xi
------------------------------	----

Chapter 1. Introduction	1
--------------------------------------	---

1.1 Research motivation and objectives	1
----------------------------------------------	---

1.2 Introduction to organic rechargeable batteries	3
----------------------------------------------------------	---

1.3 References	10
----------------------	----

Chapter 2. Exploitation of bio-inspired redox-active organic materials through molecular redesign	18
----------------------------------------------------------------------------------------------------------------	----

2.1 Research background	18
-------------------------------	----

2.2 Experimental method.....	22
------------------------------	----

2.2.1 Synthesis of nicotinamide biomimetics (mNAD-X)	22
------------------------------------------------------------	----

2.2.2 Electrochemical measurements	28
------------------------------------------	----

2.2.3 Computational details	28
-----------------------------------	----

2.2.4 Ex situ characterization	29
--------------------------------------	----

3.3.5 Electrochemical performance of PNZTA symmetric cell	96
3.4 Concluding remarks	102
3.5 References	104

Chapter 4. Investigation on fundamentals of *p*-type reaction

for developing high voltage organic batteries.....	113
4.1 Research background.....	113
4.2 Experimental method	117
4.2.1 Preparation and characterization of materials	117
4.2.2 Electrochemical measurements.....	117
4.2.3 In situ X-ray diffraction	118
4.2.4 In situ optical microscope	118
4.2.5 Characterizations.....	119
4.3 Results and discussions	120
4.3.1 Building system for the mechanism study	120
4.3.2 Crystallographic understanding during the <i>p</i> -type reaction	124
4.3.3 Real-time monitoring of morphological evolution	130
4.3.4 The presence of intermediate phases	142
4.3.5 Proposed mechanism of <i>p</i> -type redox reaction	151
4.4 Concluding remarks	163
4.5 References	164

Chapter 5. Conclusion 171

Chapter 6. Abstract in Korean 175

List of Tables

Table 2.1. Calculated bond length of mNAD⁺ and mNAD Li⁺ for all bonds. The hydrogen atoms bonded to the same carbon have the same C-H bond length. There are no remarkable changes in butyl group and carbon-proton bonds during Li-coupled reduction process 36

Table 2.2. Peak assignments in FTIR spectrum using DFT calculations. The reversible changes of the vibrational modes including the stretching of C=O bond and others within fingerprint region indicate that experimental results are compatible with computational calculations. 37

Table 3.1. Summary of X-ray crystallographic data. 89

Table 3.2. Performance of previous reported symmetric cells. The energy densities of the symmetric cells were estimated with respect to the weight of one electrode. 98

List of Figures

Figure 1.1. Comparative analysis of environmental and economic merits of redox-active organic materials. a) Comparison of the global warming potential (GWP) between common transition-metal-based active materials (blue bars) and organic materials (green bars). GWP100 denotes the relevant global warming impact of the specific product compared with the impact of CO₂ gas emissions over 100 years. The IPCC 2007 GWP100a method is used for LCO, whereas the IPCC 2013 GWP100a method is used for NCM622 and organic materials. Note that the life cycle assessment for the calculation of GWP100 excluded the end-of-life stage. The GWP of redox-active organic materials (orange bar) is an estimated value with the assumption that redox-active organic materials are synthesized in two to four steps from simple organic precursors and that little additional energy is needed during the synthesis process. b) Daily price of cobalt metal (blue), LCO (green), NCM622 (yellow), and NCM523 (red) over recent three years. Data sources: Shanghai Metal market, 2021 (for LCO, NCM622 and NCM523); London Metal Exchange, 2021 (for cobalt metal). Olefins: ethylene (C₂H₄), propylene (C₃H₆), Common aromatic compounds: benzene, toluene, mixed xylene. LCO, NCM523 and NCM622 refer to LiCoO₂, LiNi_{0.5}Co_{0.2}Mn_{0.3}O₂ and LiNi_{0.6}Mn_{0.2}Co_{0.2}O₂, respectively..... 7

Figure 1.2. Redox motifs in representative redox-active organic electrodes. Representative redox motifs that are commonly observed in redox-active organic materials in the literature. The blue and green colors indicate p-type and n-type

motifs, respectively. During the p-type and n-type redox reactions, charge compensation by anions and cations, respectively, in the electrolyte is generally required. 9

Figure 2.1. a) Reversible redox cycling of nicotinamide redox center in NAD(P)⁺ facilitates biological energy transduction which converts solar energy to ATP. b) In electrochemical energy storage, reversible lithium-coupled electron transfer can take place near the fixed nicotinamide redox motif of mNAD-X electrode 21

Figure 2.2. ¹H NMR (300 MHz, top) and ¹³C NMR (75 MHz, bottom) spectrum of mNAD-Cl in D₂O (*T* = 298 K)..... 25

Figure 2.3 ¹H NMR (300 MHz, top) and ¹³C NMR (75 MHz, bottom) spectrum of mNAD-I in D₂O (*T* = 298 K) 26

Figure 2.4 ¹H NMR (300 MHz, top) and ¹³C NMR (75 MHz, bottom) spectrum of [(mNAD)₂Bu]I₂ in D₂O (*T* = 298 K)..... 27

Figure 2.5. a) Molecular design strategy to mimic the redox center of NAD⁺ to utilize it as the active material of the battery electrode. b) Galvanostatic discharge/charge profile of mNAD-I/Li cell indicating reversible lithium-coupled electron transfer reactions. 32

Figure 2.6. a) DFT energies calculated for mNAD⁺ and various mNAD Li⁺ with different lithium ion sites. The mNAD Li⁺, in which lithium atom was inserted near C4 site, is energetically most stable compared to other structures. b) Molecular

structure of $mNAD^+$ and $mNAD Li^+$ which is reduced with lithium insertion, predicted from DFT calculations..... 38

Figure 2.7. a) Hirshfeld charge analysis for each atom of $mNAD^+$ and $mNAD Li^+$. b) The major bond length changes of $mNAD^+$ upon lithiation. c) Ex situ analysis of $mNAD-I$ at various states of charge in $mNAD-I/Li$ cell. FTIR spectra containing information of CO vibration. d) XPS spectra of O1s local scan: as-prepared state, discharged state to 1.9 V and recharged state to 2.8 V. 39

Figure 2.8. Calculated Hirshfeld charge of $mNAD^+$ and $mNAD Li^+$. The Hirshfeld charge of C4 was remarkably reduced, indicating the increment of the electron density, which may be attributed to the binding with lithium cation. 40

Figure 2.9. Full range spectra of ex situ FTIR from 500 cm^{-1} to 2000 cm^{-1} with peak assignments for each vibrational mode. The reversible changes during the discharge/charge indicate that lithiated structure was stabilized by conjugation from pyridinium to amide group..... 41

Figure 2.10. a) Electrochemical profile of $mNAD-X$ with various halides. As the size of the anion increases, the amount of lithium per each molecule that inserts and deinserts reversibly increases. b) Differential capacity (dQ/dV) curves of $mNAD-X/Li$ cells calculated from the data shown in Figure 2b. As the size of the anion decreases, the discharge potential increases 45

Figure 2.11. Electrochemical profile of mNAD-X with various halides. The theoretical specific capacity of mNAD-Cl, mNAD-Br and mNAD-I are 124.65, 103.48 and 87.59 mAh g⁻¹, respectively. 46

Figure 2.12. XRD patterns of powder mNAD-Cl, mNAD-Br and mNAD-I. 47

Figure 2.13. GITT curves of each NAD⁺-derivative (mNAD-Cl, mNAD-Br, and mNAD-I) from second to fourth steps. The smaller the size of the anion, the higher the thermodynamic reduction potential. 48

Figure 2.14. a) Molecular structure of Butyl-linked mNAD-I. b) Electrochemical profile of butyl-linked mNAD-I. it also showed reversible reaction with average voltage of 2.3 V. c) Enhanced cycle performance of butyl-linked mNAD-I compared to mNAD-I. 49

Figure 3.1. ¹H NMR (500 MHz, top) spectrum and ¹³C NMR (125 MHz, bottom) spectrum of PNZTA in CDCl₃ (*T* = 298 K)..... 64

Figure 3.2. Preventing shuttle effect of PNZTA through separator engineering. a, b) Charge/discharge curves of *p*-type reaction of PNZTA utilizing celgard separator (a) and nafion coated separator (b). Overcharging due to the shuttle effect was mitigated after using nafion coated separator. c, d) XPS survey scan results and surface images for Na metal anode after charging the PNZTA half cells using celgard separator(c) and nafion coated separator (d). e, f) Comparison of XPS narrow scan results of N 1s (e) and S 2p (f) spectra from the results of c) and d). In

the cell using only celgard separator, the nitrogen and sulfur which is originated from PNZTA was found in the metal surface resulting in the contamination of metal surface. However, after using nafion coated separator, sodium metal retained a clean pristine surface after charging and none of nitrogen and sulfur was found in the surface, indicating the suppression of PNZTA migration from cathode to anode.

..... 65

Figure 3.3. Molecular design strategy of PNZTA through the “*P*-linker-*N*” and “*P*-*N* fusion” of phenazine and thianthrene redox motifs. 70

Figure 3.4. Calculated HOMO and LUMO level of TA, PNZ and various fused molecules of those motifs. The Na/Na⁺ redox potential was set to -1.73 V versus AVS because the standard hydrogen electrode (SHE) is -4.44 V versus AVS and Na/Na⁺ is -2.71 V versus SHE. 71

Figure 3.5. Charge distribution calculation of PNZTA using natural population analysis. 76

Figure 3.6. The *p-n* fusion of DD and PNZ. a) Calculated molecular orbital energies (HOMO and LUMO) of DD, PNZ and various fused molecules of those motifs. The Na/Na⁺ redox potential was set to -1.73 V versus AVS because the SHE is -4.44 V versus AVS and Na/Na⁺ is -2.71 V versus SHE. b) Charge distribution calculation of PNZDD using natural population analysis..... 77

Figure 3.7. The *p-n* fusion of PTZ and PNZ. a) Calculated molecular orbital energies (HOMO and LUMO) of PTZ, PNZ and various fused molecules of those

motifs. b) Charge distribution calculation of PNZPTZ using natural population analysis.	78
Figure 3.8. Synthetic scheme for PNZTA.	79
Figure 3.9. CV curves of PNZ (blue), TA (orange), and PNZTA (green), which presents bipolar redox activity with widened potential gap in the fused material. dQ/dV curves of PNZ, TA, and PNZTA, corresponding to the sodium half-cell charge/discharge profile, are presented in the inset.	80
Figure 3.10. CV results of PNZ, TA and PNZTA in various electrolyte system. a) 0.1 M NaClO ₄ in MeCN, b) 0.1 M LiTFSI in MeCN	81
Figure 3.11. Galvanostatic charge/discharge profile and capacity retention curves of PNZ, TA, and PNZTA half-cell at a current density of C/5. a, c) The <i>n</i> -type redox reaction of PNZ and PNZTA. b,d) The <i>p</i> -type redox reaction of TA and PNZTA.	82
Figure 3.12. Solubility test for PNZ, TA and PNZTA. a) Powder solubility of PNZ, TA and PNZTA in DEGDEM solvent which was used in this paper b) Images of solvent after dissolving each material. PNZTA showed significantly low solubility than PNZ and TA.....	83
Figure 3.13. a) Expected reaction scheme for the <i>n</i> -type and <i>p</i> -type redox reaction and changes of the calculated charge distributions upon each reaction. b,c,d) Charge distribution calculations of PNZTA (b), PNZTA ⁻ (c), and PNZTA ⁺ (d) using natural population analysis. The numbers on each atom denotes the calculated atomic charges. The numbers under each molecule are the sum of atomic charges	

which corresponding to the phenazine motif (blue) and the thianthrene motif (orange), respectively. 84

Figure 3.14. The bond length changes of PNZTA upon reduction (that is *n*-type reaction, blue bar) and oxidation (that is *p*-type reaction, orange bar)..... 85

Figure 3.15. Investigation of redox mechanism for *n*-type redox reaction of PNZTA. a) Ex situ Na 1s, N 1s, and S 2p XPS spectra. b) Voltage-capacity profile of *n*-type reaction for PNZTA and corresponding FT-IR spectra. c) Side view of molecular structures of PNZTA and PNZTA⁻ with folding angle obtained by DFT calculation. d) Ex situ XRD patterns during the *n*-type redox reaction 90

Figure 3.16. Peak assignments for FTIR spectra..... 91

Figure 3.17. X-ray structure of PNZTA: a) top view and b) side view 92

Figure 3.18. Investigation of redox mechanism for *p*-type redox reaction of PNZTA. a) Ex situ Cl 2p, S 2p, and N 1s XPS spectra. b) Side view of molecular structures of PNZTA and PNZTA⁺ with folding angle, which showed significant conformational change. c) Voltage-capacity profile of *n*-type reaction for PNZTA and corresponding FT-IR spectra. d) Ex situ XRD patterns during the *p*-type redox reaction. 95

Figure 3.19. Electrochemical performance of the symmetric cell. (a) Comparison of charge–discharge curves of the battery using PNZ and TA as the cathode and anode, respectively, and that of the symmetric battery exploiting PNZTA as the active materials for both electrodes simultaneously. (b) Symmetric cell voltage and energy density plot of reported symmetric batteries utilizing inorganic (green) and

organic (yellowish-green) active materials. The energy density was calculated as the product of the voltage of the symmetric cell and the capacity based on the weight of one electrode. 99

Figure 3.20. Linear sweep voltammetry (LSV) curves of Na metal / 3.5 m NaClO₄ in DEGDME / SUS cell. 100

Figure 3.21. Capacity retentions of PNZTA symmetric cell after the activation cycle. 101

Figure 4.1. Electrochemical reaction of DMPZ in an aqueous system. a) Molecular structure and reaction formula of DMPZ. b) Photo image of DMPZ powder dispersed in aqueous electrolyte. c. Galvanostatic charge/discharge profile of DMPZ electrode in Zn cell at a current density of 10 mA g⁻¹. 122

Figure 4.2. Normalized UV-vis absorption spectra of (a) DMPZ and (b) [DMPZ⁺][ClO₄⁻] in various aqueous and non-aqueous solvent 123

Figure 4.3. Structural evolution of DMPZ during charge/discharge process. a. Voltage profile of DMPZ electrodes cycled at 10 mA g⁻¹ and corresponding summarized in situ XRD patterns. The displayed patterns were collected every 45 minutes. The peaks in the blue box are new peaks that evolved upon charging. b. The molecular and crystal structure of DMPZ and [DMPZ⁺][ClO₄⁻] determined by SC-XRD at room temperature and corresponding PXRD patterns calculated from the SC-XRD result. 127

Figure 4.4. In situ XRD patterns of DMPZ electrodes cycled under a current rate of 10 mA g⁻¹ and corresponding voltage profile. 128

Figure 4.5. a. PXRD pattern of the DMPZ electrode (top) and simulated PXRD pattern based on SC-XRD result of DMPZ obtained at room temperature (bottom).
b. PXRD pattern of the charged DMPZ electrode (top) and that of the electrode made with chemically synthesized [DMPZ⁺][ClO₄⁻] (bottom). c. Normalized charge/discharge profile of DMPZ electrode (blue) and [DMPZ⁺][ClO₄⁻] electrode (purple). d. PXRD pattern of the [DMPZ⁺][ClO₄⁻] electrode (top) and simulated PXRD pattern based on SC-XRD result of [DMPZ⁺][ClO₄⁻] obtained at room temperature (bottom)..... 129

Figure 4.6. Morphological change of DMPZ during *p*-type reaction and the presence of solvated intermediate. a. Schematic illustration of the in situ optical system. b. In situ optical microscopy images of DMPZ crystal during the galvanostatic charging, which demonstrate the surface reorganization of DMPZ. c-f. Ex situ SEM images of the DMPZ electrode at different states of charge during the first cycle; pristine electrode (c), charged electrode (d), and discharged electrode (e). f. Schematic illustration of rotating ring disk electrode with DMPZ deposited to the disk electrode and related reaction occurring at each electrode. g. Current response obtained in the rotating ring disk electrode experiment presented in Figure 3e with 0.2 M Zn(ClO₄)₂ H₂O electrolyte. The rotation rate of 1,000 rpm and a scan rate of 5 mV s⁻¹ were used. h. Schematic illustration of rotating ring disk electrode with [DMPZ⁺][ClO₄⁻] deposited to the disk electrode and related reaction occurring

at each electrode. i. Current response from ring electrode obtained in the rotating ring disk electrode experiment presented in Figure 4.6g with 0.2 M $\text{Zn}(\text{ClO}_4)_2 \text{H}_2\text{O}$ electrolyte. A pause for 5 minutes and a rotation for 3 minutes were repeated, and the rotation rpm was increased to 1000, 2000, and 3000 rpm..... 134

Figure 4.7. Raman spectra of DMPZ powder, $[\text{DMPZ}^+][\text{ClO}_4^-]$ powder and dark green phase grown on the crystalline DMPZ surface after charging in the homemade cell presented in Figure 3a with 1 M $\text{Zn}(\text{ClO}_4)_2 \text{H}_2\text{O}$ electrolyte. Raman spectra of the dark green phase is identical to that of the $[\text{DMPZ}^+][\text{ClO}_4^-]$ powder. 136

Figure 4.8. a,b. Optical microscope image of DMPZ crystal after deep charging ((a) for 24 hours and (b) for 15 hours) c. SEM images of DMPZ particle on the carbon tape with the size of hundred micrometers. d. SEM images of the charged DMPZ particle in 1 M $\text{Zn}(\text{ClO}_4)_2 \text{H}_2\text{O}$ electrolyte. 137

Figure 4.9. a. SEM image of DMPZ powder. b. Magnified SEM image of the DMPZ particle surface after 2 minutes of galvanostatic charging in 1 M $\text{Zn}(\text{ClO}_4)_2 \text{H}_2\text{O}$ electrolyte. c. SEM image of DMPZ powder after 5 hours of galvanostatic charging in 1 M $\text{Zn}(\text{ClO}_4)_2 \text{H}_2\text{O}$ electrolyte. d. EDS results in each point indicated in Figure S5b. EDS results demonstrate that the area marked in green color in Figure S6b is the charged DMPZ phase..... 138

Figure 4.10. Ex situ SEM images of DMPZ electrode at different states of charge during the first cycle in 1 M $\text{Zn}(\text{ClO}_4)_2 \text{H}_2\text{O}$ electrolyte. Note that scale bars in each image represent different lengths. Light green colored particles indicate DMPZ and

dark green colored particles indicate $[\text{DMPZ}^+][\text{ClO}_4^-]$ 139

Figure 4.11. Magnified SEM image of half discharged electrode after charge to 1.3 V vs. Zn^{2+}/Zn . DMPZ particles are located near the $[\text{DMPZ}^+][\text{ClO}_4^-]$ that is peeling off during the discharge..... 140

Figure 4.12. Ex situ SEM images of DMPZ electrode at different states of charge during the second cycle in 1 M $\text{Zn}(\text{ClO}_4)_2$ H_2O electrolyte. 141

Figure 4.13. a-c. RRDE experiment results in 0.2 M $\text{Zn}(\text{ClO}_4)_2$ H_2O electrolyte with various rotating rate. a. 1,000 rpm. b. 2,000 rpm. c. 3,000 rpm. d. The ratio of oxidation charge to reduction charge in each rotation rate. The oxidation and reduction charge was calculated by the integrating the positive and negative areas of the current-time curve of the linear sweep voltammetry of the disk electrode. 147

Figure 4.14. RRDE experiment results in 1 M $\text{Zn}(\text{ClO}_4)_2$ H_2O electrolyte with various rotating rate. a. 1,000 rpm. b. 2,000 rpm. c. 3,000 rpm. d. The ratio of oxidation charge to reduction charge in each rotation rate. 148

Figures 4.15. a. UV-vis absorption spectra of $[\text{DMPZ}^+][\text{ClO}_4^-]$ with various concentrations dissolved in water and b. corresponding Beer-Lambert calibration curve. Calculated solubility product (K_{sp}) based on the UV-vis absorption spectra is 5.176×10^{-6} 149

Figure 4.16. a. Schematic illustration of rotating ring disk electrode with $[\text{DMPZ}^+][\text{ClO}_4^-]$ deposited to the disk electrode and related reaction occurring at each electrode. b-d. Current response of RRDE experiment in 0.2 M $\text{Zn}(\text{ClO}_4)_2$

H₂O electrolyte with various rotating rate. b. 1,000 rpm. c. 2,000 rpm. d. 3,000 rpm. e. The ratio of oxidation charge to reduction charge in each rotation rate. 150

Figure 4.17. Proposed *p*-type redox mechanism of DMPZ. Schematic illustration of proposed *p*-type redox reaction for DMPZ. DMPZ at the particle surface undergoes electrolytic dissolution during the charging. Dissolved DMPZ⁺ is precipitated and forms [DMPZ⁺][ClO₄⁻] nuclei as it reaches its solubility limit near the surface. Precipitation facilitates additional dissolution of DMPZ⁺, enabling the continuous charging. The reaction proceeds as the [DMPZ⁺][ClO₄⁻] grows continuously. For the discharge process, the dissolution of [DMPZ⁺][ClO₄⁻] occurs first to produce the solvated DMPZ⁺ intermediates. This solvated DMPZ⁺ undergoes the solution mediated charge transfer reaction at the electrode and reduced DMPZ is immediately precipitated on the electrode. As the charge process, precipitation of DMPZ induces additional production of solvated DMPZ⁺, and the discharge reaction proceeds as the DMPZ nuclei grows. 156

Figure 4.18. a. Chronoamperograms of DMPZ charging at 1.06 V (vs. Zn²⁺/Zn) in 1 M Zn(ClO₄)₂ H₂O electrolyte. b. Current (**I**_m) and time (**t**_m) plots of four classical models and experimental data for DMPZ at 1.06 V. c. Chronoamperograms of [DMPZ⁺][ClO₄⁻] which is made by charging DMPZ to 1.3 V (vs. Zn²⁺/Zn) at 10 mA g⁻¹ discharging at 0.87 V (vs. Zn²⁺/Zn) in 1 M Zn(ClO₄)₂ H₂O electrolyte. d. Current (**I**_m) and time (**t**_m) plots of four classical models and experimental data for [DMPZ⁺][ClO₄⁻] at 0.87 V. e. Four classical models of electrochemical deposition..... 157

Figure 4.19. a, b. Current-overpotential profile of half charged electrode (a) and half discharged electrode (b) obtained through the linear sweep voltammetry to the positive and negative scan direction. The exchanged current was obtained based on the Butler-Volmer equation. If the overpotential η is small enough, the Butler-Volmer equation $i=i_0[\exp[-\alpha zF\eta/RT]-\exp[(1-\alpha)zF\eta/RT]$ to $i=-i_0F\eta/RT$ according to the Taylor series. i : current, i_0 : exchange current, α : charge transfer coefficient, z : number of electrons involved in the reaction, F : Farady constant, R : gas constant, T : absolute temperature, η : overpotential. Based on this simplified equation, the exchange current of oxidation and reduction reactions was obtained through the reciprocal of tangent slope at the point where overpotential is zero on each of the positive scan and negative scan curves. c. Average voltage of galvanostatic charge and discharge at various current rate. d. GITT profile of the DMPZ cell and its enlarged profile (inset) 159

Figure 4.20. a. Capacity retention at various current densities from 50 mA g⁻¹ to 1,000 mA g⁻¹. b. Charge/discharge profile of DMPZ electrode at various current densities. c. Capacity retention and coulombic efficiency of DMPZ electrode at 300 mA g⁻¹ 160

Figure 4.21. Charge/discharge profile of DMPZ electrode after prolonged cycles. 161

Figure 4.22. a. Ex situ XRD patterns of the electrode after 2nd and 200th charged and discharged. b. SEM images of the electrode after 200th charge and discharge 162

Chapter 1. Introduction

(The essence of this chapter has been published in *Nature Reviews Materials*.
Reproduced with permission from [Kim, J.[†], Y, Kim.[†], and J, Yoo.[†] *et al.*, *Nat. Rev. Mater.* **2022**, <https://doi.org/10.1038/s41578-022-00478-1>] Copyright (2022) Springer Nature)

1.1 Research motivation and objectives

The advancement of science and technology allows human beings to live a more enriched and convenient life, but at the expense of severe environmental pollution and global warming. The irresponsible use of fossil fuels is cited as the primary cause of environmental pollution, and thus, the world is on the verge of transitioning to sustainable energy under the global objective of carbon neutrality. The expansion of renewable energy resources, including solar and wind power, and the development of an energy storage system to store the generated electrical energy are the key enablers in achieving worldwide goals. Lithium-ion batteries have been developed as one of the promising energy storage systems during the last decades owing to their high energy and power densities.¹⁻³ However, conventional lithium-ion batteries rely on transition metal (TM)-based materials such as cobalt and nickel oxides of which the resources are scarce in coping with ever-increasing energy demand. In addition, because these materials not only emit a lot of greenhouse gases during the production process but is also even difficult to recycle,

it is neither sustainable nor environmentally benign.^{2,4-6}

In this regard, organic rechargeable batteries have emerged as a promising alternative for sustainable energy storage systems as they exploit transition-metal-free active materials, namely redox-active organic materials (ROMs) mostly comprising earth-abundant carbon, oxygen, hydrogen, and nitrogen.⁷⁻⁹ Since their introduction in the 1970s¹⁰⁻¹², organic rechargeable batteries have been consistently explored, but they have been overshadowed by the rapid development of based on TM-based materials. Nevertheless, continuous research has been conducted utilizing unique characteristics of organic materials differentiated from conventional TM-based inorganic materials, such as chemical tunability and natural extractability, and given the economic and environmental aspects, it is undoubtedly a fascinating system for the next generation.

The aim of this dissertation is to present various strategies to expand and develop the organic rechargeable battery system exploiting the unique advantages of organic materials, and to provide the new potential of organic batteries by revealing the reaction mechanism of the *p*-type organic materials that have the potential of high performance.

1.2 Introduction to organic rechargeable batteries

Organic rechargeable batteries are the system that exploits ROMs instead of the transition-metal oxide material in conventional lithium-ion batteries. Although TM-based materials have led the development of batteries owing to their high energy density and long cycle life, it is projected that these materials would face a supply problem due to their limited resource as the demand for energy storage systems increases rapidly. Moreover, considering that TM-based materials are responsible for nearly 30-50% of the global warming impact from the battery manufacturing process^{13,14}, replacing them with organic materials is a reasonable solution.

Figure 1.1a presents the global warming potential (GWP) values of the representative TM-based cathode materials and several mass-produced organic compounds such as methanol, olefins, and common aromatic.^{13,15,16} The GWP is an index that enables the comparison of the environmental impact of the production process of each material which refers to the amount of CO₂ or greenhouse gas equivalent to CO₂, generated per the production of 1 kg of a specific product.^{17,18} The figure clearly shows that the organic materials have substantially lower GWP values than that of TM-based materials. Although the GWP values have never been calculated for ROMs due to the absence of their mass production, a rough estimate is possible based on the values of organic precursors in Figure 1.1 and the fact that the complex industrial organic chemicals generally require two to four additional chemical processes from the precursors.^{19,20} The estimated GWP value of ROMs is

still significantly lower than those of TM-based materials. Moreover, given that the synthesis process for some organics can be further simplified, this conservative estimate is likely to be much lower.

Figure 1.1b presents the price fluctuation of commercial cathode materials and cobalt, a significant element of these materials, over the past three years. It clearly manifests that the prices of TM-based materials fluctuate by more than twofold even over the short period of time, and it is closely correlated with the price of raw metals such as cobalt. Since the cathode materials usually make up 40% of the total cell cost, their fluctuating price poses an unpredictable risk factor in the mass production of lithium-ion batteries.²¹ Additionally, the availability of TM resources, including nickel and cobalt, is limited, and competition with other industries that require a large amount of these metals, such as stainless-steel manufacturing industry, is unavoidable. Unlike these projections on transition-metal availability and associated costs, previous studies unequivocally suggest that the cost of redox-active organic materials would be under ~ 15 USD kg^{-1} when mass-produced through conventional organic synthetic routes.^{9,22} Owing to resourcefulness, eco-friendliness, and cost-effectiveness organic rechargeable batteries are considered promising alternatives to current lithium-ion batteries.

The redox activity of organic compounds is determined by the functional group in the material. And redox-active organic materials are commonly classified as *n*-type, *p*-type, or bipolar-type according to their capabilities to release electrons (oxidation) or receive electrons (reduction) in their neutral state during the

electrochemical reaction. Figure 1.2 presents representative redox motifs in redox-active organic materials. The *N*-type redox-active organic materials typically undergo reduction from their neutral state, forming negatively charged molecular states that can be reversed during oxidation. Carbonyl²³⁻²⁶, carboxylate^{27,28}, imine²⁹⁻³¹, nitrile³²⁻³⁴, and disulfide^{35,36} functional groups are representative *n*-type redox motifs. Most well-known organic materials inspired by biomaterials such as quinone and flavin derivatives are also classified as *n*-type. Conversely, the electrochemical reaction of *p*-type organic materials involves oxidation from their neutral state, forming positively charged molecular states reversibly. Ether³⁷, tertiary amine³⁸⁻⁴⁰, and thioether^{41,42} motifs can act as *p*-type motifs in organic materials. These *p*-type organic materials usually exhibit higher redox potential than *n*-type materials. Some organic compounds are known to undergo a bipolar-type reaction, exploiting redox moieties capable of both *n*-type and *p*-type behaviors. Nitroxide radicals^{43,44} and some conducting polymers⁴⁵⁻⁴⁷ are capable of bipolar redox activity.

The electrochemical properties of organic electrodes can be simply modified owing to the chemical tunability of organic materials.⁴⁸ For example, the specific capacity can be increased by eliminating the redox inactive part in molecules, and the redox potential also can be increased/decreased by attaching the electron withdrawing/donating functional group to adjust the frontier molecular orbital. In addition, polymerization or hybridization with carbon materials such as carbon nanotubes and graphene can enhance cycle stability. Moreover, organic

materials have versatile compatibility with both organic⁴⁸ and aqueous⁴⁹ electrolyte systems, as well as Na⁵⁰⁻⁵², K⁵³⁻⁵⁵, and even multivalent ion battery systems such as Zn^{56,57}, Ca^{58,59}, Mg⁶⁰, and Al^{61,62}. Therefore, organic materials are intensively studied in various applications utilizing their unique advantages.

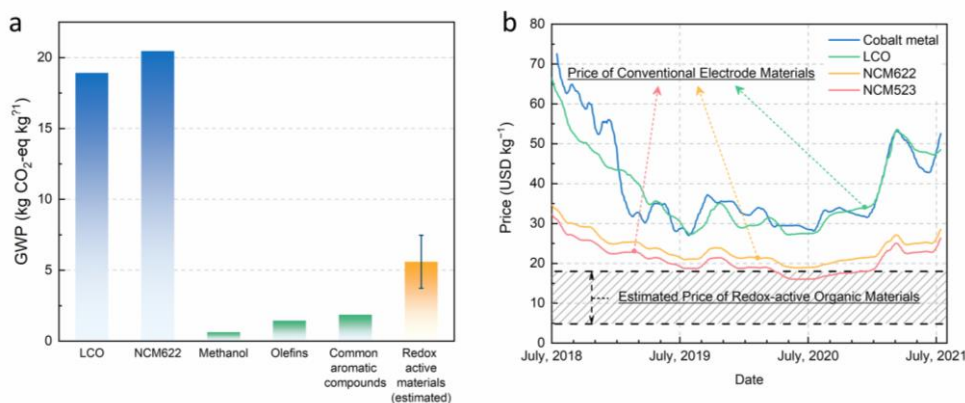


Figure 1.1. Comparative analysis of environmental and economic merits of redox-active organic materials. a) Comparison of the global warming potential (GWP) between common transition-metal-based active materials (blue bars) and organic materials (green bars). GWP100 denotes the relevant global warming impact of the specific product compared with the impact of CO₂ gas emissions over 100 years. The IPCC 2007 GWP100a method is used for LCO, whereas the IPCC 2013 GWP100a method is used for NCM622 and organic materials. Note that the life cycle assessment for the calculation of GWP100 excluded the end-of-life stage. The GWP of redox-active organic materials (orange bar) is an estimated value with the assumption that redox-active organic materials are synthesized in two to four steps from simple organic precursors and that little additional energy is needed during the synthesis process. b) Daily price of cobalt metal (blue), LCO (green), NCM622 (yellow), and NCM523 (red) over recent three years. Data sources: Shanghai Metal market, 2021 (for LCO, NCM622 and NCM523); London Metal

Exchange, 2021 (for cobalt metal). Olefins: ethylene (C₂H₄), propylene (C₃H₆),
Common aromatic compounds: benzene, toluene, mixed xylene. LCO, NCM523
and NCM622 refer to LiCoO₂, LiNi_{0.5}Co_{0.2}Mn_{0.3}O₂ and LiNi_{0.6}Mn_{0.2}Co_{0.2}O₂,
respectively.

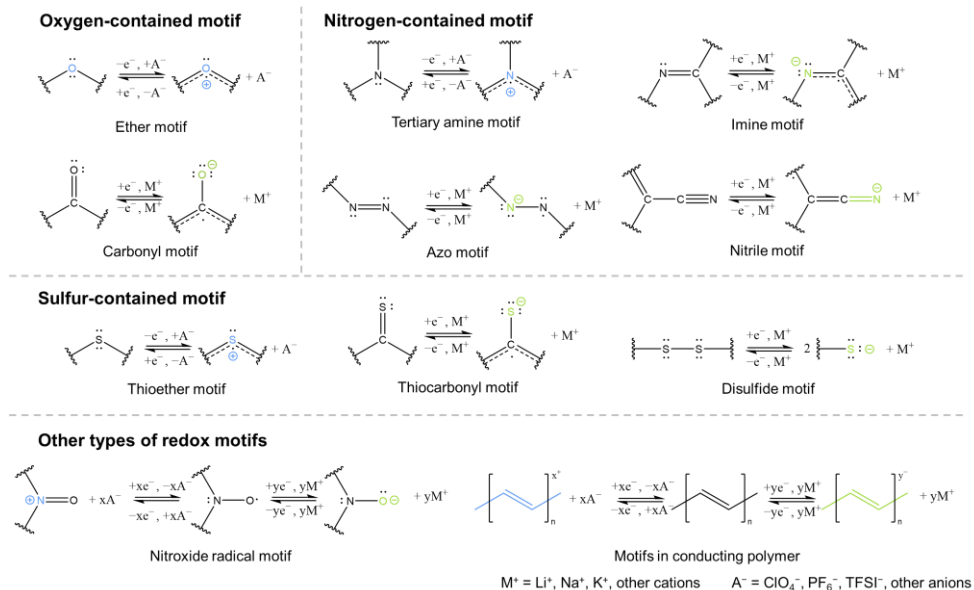


Figure 1.2. Redox motifs in representative redox-active organic electrodes.

Representative redox motifs that are commonly observed in redox-active organic materials in the literature. The blue and green colors indicate *p*-type and *n*-type motifs, respectively. During the *p*-type and *n*-type redox reactions, charge compensation by anions and cations, respectively, in the electrolyte is generally required.

1.3 References

- 1 Tarascon, J. M. & Armand, M. Issues and challenges facing rechargeable lithium batteries. *Nature* **414**, 359-367, (2001).
- 2 Dunn, B., Kamath, H. & Tarascon, J.-M. Electrical Energy Storage for the Grid: A Battery of Choices. *Science* **334**, 928-935, (2011).
- 3 Lewis, N. S. Research opportunities to advance solar energy utilization. *Science* **351**, aad1920, (2016).
- 4 Turcheniuk, K., Bondarev, D., Singhal, V. & Yushin, G. Ten years left to redesign lithium-ion batteries. *Nature* **559**, 467-470, (2018).
- 5 Harper, G. *et al.* Recycling lithium-ion batteries from electric vehicles. *Nature* **575**, 75-86, (2019).
- 6 Armand, M. & Tarascon, J. M. Building better batteries. *Nature* **451**, 652-657, (2008).
- 7 Poizot, P., Dolhem, F. & Gaubicher, J. Progress in all-organic rechargeable batteries using cationic and anionic configurations: Toward low-cost and greener storage solutions? *Curr. Opin. Electrochem.* **9**, 70-80, (2018).
- 8 Poizot, P. *et al.* Opportunities and Challenges for Organic Electrodes in Electrochemical Energy Storage. *Chem. Rev.* **120**, 6490-6557, (2020).
- 9 Lu, Y. & Chen, J. Prospects of organic electrode materials for practical lithium batteries. *Nat. Rev. Chem.* **4**, 127-142, (2020).
- 10 Alt, H., Binder, H., Köhling, A. & Sandstede, G. Investigation into the use of quinone compounds-for battery cathodes. *Electrochim. Acta* **17**, 873-

- 887, (1972).
- 11 Shirakawa, H., Louis, E. J., MacDiarmid, A. G., Chiang, C. K. & Heeger, A. J. Synthesis of electrically conducting organic polymers: halogen derivatives of polyacetylene, (CH). *J. Chem. Soc., Chem. Commun.*, 578-580, (1977).
 - 12 Ivory, D. M. *et al.* Highly conducting charge-transfer complexes of poly(p-phenylene). *J. Chem. Phys.* **71**, 1506-1507, (1979).
 - 13 Wang, C., Chen, B., Yu, Y., Wang, Y. & Zhang, W. Carbon footprint analysis of lithium ion secondary battery industry: two case studies from China. *J. Clean. Prod.* **163**, 241-251, (2017).
 - 14 Ambrose, H. & Kendall, A. Effects of battery chemistry and performance on the life cycle greenhouse gas intensity of electric mobility. *Transp. Res. D Trans. Environ* **47**, 182-194, (2016).
 - 15 Sun, X., Luo, X., Zhang, Z., Meng, F. & Yang, J. Life cycle assessment of lithium nickel cobalt manganese oxide (NCM) batteries for electric passenger vehicles. *J. Clean. Prod.* **273**, 123006, (2020).
 - 16 Rosental, M., Fröhlich, T. & Liebich, A. Life Cycle Assessment of Carbon Capture and Utilization for the Production of Large Volume Organic Chemicals. *Frontiers in Climate* **2**, (2020).
 - 17 Stocker, T. F. *et al.* Climate Change 2013: The physical science basis. contribution of working group I to the fifth assessment report of IPCC the intergovernmental panel on climate change. (2014).

- 18 Larcher, D. & Tarascon, J. M. Towards greener and more sustainable batteries for electrical energy storage. *Nat. Chem.* **7**, 19-29, (2015).
- 19 Wernet, G., Conradt, S., Isenring, H. P., Jiménez-González, C. & Hungerbühler, K. Life cycle assessment of fine chemical production: a case study of pharmaceutical synthesis. *Int. J. Life Cycle Assess.* **15**, 294-303, (2010).
- 20 Wernet, G., Mutel, C., Hellweg, S. & Hungerbühler, K. The Environmental Importance of Energy Use in Chemical Production. *J. Ind. Ecol.* **15**, 96-107, (2011).
- 21 Wentker, M. G. M. L. J. A. B.-U. A. t. L.-I. B. C. M. w. a. F. o. C. A. M. A Bottom-Up Approach to Lithium-Ion Battery Cost Modeling with a Focus on Cathode Active Materials. *Energies* **12**. (2019).
- 22 Yang, Z. *et al.* Alkaline Benzoquinone Aqueous Flow Battery for Large-Scale Storage of Electrical Energy. *Adv. Energy Mater.* **8**, 1702056, (2018).
- 23 Williams, D. L., Byrne, J. J. & Driscoll, J. S. A High Energy Density Lithium/Dichloroisocyanuric Acid Battery System. *J. Electrochem. Soc.* **116**, 2, (1969).
- 24 Liang, Y. *et al.* Universal quinone electrodes for long cycle life aqueous rechargeable batteries. *Nat. Mater.* **16**, 841-848, (2017).
- 25 Chen, H. *et al.* From Biomass to a Renewable LiXC6O6 Organic Electrode for Sustainable Li-Ion Batteries. *ChemSusChem* **1**, 348-355, (2008).
- 26 Lee, M. *et al.* High-performance sodium–organic battery by realizing four-

- sodium storage in disodium rhodizonate. *Nat. Energy* **2**, 861-868, (2017).
- 27 Armand, M. *et al.* Conjugated dicarboxylate anodes for Li-ion batteries. *Nat. Mater.* **8**, 120-125, (2009).
- 28 Jouhara, A. *et al.* Raising the redox potential in carboxyphenolate-based positive organic materials via cation substitution. *Nat. Commun.* **9**, 4401, (2018).
- 29 Lee, M. *et al.* Redox Cofactor from Biological Energy Transduction as Molecularly Tunable Energy-Storage Compound. *Angew. Chem. Int. Ed.* **52**, 8322-8328, (2013).
- 30 Peng, C. *et al.* Reversible multi-electron redox chemistry of π -conjugated N-containing heteroaromatic molecule-based organic cathodes. *Nat. Energy* **2**, 17074, (2017).
- 31 Schon, T. B., Tilley, A. J., Bridges, C. R., Miltenburg, M. B. & Seferos, D. S. Bio-Derived Polymers for Sustainable Lithium-Ion Batteries. *Adv. Funct. Mater.* **26**, 6896-6903, (2016).
- 32 Fujihara, Y. *et al.* Electrical Conductivity-Relay between Organic Charge-Transfer and Radical Salts toward Conductive Additive-Free Rechargeable Battery. *ACS Appl. Mater. Interfaces* **12**, 25748-25755, (2020).
- 33 Hanyu, Y. & Honma, I. Rechargeable quasi-solid state lithium battery with organic crystalline cathode. *Sci. Rep.* **2**, 453, (2012).
- 34 Häupler, B. *et al.* PolyTCAQ in organic batteries: enhanced capacity at constant cell potential using two-electron-redox-reactions. *J. Mater. Chem.*

- A **2**, 8999-9001, (2014).
- 35 Visco, S. J. & DeJonghe, L. C. Ionic Conductivity of Organosulfur Melts for Advanced Storage Electrodes. *J. Electrochem. Soc.* **135**, 2905-2909, (1988).
- 36 Zhou, J. *et al.* Selenium-Doped Cathodes for Lithium–Organosulfur Batteries with Greatly Improved Volumetric Capacity and Coulombic Efficiency. *Adv. Mater.* **29**, 1701294, (2017).
- 37 Lee, S. *et al.* Charge-transfer complexes for high-power organic rechargeable batteries. *Energy Storage Mater.* **20**, 462-469, (2019).
- 38 Lee, M. *et al.* Multi-electron redox phenazine for ready-to-charge organic batteries. *Green Chem.* **19**, 2980-2985, (2017).
- 39 Dai, G. *et al.* Manipulation of conjugation to stabilize N redox-active centers for the design of high-voltage organic battery cathode. *Energy Storage Mater.* **16**, 236-242, (2019).
- 40 Peterson, B. M., Gannett, C. N., Melecio-Zambrano, L., Fors, B. P. & Abruña, H. Effect of Structural Ordering on the Charge Storage Mechanism of p-Type Organic Electrode Materials. *ACS Appl. Mater. Interfaces* **13**, 7135-7141, (2021).
- 41 Speer, M. E. *et al.* Thianthrene-functionalized polynorbornenes as high-voltage materials for organic cathode-based dual-ion batteries. *Chem. Commun.* **51**, 15261-15264, (2015).
- 42 Wild, A., Strumpf, M., Häupler, B., Hager, M. D. & Schubert, U. S. All-

- Organic Battery Composed of Thianthrene- and TCAQ-Based Polymers.
Adv. Energy Mater. **7**, 1601415, (2017).
- 43 Nakahara, K. *et al.* Rechargeable batteries with organic radical cathodes.
Chem. Phys. Lett. **359**, 351-354, (2002).
- 44 Wang, S., Li, F., Easley, A. D. & Lutkenhaus, J. L. Real-time insight into
the doping mechanism of redox-active organic radical polymers. *Nat.*
Mater. **18**, 69-75, (2019).
- 45 Nigrey, P. J., MacInnes, D., Nairns, D. P., MacDiarmid, A. G. & Heeger,
A. J. Lightweight Rechargeable Storage Batteries Using Polyacetylene,
(CH)_x as the Cathode-Active Material. *J. Electrochem. Soc.* **128**, 1651-
1654, (1981).
- 46 Kaneto, K., Yoshino, K. & Inuishi, Y. Characteristics of Polythiophene
Battery. *Jpn. J. Appl. Phys.* **22**, L567-L568, (1983).
- 47 MacDiarmid, A. G., Yang, L. S., Huang, W. S. & Humphrey, B. D.
Polyaniline: Electrochemistry and application to rechargeable batteries.
Synth. Met. **18**, 393-398, (1987).
- 48 Lee, S. *et al.* Recent Progress in Organic Electrodes for Li and Na
Rechargeable Batteries. *Adv. Mater.* **30**, 1704682, (2018).
- 49 Han, C., Zhu, J., Zhi, C. & Li, H. The rise of aqueous rechargeable
batteries with organic electrode materials. *J. Mater. Chem. A* **8**, 15479-
15512, (2020).
- 50 Zhao, Q., Lu, Y. & Chen, J. Advanced Organic Electrode Materials for

- Rechargeable Sodium-Ion Batteries. *Adv. Energy Mater.* **7**, 1601792, (2017).
- 51 Xu, Y., Zhou, M. & Lei, Y. Organic materials for rechargeable sodium-ion batteries. *Materials Today* **21**, 60-78, (2018).
- 52 Luo, C. *et al.* Reversible Redox Chemistry of Azo Compounds for Sodium-Ion Batteries. *Angew. Chem. Int. Ed.* **57**, 2879-2883, (2018).
- 53 Zhang, W., Huang, W. & Zhang, Q. Organic Materials as Electrodes in Potassium-Ion Batteries. *Chem. Eur. J.* **27**, 6131-6144, (2021).
- 54 Liang, Y. *et al.* An Organic Anode for High Temperature Potassium-Ion Batteries. *Adv. Energy Mater.* **9**, 1802986, (2019).
- 55 Tang, M. *et al.* An organic cathode with high capacities for fast-charge potassium-ion batteries. *J. Mater. Chem. A* **7**, 486-492, (2019).
- 56 Yang, B., Ma, Y., Bin, D., Lu, H. & Xia, Y. Ultralong-Life Cathode for Aqueous Zinc-Organic Batteries via Pouring 9,10-Phenanthraquinone into Active Carbon. *ACS Appl. Mater. Interfaces* **13**, 58818-58826, (2021).
- 57 Xu, S., Sun, M., Wang, Q. & Wang, C. Recent progress in organic electrodes for zinc-ion batteries. *J. Semicond.* **41**, 091704, (2020).
- 58 Han, C., Li, H., Li, Y., Zhu, J. & Zhi, C. Proton-assisted calcium-ion storage in aromatic organic molecular crystal with coplanar stacked structure. *Nat. Commun.* **12**, 2400, (2021).
- 59 Gheyhani, S. *et al.* An Aqueous Ca-Ion Battery. *Adv. Sci.* **4**, 1700465, (2017).

- 60 Dong, H. *et al.* High-power Mg batteries enabled by heterogeneous enolization redox chemistry and weakly coordinating electrolytes. *Nat. Energy* **5**, 1043-1050, (2020).
- 61 Kim, D. J. *et al.* Rechargeable aluminium organic batteries. *Nat. Energy* **4**, 51-59, (2019).
- 62 Yoo, D.-J., Heeney, M., Glöcklhofer, F. & Choi, J. W. Tetradiketone macrocycle for divalent aluminium ion batteries. *Nat. Commun.* **12**, 2386, (2021).

Chapter 2. Exploitation of bio-inspired redox active organic materials through molecular redesign

(The essence of this chapter has been published in *Angewandte Chemie International Edition*. Reproduced with permission from [Kim, J.[†], and Ko, S.[†] *et al.*, *Angew. Chem. int. Ed.* **2019**, 58, 16764] Copyright (2019) WILEY-VCH)

2.1 Research background

Rising concerns on sustainability have brought great interest for eco-friendly energy storage solutions and motivated searching for sustainable electrode chemistry for lithium-ion batteries (LIBs), most widely-adopted portable power sources.¹ Organic compounds, which are derived from biomass or naturally abundant resources, are attractive electrode candidates for LIBs owing to their minimal environmental footprint.² The chemical tunability of organic materials can additionally offer a design flexibility required for electrodes in various types of rechargeable batteries.³ In particular, exploiting redox-active molecules in biological energy transduction procedures, which are believed to have been optimized over many years of evolution, is an appealing approach to green energy storage combined with the demonstrated efficiency.^{3,4} Previous studies reported that biological energy transductions share many aspects in common with rechargeable battery chemistry in underlying redox mechanism with respect to unidirectional transportation of charged ions (H^+ or Li^+) and electrons to a redox-

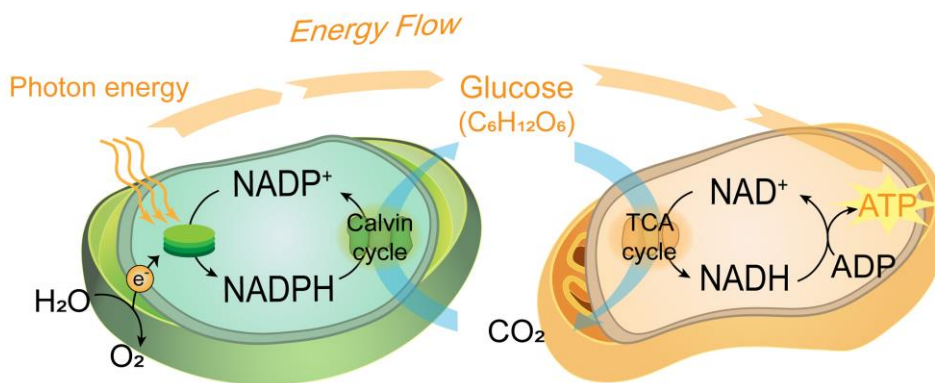
active center, which results in reversible energy storage.^{3,5} This analogy suggests a potential feasibility for exploiting new redox center from biological reactions to energy storage in rechargeable batteries. Flavin cofactors, for example, have been demonstrated as energy storage materials owing to their redox-active pteridine center, which enables reversible electron transfer.⁶ Considering the variety of biomolecules and derivatives, exploring bio-derived organic redox centers is thus expected to offer unexplored opportunities to develop new sustainable electrode chemistry for rechargeable battery system or devising a novel biomimetic artificial energy storage solution.

Nicotinamide adenine dinucleotide (nicotinamide cofactor) is one of the most well-known redox cofactors present in living cells. The redox-active NAD^+ motif is involved in over 80 % of all bio-transformations and electron-transfer reactions in natural systems by carrying charged ions and electrons from one reaction to another.⁷ For example, the redox cycle of the NAD^+ motif mediates multi-step transfer of energy and electrons from plant cell stroma through the mitochondrial matrix (Figure 2.1a).⁸ The versatility of NAD^+ motif may present promises in its electrochemical activity in other energy storage systems such as LIBs. Nevertheless, the exploration of its applicability as an electrode in conventional LIB setup is not trivial, since its charged state (NAD^+) and the dissolved nature are not compatible with the electrode fabrication requirements, where active compounds are generally in neutral state and ready for process into solid electrode. While significant portion of the energy carrying molecules are in

charged states and/or dissolved states in the biocells, a general fixation strategy would aid in expediting the exploration of these bio redox molecules.

Herein, inspired by versatile redox activity of nicotinamide cofactor, we attempt to investigate its potential applicability as an electrode material for LIBs, and propose a general route to anchor the charged/dissolved NAD^+ motif into the solid state without compensating for its intrinsic redox activity (Figure [2.1b](#)). To exploit the redox reaction of NAD^+ motif in LIBs, nicotinamide cofactor was modified into a simple structure bearing the redox-active part to produce nicotinamide analogue (mNAD^+). The charged mNAD^+ were crystallized using counter anions such as I^- , Br^- , and Cl^- , resulting in a neutral and solid-state powder. It is demonstrated that these NAD^+ -derivatives are capable of reversibly facilitating lithium-coupled electron transfer in solid electrode form, exhibiting the intrinsic redox capability of NAD^+ .

a) Biological energy transduction



b) Electrochemical energy storage

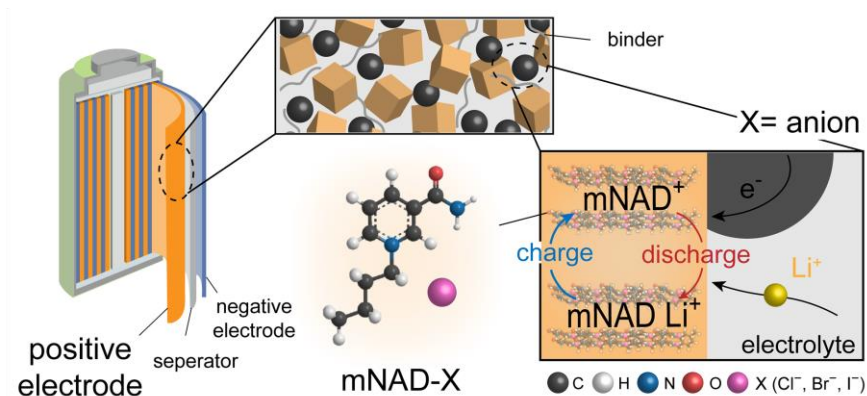


Figure 2.1. a) Reversible redox cycling of nicotinamide redox center in NAD(P)^+ facilitates biological energy transduction which converts solar energy to ATP. b) In electrochemical energy storage, reversible lithium-coupled electron transfer can take place near the fixed nicotinamide redox motif of mNAD-X electrode.

2.2 Experimental method

2.2.1 Synthesis of nicotinamide biomimetics (mNAD-X)

General Considerations: All reagents were obtained from commercial suppliers and used as received unless otherwise noted. The compound 1-butyl-3-carbamoylpyridinium bromide (mNAD-Br)⁹ was prepared according to literature procedure.

Physical Measurements: ¹H NMR and ¹³C NMR spectra were recorded on a 300 MHz Bruker Advance DPX-300. Chemical shifts are referenced to the residual solvent peaks. Elemental analysis was performed by a Perkin Elmer 2400 Series II CHNS/O Analyzer. FTIR spectra were recorded on a Perkin Elmer Spectrum Two FTIR Spectrometer.

1-Butyl-3-carbamoylpyridinium chloride (mNAD-Cl): This compound was prepared by adapting the reported procedure,¹⁰ for which only the m.p. of the product was reported. We thus provide detailed synthetic protocol, along with full characterization data here (Figure 2.2). A DMF (10 mL) solution of nicotinamide (1.98 g, 16.2 mmol) and 1-chlorobutane (1.80 mL, 17.1 mmol) was heated at 130 °C for 20 h, and allowed to cool to r.t. A portion of diethyl ether (20 mL) was added to induce precipitation. Filtration followed by washing with diethyl ether (20 mL) and DCM (20 mL) afforded product with nicotinamide impurity. After recrystallization from hot EtOH (6 mL), pure product was obtained as a white crystal (1.29 g, 6.02 mmol, yield = 37%). ¹H NMR (300 MHz, D₂O, 298 K): δ 9.39 (s, 1H), 9.12 (d, *J* = 6.1 Hz, 1H), 8.96 (d, *J* = 8.2 Hz, 1H), 8.27 (dd, *J* = 7.9, 6.3 Hz,

1H), 4.77 (t, $J = 7.5$ Hz, 2H), 2.08 (m, 2H), 1.43 (m, 2H), 0.98 (t, $J = 7.4$ Hz, 3H). ^{13}C NMR (75 MHz, D_2O , 298 K): δ 165.80, 146.60, 144.23, 143.88, 133.85, 128.47, 62.38, 32.62, 18.81, 12.79. FT-IR (ATR, cm^{-1}): 3241, 3057, 2963, 2875, 2792, 1698, 1651, 1588, 1512, 1445, 1405, 1326, 1207, 1146, 805, 682, 654. Anal. Calcd for $\text{C}_{10}\text{H}_{15}\text{ClN}_2\text{O}$: C, 55.95; H, 7.04; N, 13.05. Found: C, 55.81; H, 7.10; N, 12.97.

1-Butyl-3-carbamoylpyridinium iodide (mNAD-I): This compound was reported previously,¹¹ but no spectroscopic data is available in the literature. We thus report our synthetic procedure and full characterization data here (Figure 2.3). To a stirred MeCN solution (40 mL) of nicotinamide (2.00 g, 16.4 mmol) was added 1-iodobutane (2.00 mL, 17.6 mmol). The mixture was heated at reflux for 20 h, and allowed to cool to r.t. A portion of diethyl ether (100 mL) was added to induce precipitation of the product, which was isolated by filtration. After washing with diethyl ether (20 mL \times 3), the product was obtained as a light-yellow powder (4.18 g, 13.7 mmol, yield = 83%). ^1H NMR (300 MHz, D_2O , 298 K): δ 9.36 (s, 1H), 9.08 (d, $J = 6.1$ Hz, 1H), 8.93 (d, $J = 8.2$ Hz, 1H), 8.24 (dd, $J = 7.9, 6.3$ Hz, 1H), 4.74 (t, $J = 7.5$ Hz, 2H), 2.08 (m, 2H), 1.41 (m, 2H), 0.98 (t, $J = 7.4$ Hz, 3H). ^{13}C NMR (75 MHz, D_2O , 298 K): δ 165.86, 146.55, 144.28, 143.87, 133.88, 128.43, 62.40, 32.57, 18.79, 12.74. FT-IR (ATR, cm^{-1}): 3325, 3152, 3015, 1678, 1640, 1583, 1506, 1460, 1447, 1391, 1339, 1213, 1147, 1115, 780, 739, 662. Anal. Calcd for $\text{C}_{10}\text{H}_{15}\text{IN}_2\text{O}$: C, 39.23; H, 4.94; N, 9.15. Found: C, 39.24; H, 4.81; N, 8.89.

1,1'-(Butane-1,4-diyl)bis(3-carbamoylpyridinium) diiodide

[(mNAD)₂Bu]I₂: A DMF (5 mL) solution of nicotinamide (0.908 g, 7.44 mmol) and 1,4-diiodobutane (0.46 mL, 3.49 mmol) was heated at 130 °C for 20 h, and cooled down to r.t. A portion of diethyl ether (20 mL) was added to induce precipitation of the product. After washing with diethyl ether (20 mL × 3), CH₂Cl₂ (5 mL), and acetone (5 mL), the product was obtained as a white powder (1.78 g, 3.21 mmol, yield = 92%). ¹H NMR (300 MHz, D₂O, 298 K): δ 9.35 (s, 1H), 9.06 (d, *J* = 6.1 Hz, 1H), 8.93 (d, *J* = 8.2 Hz, 1H), 8.23 (dd, *J* = 8.0, 6.3 Hz, 2H), 4.79 (t, 2H), 2.21 (m, 2H). ¹³C NMR (75 MHz, D₂O, 298 K): δ 165.73, 146.49, 144.43, 144.18, 134.09, 128.56, 61.28, 27.18. FT-IR (ATR, cm⁻¹): 3285, 3223, 3136, 3049, 2994, 1667, 1629, 1606, 1496, 1472, 1386, 1297, 1242, 1192, 1133, 1102, 1010, 915, 888, 822, 765, 669. Anal. Calcd for C₁₆H₂₀I₂N₄O₂: C, 34.68; H, 3.64; N, 10.11. Found: C, 34.53; H, 3.51; N, 9.92 (Figure 2.4).

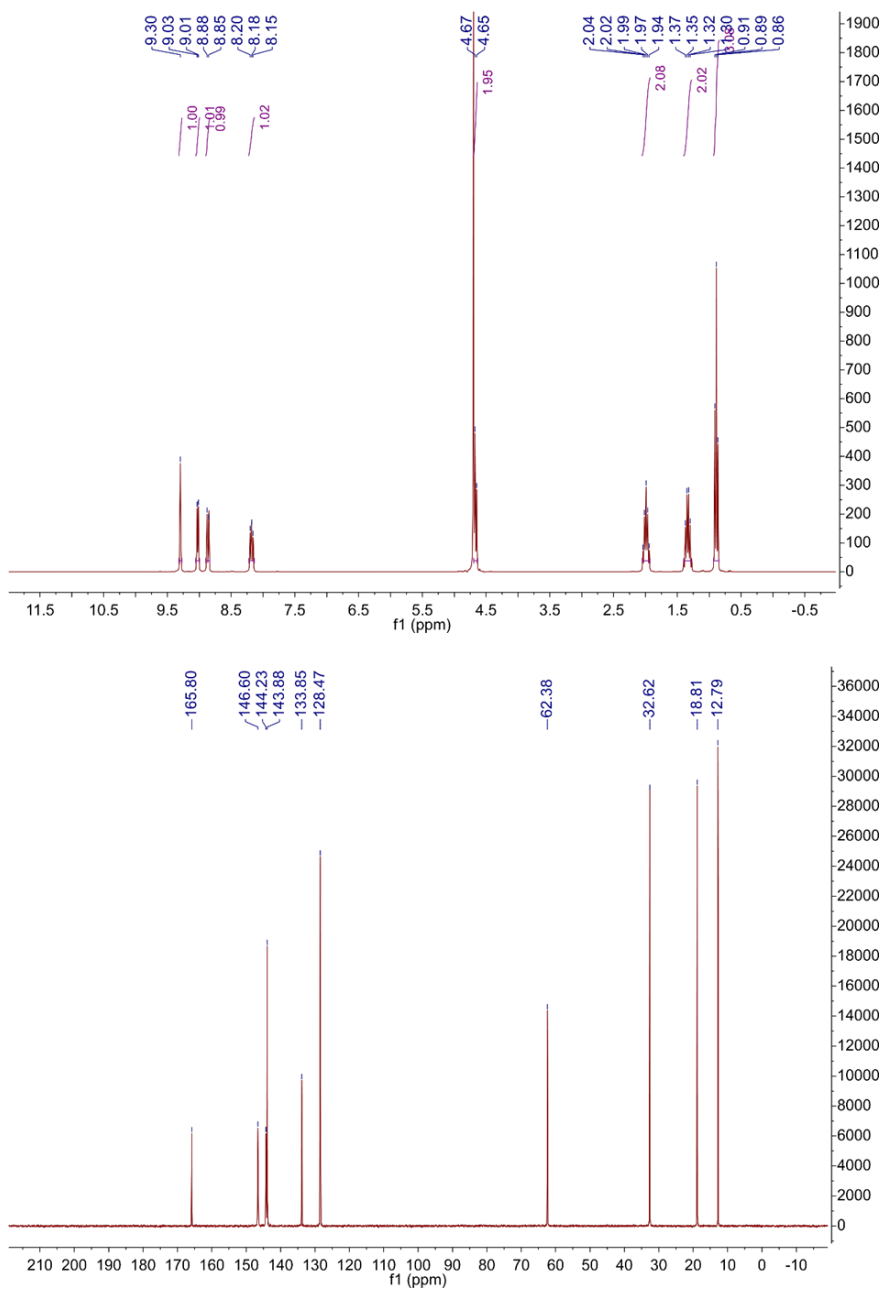


Figure 2.2. ¹H NMR (300 MHz, top) and ¹³C NMR (75 MHz, bottom) spectrum of mNAD-Cl in D₂O (*T* = 298 K).

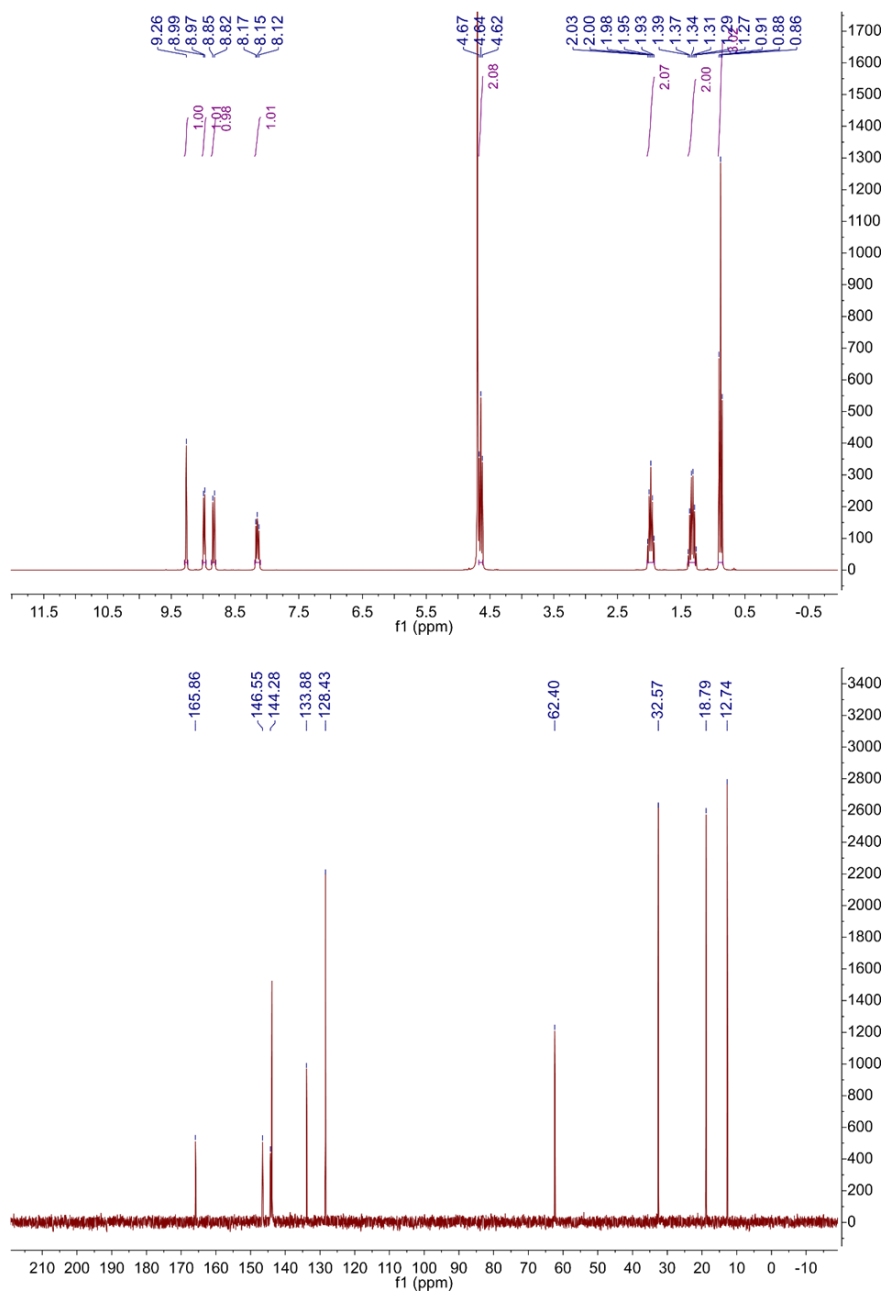


Figure 2.3. ¹H NMR (300 MHz, top) and ¹³C NMR (75 MHz, bottom) spectrum of mNAD-I in D₂O (*T* = 298 K).

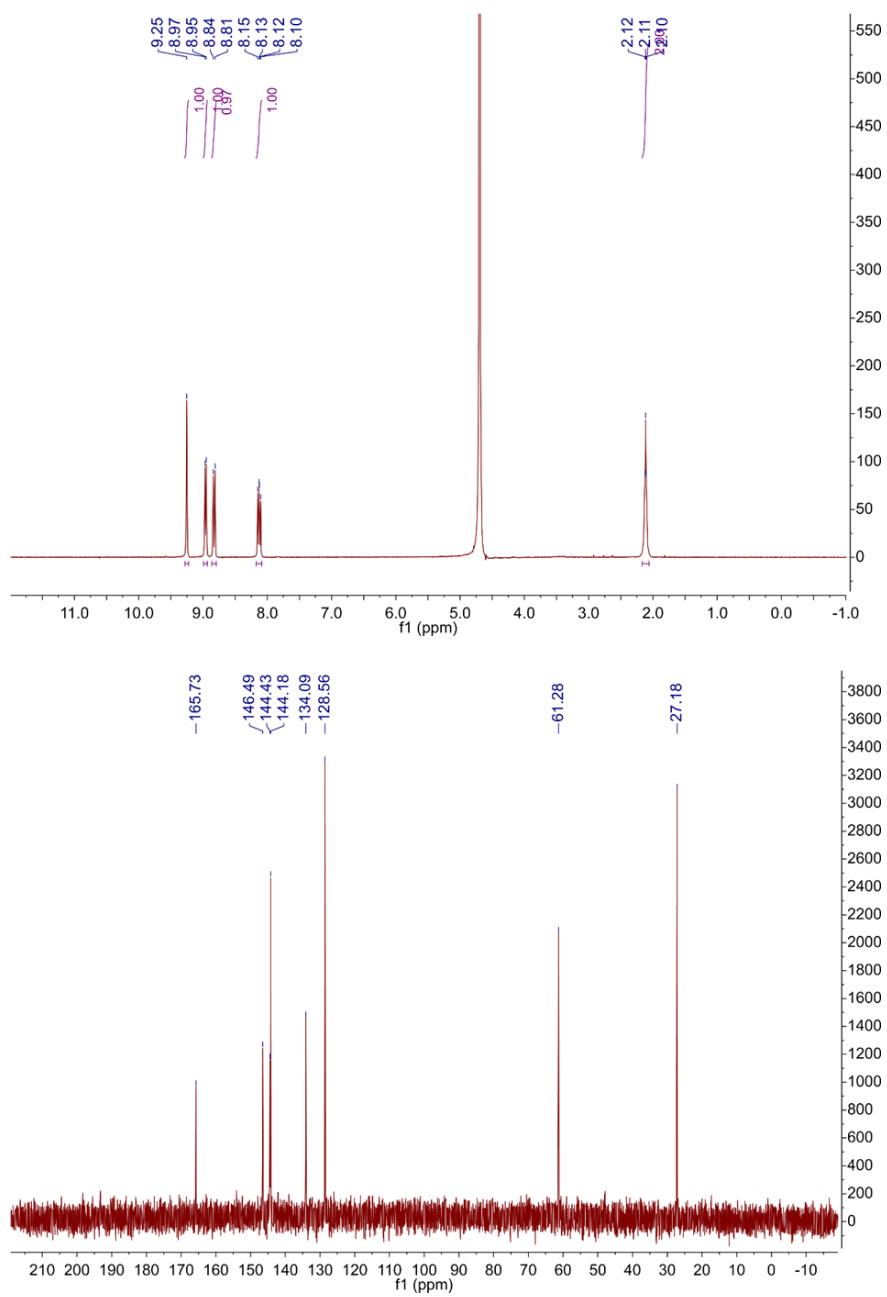


Figure 2.4. 1H NMR (300 MHz, top) and ^{13}C NMR (75 MHz, bottom) spectrum of $[(mNAD)_2Bu]I_2$ in D_2O ($T = 298\text{ K}$).

2.2.2 Electrochemical measurements

2032 type coin-cells with porous polypropylene membrane (Celgard) were used to measure electrochemical performances of mNAD-X molecules. mNAD-X electrodes were prepared by mixing 40% w/w active materials, 40% w/w conductive carbon (Super P) and 20% w/w PTFE (polytetrafluoroethylene, Sigma-Aldrich) binder. The electrolyte was 1 M LiTFSI in a mixture of ethylene carbonate (EC) and dimethyl carbonate (DMC) in a volume ratio of 1:1. The cells were assembled in Ar-filled glove box with relative humidity under 5 ppm. Galvanostatic tests were performed at a current density of 50 mA g⁻¹ in voltage range of 1.9 ~ 2.8 V on battery cycler (WMPG 1000). For GITT measurements, the Li/mNAD-I half cells were discharged and charged for 6 minute at 50 mA g⁻¹, with 2 hours rest time, in galvanostatic mode.

2.2.3 Computational details

We conducted ab initio calculation based on density functional theory (DFT) using GAMESS program.¹² Wave functions were approximated with 6-311G**(d,p) basis set, and the exchange-correlation functional was described by Becke-Lee-Yang-Parr (B3LYP) hybrid functional.^{13,14} Polarizable continuum model (PCM) method was implemented to implicitly consider the solvation effect.¹⁵ Atomic partial charge was calculated via Hirshfeld method. Molecular structure and orbitals were visualized with MacMolPlt program.¹⁶

2.2.4 Ex situ characterization

The mNAD-I electrodes at different states of charge (as-prepared, 20 mA g⁻¹ discharged, 40 mA g⁻¹ discharged, 60 mA g⁻¹ discharged, fully discharged to 1.9 V, 20 mA g⁻¹ charged, 40 mA g⁻¹ charged and fully charged to 2.8 V) were disassembled from coin cells for ex situ analyses. Fourier transform infrared spectroscopy (FTIR) measurements were performed on each electrode by using FTIR-4200 (Jasco Inc., Japan) at a resolution of 4 cm⁻¹ in vacuum. Samples were prepared as pellets made of electrodes and KBr powder. X-ray photoelectron spectroscopy (XPS) were operated by using Thermo VG Scientific Sigma Probe spectrometer (U.K.) equipped with a microfocus monochromated X-ray source (90 W). Binding energies of collected data were referenced to C 1s (284.5 eV). Photochemical stability of mNAD-I were confirmed by UV/Vis absorbance spectroscopy using V/650 spectrophotometer (Jasco Inc., Japan) and FTIR. mNAD-I powder, as-prepared electrodes, and as-prepared electrode in EC/DMC for 24 h were compared.

2.3 Results and discussions

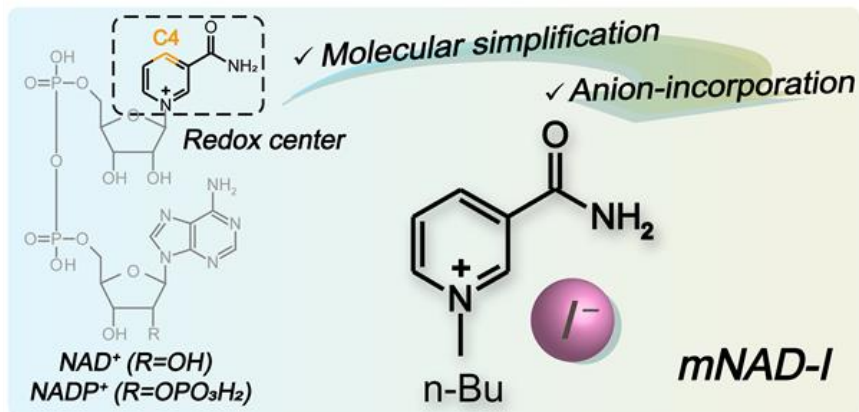
2.3.1 Molecular redesign of nicotinamide cofactor

In a typical biological energy transduction process, the redox reaction of NAD^+ involves two electrons and one proton, which can be expressed as a hydride (H^-) equivalent. The hydride equivalent from substrate transfers to NAD(P)^+ , resulting in the oxidized product and the reduced NAD(P)H .¹⁷ It is known that the active redox center lies particularly around C4 position in the molecular structure of NAD^+ , accompanying the reversible proton accommodation as illustrated in Figure 2.5a.¹⁸ In exploiting the NAD^+ redox activity in the battery system, we attempted to minimize the weight of bulky NAD^+ molecule while maintaining the redox-active center so that the specific capacity can be maximized with the given redox activity. In this respect, the adenosine diphosphate (ADP) ribose part in NAD^+ , which is redox-inactive, was substituted to a light butyl chain, leading to a new derivative, mNAD^+ . In the following step, positively charged mNAD^+ in a solution was precipitated by introducing counter anions such as iodide (I^-), which resulted in solid-state powder that can be fabricated into conventional electrodes.

The synthesized mNAD-I could manifest a reversible redox activity in the LIB system, exhibiting a reversible galvanostatic profile with a flat discharge potential at 2.1 V in Figure 2.5b. Considering that the NAD^+ in aqueous environment is known to exhibit 2.04 V (vs. Li^+/Li) for electron uptake,^{19,20} it indicates that the intrinsic redox activity of NAD^+ is preserved in mNAD-I even

after anion fixation. The electrochemical activity of Γ/I_3^- is about 3.2 V,²¹ supporting the notion that the redox activity at 2.3 V is attributable to the NAD⁺ motif. It was observed that mNAD-I could deliver the specific capacity of 77.7 mAh g⁻¹ in the lithium cell. It suggests that a nearly full one-electron transfer reaction could be feasible for the mNAD-I electrode in the lithium electrochemical cell.

a) Molecular design: mNAD-I



b)

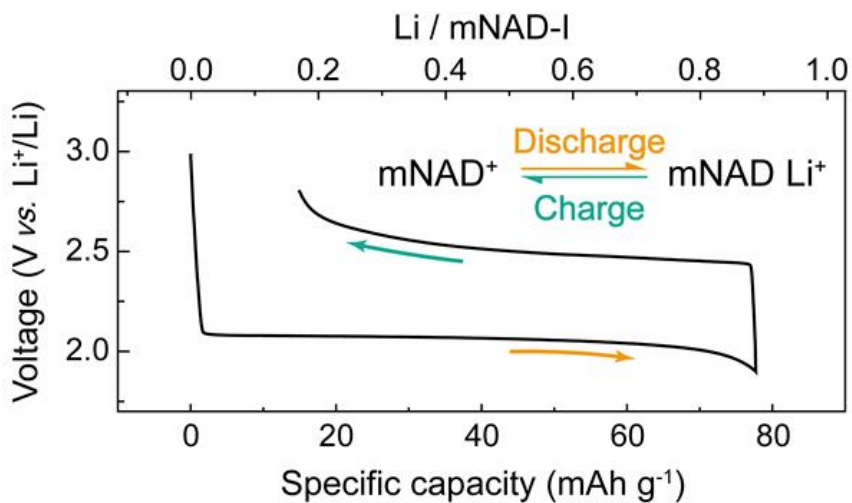


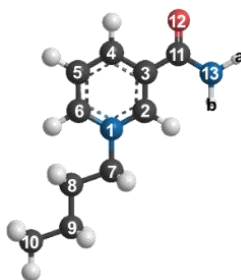
Figure 2.5. a) Molecular design strategy to mimic the redox center of NAD^+ to utilize it as the active material of the battery electrode. b) Galvanostatic discharge/charge profile of mNAD-I/Li cell indicating reversible lithium-coupled electron transfer reactions.

2.3.2 Reaction mechanism of mNAD⁺ in LIBs

The redox mechanism of mNAD-I was first investigated by conducting DFT calculations on the series of intermediate states. The energy calculations involving lithium incorporation to mNAD⁺ suggested that the equilibrium redox potential is about 2.0 V, which agrees with the galvanostatic data in Figure 2.5b. To verify the lithium binding site to mNAD⁺, various possible lithium sites were examined (Figure 2.6a). The most stable structure was the one in which lithium binds with C4 (Li–C4 bond in Figure 2.6b), which is consistent with the proton-bearing site for the NAD⁺ redox reaction in the biological energy transduction process, implying the analogy between lithium and proton incorporations in NAD⁺.¹⁸ In addition to the C4 atom, the lithium ion was found to strongly interact with oxygen in the amide group, forming a five-membered –C4–C3–C11–O12–Li– ring.⁵ The Hirshfeld charge of pristine (mNAD⁺) and discharged (mNAD Li⁺) states in Figure 2.7a and the Figure 2.8 indicates that the change in charge density around C4 atom upon lithium insertion is the most significant, supporting the major binding of the lithium to C4. Furthermore, in Figure 2.7b and the Table 2.1, the bond lengths of C2–C3, C5–C6, and C3–C11 were shortened upon lithiation, while others in the pyridinium ring, N1–C2, C3–C4, C4–C5, C6–N1, and O12–C11, were lengthened. This trend is similar to changes seen when NAD⁺ was reduced to NADH in biological systems, and reflects the fact that the inserted electron is dispersed in conjugation area from pyridinium to amide group resulting in the stable lithiated structure.²²

Inspired by the redox activity of mNAD⁺ in a lithium-coupled electrochemical reaction proposed by the theoretical calculations, post mortem analysis was carried out for mNAD-I electrodes at different states of charge and discharge in the lithium cell by FTIR (Fourier transform infrared spectroscopy) analysis (Figure 2.7c). While the precise assignment of all the peaks was not trivial, the most notable change in the FTIR spectrum could be found in the C=O bond in amide group (Figure 2.7c right). The absorbance signal at 1686 cm⁻¹ attributed to the stretching of C=O bond in amide group disappeared gradually with discharge and was reversibly recovered with charge.²³ Additionally, spectral data in fingerprint region of 1000–1500 cm⁻¹ were reversibly changed during the discharge/charge process (Figure 2.9 and Table 2.2). FTIR spectra verify the active involvement of the C=O/C–O bonds in the lithium insertion,²⁴ which is consistent with the formation of the five-membered –C4–C3–C11–O12–Li– ring in the DFT calculations. To better understand the redox mechanism, XPS (X-ray photoelectron spectroscopy) analysis of O 1s spectra was additionally conducted at three representative states; as-prepared, fully discharged (ca. 1.9 V) and fully charged (ca. 2.8 V) states (Figure 2.7d). The oxygen peak centered at 532.6 eV corresponding to C=O²⁵ is noticeably broadened with discharge, and is reversibly recovered with charge. The peak broadening toward lower binding energy region for the discharged electrode indicates the formation of additional peak, which can be deconvoluted into a new peak at 531.7 eV and signifies the formation of the bond between lithium and oxygen.²⁶ The XPS peak at 531.7 eV from O–Li bond disappears with charge,

resulting in the restoration of the pristine state of mNAD-I, which is consistent with FTIR results.



Unit:

Å

	N1-C7	C7-C8	C8-C9	C9-C10	C2-H	C4-H	C5-H	C6-H
mNAD ⁺	1.50	1.53	1.53	1.53	1.08	1.08	1.08	1.08
mNAD Li ⁺	1.47	1.53	1.53	1.53	1.08	1.09	1.08	1.08

	C7-H	C8-H	C9-H	C10-H	N13-Ha	N13-Hb
mNAD ⁺	1.09	1.10	1.10	1.09	1.01	1.01
mNAD Li ⁺	1.09	1.10	1.10	1.09	1.01	1.01

Table 2.1. Calculated bond length of mNAD⁺ and mNAD Li⁺ for all bonds. The hydrogen atoms bonded to the same carbon have the same C-H bond length. There are no remarkable changes in butyl group and carbon-proton bonds during Li-coupled reduction process.

Wavenumber (cm ⁻¹)	Vibrational mode
3300~3500	Amide N-H stretching mode
2800~3100	Pyridinium C-H stretching mode Butyl tail C-H stretching mode
1686	Amide C=O stretching mode (Amide I)
1618	Pyridinium coupled amide C=O stretching mode Amide H-N-H scissoring mode (Amide II)
1375~1525	Butyl tail C-H bending mode Pyridinium ring asymmetric twist mode
1347	Pyridinium coupled amide C-N stretching mode (Amide III)
1000~1200	Pyridinium in plane vibration mode

Table 2.2. Peak assignments in FTIR spectrum using DFT calculations. The reversible changes of the vibrational modes including the stretching of C=O bond and others within fingerprint region indicate that experimental results are compatible with computational calculations.

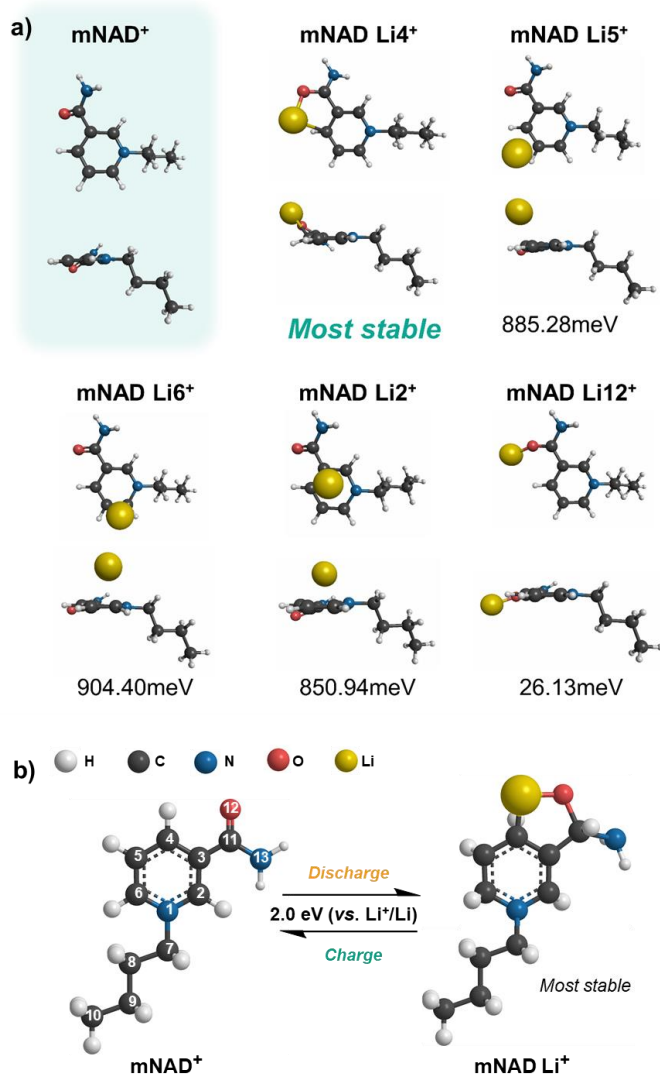


Figure 2.6. a) DFT energies calculated for mNAD⁺ and various mNAD Li⁺ with different lithium ion sites. The mNAD Li⁴⁺, in which lithium atom was inserted near C4 site, is energetically most stable compared to other structures. b) Molecular structure of mNAD⁺ and mNAD Li⁺ which is reduced with lithium insertion, predicted from DFT calculations.

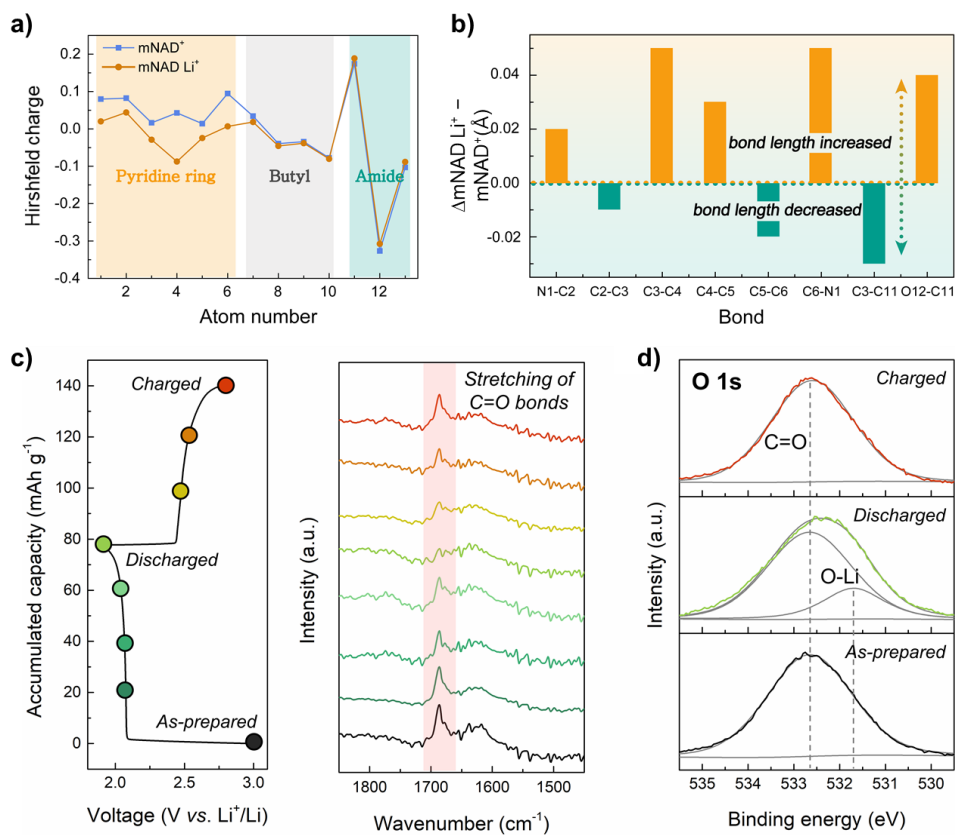
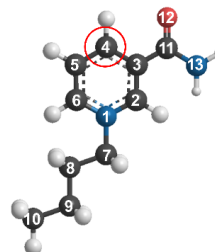
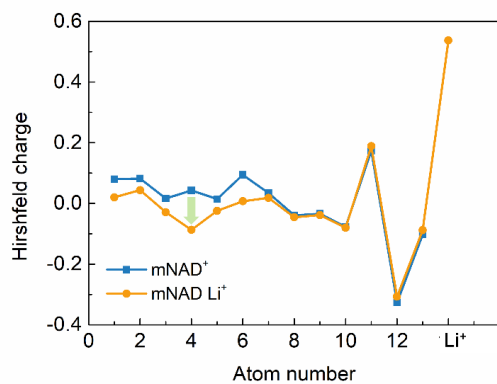


Figure 2.7. a) Hirshfeld charge analysis for each atom of mNAD⁺ and mNAD Li⁺. b) The major bond length changes of mNAD⁺ upon lithiation. c) Ex situ analysis of mNAD-I at various states of charge in mNAD-I/Li cell. FTIR spectra containing information of CO vibration. d) XPS spectra of O1s local scan: as-prepared state, discharged state to 1.9 V and recharged state to 2.8 V.



	1	2	3	4	5	6	7	8	9	10	11	12	13	Li ⁺
mNAD ⁺	0.0797	0.0823	0.0163	0.0427	0.0141	0.0946	0.0341	-0.0392	-0.0343	-0.0776	0.1742	-0.3266	-0.103	
mNAD Li ⁺	0.0200	0.0439	-0.0290	-0.0873	-0.0245	0.0068	0.0183	-0.0456	-0.0383	-0.0802	0.1887	-0.3074	-0.088	0.5369
mNADLi ⁺ - mNAD ⁺	-0.0597	-0.0384	-0.0453	-0.13	-0.0386	-0.0878	-0.0158	-0.0064	-0.004	-0.0026	0.0145	0.0192	0.015	

Figure 2.8. Calculated Hirshfeld charge of mNAD⁺ and mNADLi⁺. The Hirshfeld charge of C4 was remarkably reduced, indicating the increment of the electron density, which may be attributed to the binding with lithium cation.

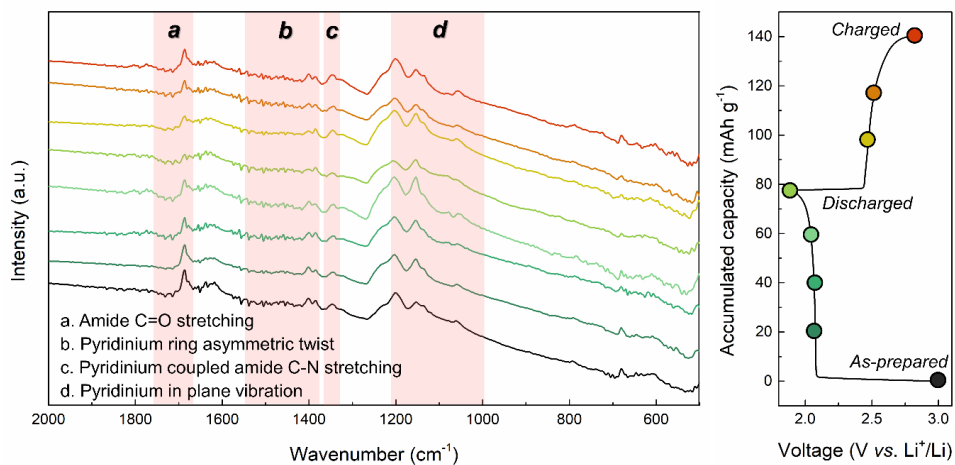


Figure 2.9. Full range spectra of ex situ FTIR from 500 cm⁻¹ to 2000 cm⁻¹ with peak assignments for each vibrational mode. The reversible changes during the discharge/charge indicate that lithiated structure was stabilized by conjugation from pyridinium to amide group.

2.3.3 The effect of anions on electrochemical performance in mNAD-X

We attempted to further explore the mNAD⁺ redox chemistry by investigating the effect of anion species in mNAD-I electrodes by replacing I⁻ with other halide ions (X⁻). Following the similar chemical route to produce mNAD-I, mNAD-Br, and mNAD-Cl were successfully synthesized in a solid-state powder. Figure 2.10a depicts the electrochemical profiles of the mNAD-I, mNAD-Br, and mNAD-Cl electrodes in a lithium cell. It is clear that all the mNAD-X electrodes exhibit reversible electrochemical activity. Moreover, all of the electrodes displayed a flat charge/discharge profile at a similar redox potential, which confirms the general redox activity of mNAD⁺ in mNAD-X electrodes. However, a close inspection of each electrochemical profile revealed that the capacity and the redox potential were slightly altered depending on the type of anion. It was observed that mNAD-X electrodes with larger anion species are capable of storing a larger amount of lithium per mNAD⁺. It was also observed that specific capacity was increased with heavier anion while theoretical capacity was expected to decrease in general (Figure 2.11). The systematic increase in the lithium incorporation for mNAD-X electrodes with the order of X=I>Br>Cl implies the better accessibility of the lithium ions offered by different anions. We speculated that those tendency may be related to the crystal lattice of mNAD-X and migration channels available for lithium ions (Figure 2.12). It is generally accepted that, for a given crystal structure, larger constituting atoms can offer greater ratio of free

space in the lattice, which may facilitate the interstitial diffusion.²⁷ Therefore, we believe that mNAD-I with larger Γ^- anion could provide the highest lithium ion accessibility with sufficient free space, resulting in the most lithium incorporation per mNAD⁺.

Another notable difference among mNAD-X is that the redox potential increases with the smaller counter anion in the order of Cl⁻>Br⁻>I⁻. Figure 2.10b presents the dQ/dV curves for each electrode, which reveals that the reduction potential gradually increased with smaller anion species. We conducted GITT (galvanostatic intermittent titration technique) measurements to compare the thermodynamic reduction potentials excluding kinetic factors (Figure 2.13). It consistently shows that mNAD-I manifested the lowest discharge potential. This anion dependence of the voltage can be explained by the hard–soft acid–base theory (HSAB theory). The lithium ion, which is a non-polarizable hard acid, is likely to exhibit stronger interaction with hard base. Consequently, the stronger interaction between lithium ion and chloride ion would lead to the highest stabilization energy for lithium insertion in mNAD-Cl, and thus the highest voltage. It suggests that without modifying the redox-active part, the systematic voltage tuning is possible by simple replacement of counterions.

To optimize the electrochemical performance we further synthesized a dimer by linking two redox centers (Figure 2.14a,b). Butyl-linked mNAD-I showed reversible electrochemical activity with the average voltage of 2.3 V, equal to that

of mNAD-I electrode, indicating that the redox activity of mNAD⁺ was well-preserved. According to our observation, butyl-linked mNAD-I exhibited increased cycle stability over monomeric mNAD-I electrode (Figure 2.14c). We attribute this result to the mitigated dissolution of the redox-active organic chemicals into electrolyte. The cycle stability of mNAD-X electrode is yet low compared with conventional cathode materials, and also capacity deterioration after butyl-linking remains a challenge in terms of energy density. Nevertheless, we believe that the molecular tunability of organic molecules, including polymerization²⁸ or substitution of functional group,⁵ would allow diverse strategies for enhancing electrochemical performances of the mNAD-X electrode. Engineering electrode architectures via the synthesis of carbo-organic composite²⁹ also should be taken into consideration in future modeling of mNAD-X electrodes.

a) Series of mNAD X

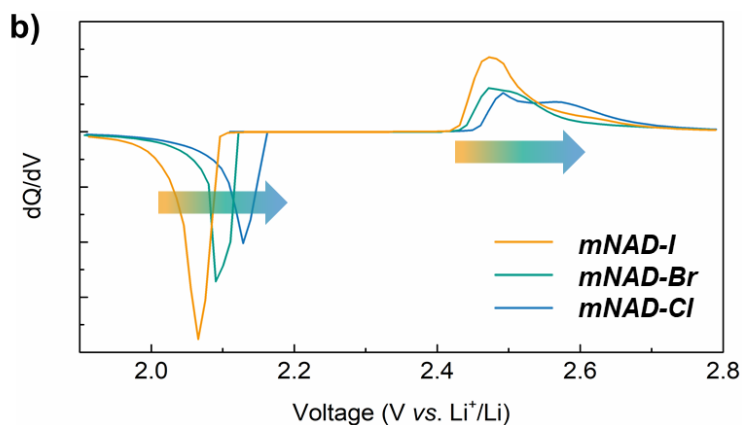
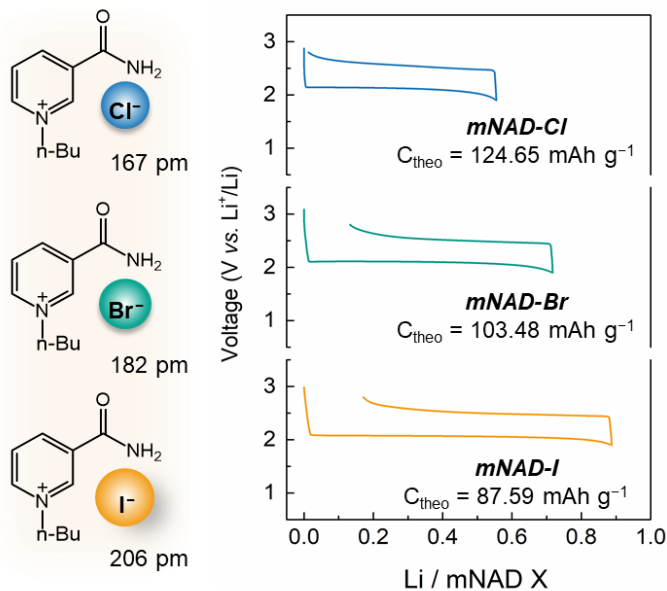


Figure 2.10. a) Electrochemical profile of mNAD-X with various halides. As the size of the anion increases, the amount of lithium per each molecule that inserts and deinserts reversibly increases. b) Differential capacity (dQ/dV) curves of mNAD-X/Li cells calculated from the data shown in Figure 2b. As the size of the anion decreases, the discharge potential increases.

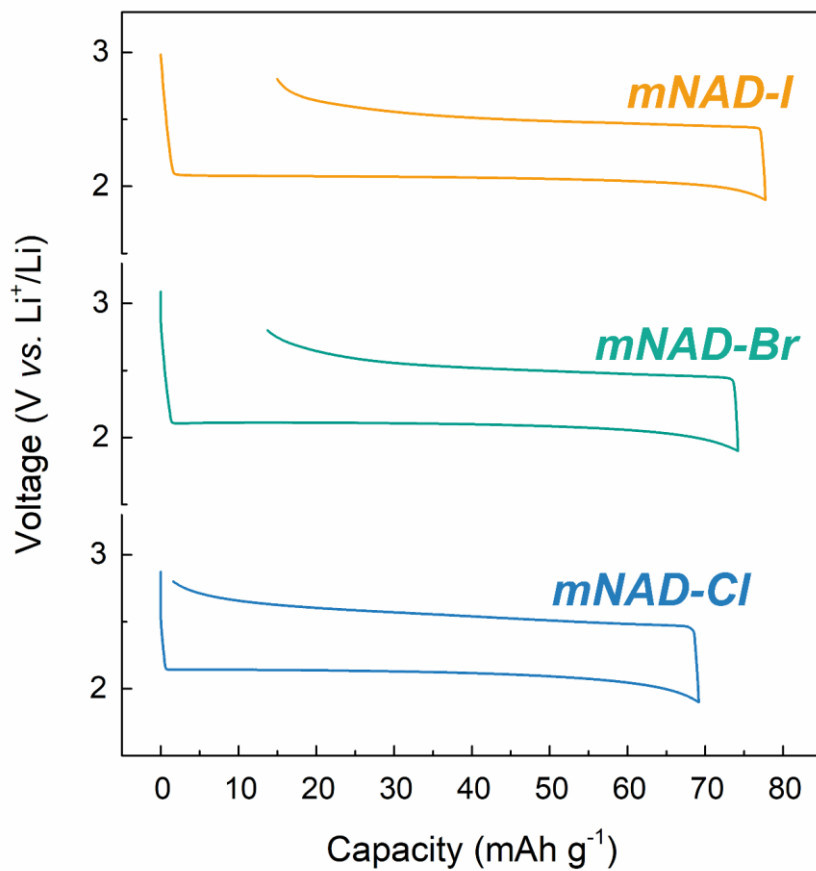


Figure 2.11. Electrochemical profile of mNAD-X with various halides. The theoretical specific capacity of mNAD-Cl, mNAD-Br and mNAD-I are 124.65, 103.48 and 87.59 mAh g⁻¹, respectively.

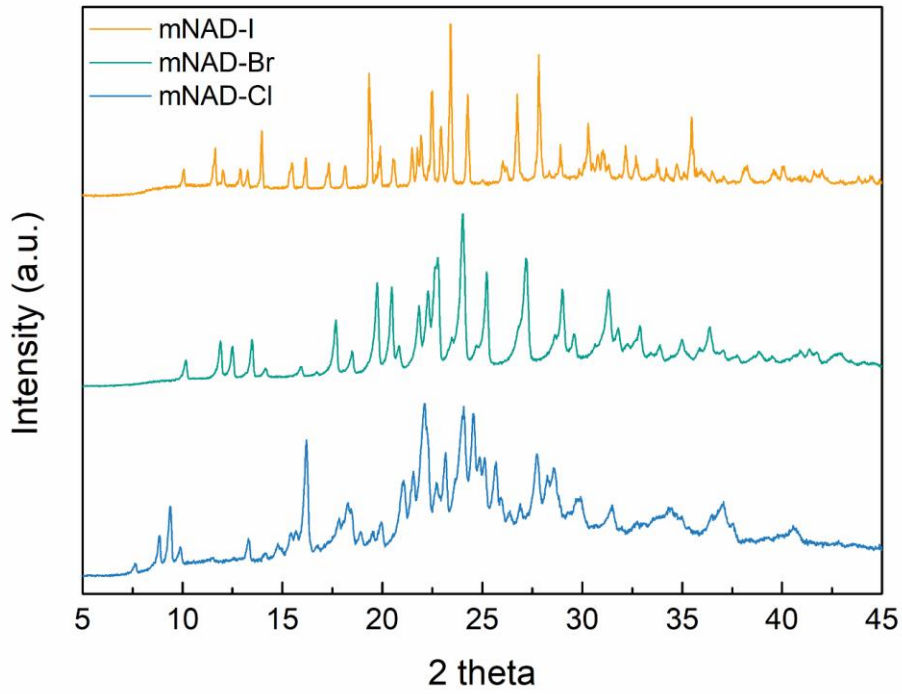


Figure 2.12. XRD patterns of powder mNAD-Cl, mNAD-Br and mNAD-I.

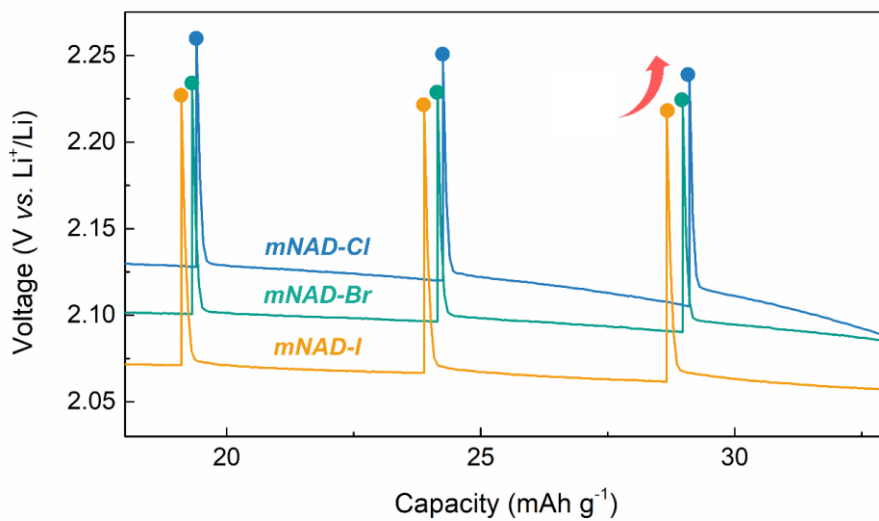


Figure 2.13. GITT curves of each NAD⁺-derivative (mNAD-Cl, mNAD-Br, and mNAD-I) from second to fourth steps. The smaller the size of the anion, the higher the thermodynamic reduction potential.

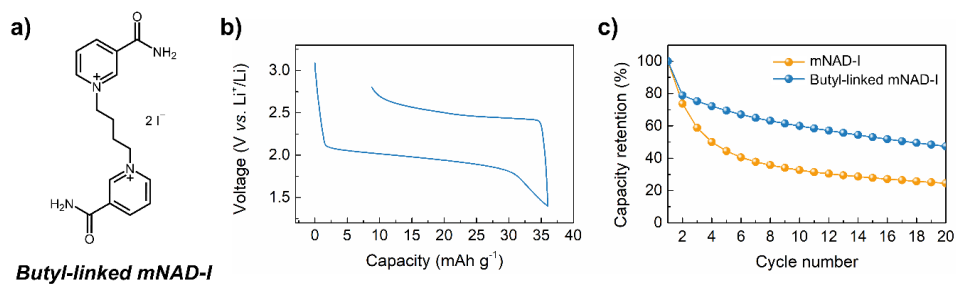


Figure 2.14. a) Molecular structure of Butyl-linked mNAD-I. b) Electrochemical profile of butyl-linked mNAD-I. It also showed reversible reaction with average voltage of 2.3 V. c) Enhanced cycle performance of butyl-linked mNAD-I compared to mNAD-I.

2.4 Concluding remarks

In summary, we exploited the NAD^+ motif, one of the most versatile redox centers in nature, to facilitate reversible electrochemical energy storage in LIB system for the first time. Through the simple substitution and the anion-fixation strategy, the natural NAD^+ motif in the solution could be converted into new mNAD-X electrodes, which were capable of reversibly storing lithium ions. Combined experimental and theoretical calculations revealed that mNAD-X retains the intrinsic redox activity of natural NAD^+ motif, accompanying lithium-coupled electron transfer which is similar to the proton-coupled electron transfer mechanism in the biological systems. The series of mNAD-X synthesized successfully here confirm that the anchoring of the charged biological cofactors with anion incorporation is a viable new approach to exploit various charged biological cofactors in rechargeable battery system. Moreover, it was demonstrated that the electrochemical properties of the cofactor could be tuned by anion characteristics by changing molecular arrangements and electronegativity within electrode. This study suggests a new approach of utilizing myriad of unexplored bio-derived materials, in the development of artificial energy storage systems.

2.5 References

- 1 Armand, M. & Tarascon, J. M. Building better batteries. *Nature* **451**, 652, (2008).
- 2 Wu, X. *et al.* Unraveling the storage mechanism in organic carbonyl electrodes for sodium-ion batteries. *Sci. Adv.* **1**, e1500330.
- 3 Lee, B. *et al.* Exploiting Biological Systems: Toward Eco-Friendly and High-Efficiency Rechargeable Batteries. *Joule* **2**, 61-75, (2018).
- 4 Yang, P. & Tarascon, J.-M. Towards systems materials engineering. *Nat. Mater.* **11**, 560-563, (2012).
- 5 Lee, M. *et al.* Redox Cofactor from Biological Energy Transduction as Molecularly Tunable Energy-Storage Compound. *Angew. Chem. Int. Ed.* **52**, 8322-8328, (2013).
- 6 Orita, A., Verde, M. G., Sakai, M. & Meng, Y. S. A biomimetic redox flow battery based on flavin mononucleotide. *Nat. Commun.* **7**, 13230, (2016).
- 7 Wang, X. *et al.* Cofactor NAD(P)H Regeneration Inspired by Heterogeneous Pathways. *Chem* **2**, 621-654, (2017).
- 8 Verdin, E. NAD⁺ in aging, metabolism, and neurodegeneration. *Science* **350**, 1208-1213, (2015).
- 9 Paul, C. E. *et al.* Mimicking Nature: Synthetic Nicotinamide Cofactors for C=C Bioreduction Using Enoate Reductases. *Org. Lett.* **15**, 180-183, (2013).
- 10 Anderson, B. M., Reynolds, M. L. & Anderson, C. D. Hydrophobic

- interactions of inhibitors with yeast alcohol dehydrogenase. *Biochimica et Biophysica Acta* **99**, 46-55, (1965).
- 11 Tomizaki, K.-y., Tsunekawa, Y., Akisada, H., Mihara, H. & Nishino, N. Design and characterization of flavoenzyme models in the course of chemical evolution of four- α -helix bundle polypeptides. *J. Chem. Soc., Perkin trans. II*, 813-822, (2000).
- 12 Schmidt, M. W. *et al.* General atomic and molecular electronic structure system. *J. Comput. Chem.* **14**, 1347-1363, (1993).
- 13 Becke, A. D. Density-functional exchange-energy approximation with correct asymptotic behavior. *Phys. Rev. A* **38**, 3098-3100, (1988).
- 14 Lee, C., Yang, W. & Parr, R. G. Development of the Colle-Salvetti correlation-energy formula into a functional of the electron density. *Phys. Rev. B* **37**, 785-789, (1988).
- 15 Li, H., Pomelli, C. S. & Jensen, J. H. Continuum solvation of large molecules described by QM/MM: a semi-iterative implementation of the PCM/EFP interface. *Theor. Chem. Acc.* **109**, 71-84, (2003).
- 16 Bode, B. M. & Gordon, M. S. Macmolplt: a graphical user interface for GAMESS. *J. Mol. Graph. Model.* **16**, 133-138, (1998).
- 17 Knaus, T. *et al.* Better than Nature: Nicotinamide Biomimetics That Outperform Natural Coenzymes. *J. Am. Chem. Soc.* **138**, 1033-1039, (2016).
- 18 Gorton, L. & Domínguez, E. *Encyclopedia of Electrochemistry*. Vol. 9

- (Wiley-VCH, 2007).
- 19 Lee, Y. W. *et al.* Unbiased biocatalytic solar-to-chemical conversion by FeOOH/BiVO₄/perovskite tandem structure. *Nat. Commun.* **9**, 4208, (2018).
- 20 Damian, A., Maloo, K. & Omanovic, S. Direct electrochemical regeneration of NADH on Au, Cu and Pt-Au electrodes. *Chem. Biochem. Eng. Q* **21**, 21-32, (2007).
- 21 Kwak, W.-J. *et al.* Li–O₂ cells with LiBr as an electrolyte and a redox mediator. *Energy Environ. Sci.* **9**, 2334-2345, (2016).
- 22 Schulz, F., Leca, F., Hollmann, F. & Reetz, M. T. Towards practical biocatalytic Baeyer-Villiger reactions: applying a thermostable enzyme in the gram-scale synthesis of optically-active lactones in a two-liquid-phase system. *Beilstein J. Org. Chem.* **1**, 10, (2005).
- 23 Ramalingam, S., Periandy, S., Govindarajan, M. & Mohan, S. FT-IR and FT-Raman vibrational spectra and molecular structure investigation of nicotinamide: A combined experimental and theoretical study. *Spectrochim. Acta, Part A* **75**, 1552-1558, (2010).
- 24 Atac, A., Karabacak, M., Kose, E. & Karaca, C. Spectroscopic (NMR, UV, FT-IR and FT-Raman) analysis and theoretical investigation of nicotinamide N-oxide with density functional theory. *Spectrochim. Acta, Part A* **83**, 250-258, (2011).
- 25 Goel, C., Bhunia, H. & Bajpai, P. K. Synthesis of nitrogen doped

- mesoporous carbons for carbon dioxide capture. *RSC Adv.* **5**, 46568-46582, (2015).
- 26 Rendek, L. J., Chottiner, G. S. & Scherson, D. A. Reactivity of Linear Alkyl Carbonates toward Metallic Lithium: Infrared Reflection–Absorption Spectroscopic Studies in Ultrahigh Vacuum. *Langmuir* **18**, 6554-6558, (2002).
- 27 Zeier, W. G., Zhou, S., Lopez-Bermudez, B., Page, K. & Melot, B. C. Dependence of the Li-Ion Conductivity and Activation Energies on the Crystal Structure and Ionic Radii in $\text{Li}_6\text{MLa}_2\text{Ta}_2\text{O}_{12}$. *ACS Appl. Mater. Interfaces* **6**, 10900-10907, (2014).
- 28 Song, Z. *et al.* Polyanthraquinone as a Reliable Organic Electrode for Stable and Fast Lithium Storage. *Angew. Chem. Int. Ed.* **54**, 13947-13951, (2015).
- 29 Kim, J.-K., Kim, Y., Park, S., Ko, H. & Kim, Y. Encapsulation of organic active materials in carbon nanotubes for application to high-electrochemical-performance sodium batteries. *Energy Environ. Sci.* **9**, 1264-1269, (2016).

Chapter 3. Molecular fusion strategy to design bipolar organic materials for high-energy-density symmetric batteries

(The essence of this chapter has been published in *Journal of Materials Chemistry A*. Reproduced with permission from [Kim, J.[†], and Kim, H.[†] *et al.*, *J. Mater. Chem. A* **2021**, 9, 14485-14494] Copyright (2021) Royal Society of Chemistry)

3.1 Research background

In the past few decades, lithium-ion batteries (LIBs) have been successfully adopted in various applications ranging from portable electronic devices to electric vehicles (EVs), owing to their high energy and power densities.^{1,2} With the growing market for LIBs and the projected large production, there has been a heightened awareness of environmental issues and the need for sustainable and affordable LIB systems. Organic batteries which employ redox-active organic compounds as electrodes are one of the candidates for such rechargeable batteries with the least environmental footprints.^{3,4} The shift to organic-based battery chemistry would allow the relatively low energy-cost processes without the need for high temperature or pressure treatments, reducing the economic/environmental burden occurring in the synthesis of conventional electrode materials used in LIBs. Moreover, certain redox-active organic materials,

including quinone/flavin derivatives and $\text{Li}_x\text{C}_6\text{O}_6$, can be produced or even directly derived from biomass, which further promises a step forward to sustainable batteries, while the current electrode chemistry in LIBs requires the resources that are often found in limited regions, *e.g.* the transition metal.⁵⁻⁸

It is generally known that the organic redox compounds undergo the redox process *via* either the *n*-type or *p*-type reaction accompanying the change in the chemical bonding.^{3,9,10} Upon the electrochemical reaction, *n*-type organic compounds are capable of being reduced by accepting electrons in the structure, while *p*-type ones can be oxidized through the removal of electrons from the neutral state.^{11,12} One of the interesting features of organic electrodes is that some redox compounds can exhibit both *n*-type and *p*-type redox activities within one molecular structure, *i.e.* displaying a bipolar nature. It implies that it may serve both as negative and positive electrodes depending on the given electrochemical condition and can be effectively utilized in the construction of the symmetric batteries. Symmetric batteries are the systems that employ an identical material for both electrodes and simultaneously store cations and anions into the anode and the cathode during the charging process. Because of their unique working mechanism, the system requires more electrolytes than conventional cells, which often leads to a low energy density. Nonetheless, in terms of the low-cost unified process and chemical sustainability that does not require the component compatibility, the DIB is regarded one of the promising alternatives of the current rechargeable battery. Research studies to overcome the challenges of DIBs have been actively conducted

in recent years.¹³⁻¹⁵ Furthermore, the electrode fabrication procedure can also be greatly simplified because separate manufacturing processes and their assemblies are no longer needed,¹⁶ and it correspondingly leads to a substantial reduction in the production cost.¹⁷⁻¹⁹ Additionally, using the same material for both the cathode and anode would circumvent the complex issues regarding the chemical/electrochemical compatibilities among the battery components, which would eventually accompany less chances of side reactions in battery operations.

There have been a few attempts to realize the symmetric batteries employing organic-based redox materials as electrodes.²⁰⁻²⁵ Chen *et al.* utilized the redox active lithium-tetrahydroxybenzoquinone salt, which possess multiple *n*-type redox motifs that have been partially reduced.²⁰ The partially reduced *n*-type carbonyl motifs in the molecule could serve as the redox active sites for both the discharge and charge, thus exhibiting the bipolar nature. The symmetric cell employing the two tetrahydroxybenzoquinone-based electrodes could successfully deliver a capacity of 178 mA h g⁻¹, even though the average voltage was relatively low (~ 0.8 V). Wang *et al.* also showed that Na₄DHTPA (Na₄C₈H₂O₆, tetrasodium salt of 2,5-dihydroxyterephthalic acid), which hold two different *n*-type redox motifs, *i.e.* carbonyl groups and carboxylate groups, could exhibit the bipolar properties in a symmetric cell.²¹ Similar to the case of tetrahydroxybenzoquinone, a part of the *n*-type motif (carbonyl group) was prepared in a reduced state in the pristine molecule, and thus could be readily charged, while carboxylate groups could function as the redox site for the discharge. The symmetric cell was capable

of delivering a capacity of 198 mA h g⁻¹ at an average voltage of 1.8 V. However, these previous studies demonstrated the potential applicability of the multi-redox organic electrodes for symmetric batteries; the low voltages were the clear practical limitations, which were attributable to generally similar potentials available from the *n*-type redox-active centers in one molecule. Recently, Dai *et al.* demonstrated that the combination of the *n*-type and *p*-type redox-active centers could offer a higher-voltage symmetric cell, benefiting from the intrinsically high *p*-type redox potential in a dual-ion system.²⁵ The use of the different redox centers could deliver a higher cell voltage; nevertheless, the use of a linker in combining the two redox couples inevitably resulted in an increase in the molecular weight, thus decreasing the overall energy density.

3.2 Experimental method

3.2.1 Preparation of materials

PNZ and TA were purchased from Sigma-Aldrich (UK) and TCI Chemicals (Japan), respectively. 1,2-Benzenedithiol and 2,3-dichloroquinoxaline were purchased from TCI Chemicals (Japan). Sodium perchlorate (NaClO₄, anhydrous), bis(trifluoromethane)sulfonimide lithium salt (LiTFSI, anhydrous), diethylene glycol dimethyl ether (DEGDME, anhydrous), and acetonitrile (MeCN, anhydrous) were purchased from Sigma-Aldrich (UK). 1,2-Benzenedithiol and 2,3-dichloroquinoxaline were purchased from TCI Chemicals (Japan). The salt was dried overnight in a vacuum. All the electrolytes were prepared and used in an Ar-filled glovebox (O₂ < 0.5 ppm, H₂O < 0.5 ppm). ¹H NMR and ¹³C NMR spectra were recorded on a 500 MHz Varian/Oxford As-500 spectrometer. The X-ray structure of PNZTA was obtained on a Rigaku XtaLAB PRO single-crystal diffractometer.

3.2.2 Synthesis and characterization of PNZTA

PNZTA was prepared by adapting the reported procedure.²⁶ A 250 mL round bottom flask (RBF) was charged with 1,2-benzenedithiol (1.173 g, 8.247 mmol), 2,3-dichloroquinoxaline (1.340 g, 6.732 mmol), K₂CO₃ (5.750 g, 41.61 mmol), and dimethylformamide (DMF, 55 mL). The mixture was stirred at r.t. for 24 h. H₂O (50 mL) was added to quench the reaction. The aqueous phase was

extracted three times with dichloromethane (DCM, 150 mL \times 3). The combined organic phase was dried over anhydrous MgSO₄, filtered, and concentrated under reduced pressure. Flash column chromatography on SiO₂ (hexane : DCM = 8 : 2 to 0 : 10, v/v) furnished PNZTA as a yellow solid (1.764 g, 6.574 mmol, yield = 98%). The spectroscopic data provided in the ESI (Figure 3.1) match well with the reported values. ¹H NMR (500 MHz, CDCl₃, 298 K): δ 7.97–7.93 (m, 2H), 7.70–7.66 (m, 2H), 7.50–7.47 (m, 2H), and 7.31–7.28 (m, 2H). ¹³C NMR (125 MHz, CDCl₃, 298 K): δ 152.35, 140.71, 131.56, 130.13, 128.84, 128.38, and 128.37.

3.2.3 X-ray crystallographic studies on PNZTA

Single crystals of PNZTA were obtained by slowly cooling hot ethyl acetate (EtOAc) solution of this material. A fluorescent yellow crystal (approximate dimensions of 0.452 \times 0.334 \times 0.13 mm³) was placed onto a nylon loop with Paratone-N oil and mounted on a Rigaku XtaLAB PRO single-crystal diffractometer. The data collection was performed using Cu K α radiation, and the crystal was kept at 93 K. A total of 6515 reflections were measured ($10.166^\circ \leq 2\theta \leq 158.978^\circ$). The structure was determined using the SHELXT²⁷ structure solution program with intrinsic phasing and refined with the SHELXL²⁸ refinement package of OLEX2.²⁹ A total of 2415 unique reflections were used in all the calculations. The final R_1 was 0.0408 ($I \geq 2\sigma(I)$) and wR_2 was 0.1216 (all data). CCDC 2030804 contains the supplementary crystallographic data for this structure.

3.2.4 Electrochemical measurements

For the three-electrode system, a glassy carbon electrode, Pt counter electrode, and Ag/AgNO₃ reference electrode were employed, and the CV curves of PNZ, TA, and PNZTA were obtained at a scan rate of 100 mV s⁻¹. Voltage–capacity profiles of the PNZ, TA, and PNZTA molecules *versus* Na⁺/Na in coin-type cells (CR2032) were obtained using the following procedure. The electrodes were fabricated by mixing 40 wt% active materials, 40 wt% conducting carbon (Super P), and 20 wt% PTFE (polytetrafluoroethylene, Aldrich) binder, and all of the sample electrodes were 4–7 mg. The sodium metal electrode was prepared by rolling a sodium cube (Na, contains mineral oil, 99.9%) into a sheet after removing the contaminated surface. The electrolyte was 3.5 m NaClO₄ in DEGDME. A Nafion-coated microporous polypropylene membrane (Celgard 2400, Wellcos, Korea) and glass microfiber membrane (GF/F, Whatman, UK) were simultaneously used as the separator (Figure 3.2). To fabricate the Nafion coating on the Celgard, Nafion-containing solution was dropped on the washed Celgard membrane, which was then dried and immersed in the electrolyte for 1 day. All the cells were assembled in an inert atmosphere within an Ar-filled glove box. The galvanostatic measurements were performed at a current density of C/5 for PNZ, TA, and PNZTA on a battery test system (Won-A Tech, Korea). PNZ and TA were cycled in the voltage ranges of 1.2–2.7 V and 4.0–3.0 V *vs.* Na⁺/Na, and PNZTA was cycled in the voltage ranges of 1.0–2.7 V and 4.3–2.7 V *vs.* Na⁺/Na for the *n*-type redox reaction and *p*-type redox reaction, respectively. The symmetric cell was operated

at a current density of 50 mA g⁻¹ in the voltage range of 3.0-1.0 V.

3.2.5 Ex situ electrode characterization

The electrodes at the different states of charge were disassembled from coin cells, followed by rinsing with DME solvent. To prevent air exposure, all the electrodes were handled in an Ar-filled glove box. XPS measurements were performed using an Axis-Supra X-ray photoelectron spectrometer (Kratos, U.K.) equipped with an automated monochromatic X-ray source. All the obtained XPS spectra were referenced to the F 1s peak for PTFE at 690.6 eV. The FT-IR spectra were measured using pellets made of the electrodes and KBr powder on an FT/IR-4200 (Jasco, Japan) at a resolution of 4 cm⁻¹. For the XRD measurement, a D2 Phaser (Bruker, Germany) with Cu K α radiation ($\lambda = 1.5406 \text{ \AA}$) was used.

3.2.6 Computational details

The Gaussian 09 quantum chemistry package was used for spin-unrestricted density functional theory (DFT) calculations, including geometry optimization, eigenvalue calculation, energy evaluation, NPZ calculation, and vibration mode prediction for various molecules and their charged molecules.³⁰ For all the calculations, the Becke–Lee–Yang–Parr (B3LYP) hybrid exchange–correlation functional and triple-zeta valence polarization (TZVP) basis set were used.³¹⁻³⁶ The polarizable continuum model (PCM) scheme, an implicit solvation model, was applied to model the solvation environment of acetonitrile, which is the

common organic solvent. In the HOMO–LUMO plot, the Na^+/Na redox potential was set to -1.73 V *versus* the absolute vacuum scale (AVS) because the standard hydrogen electrode (SHE) is -4.44 V *versus* AVS and Na^+/Na is -2.71 V *versus* SHE.³⁷⁻³⁹

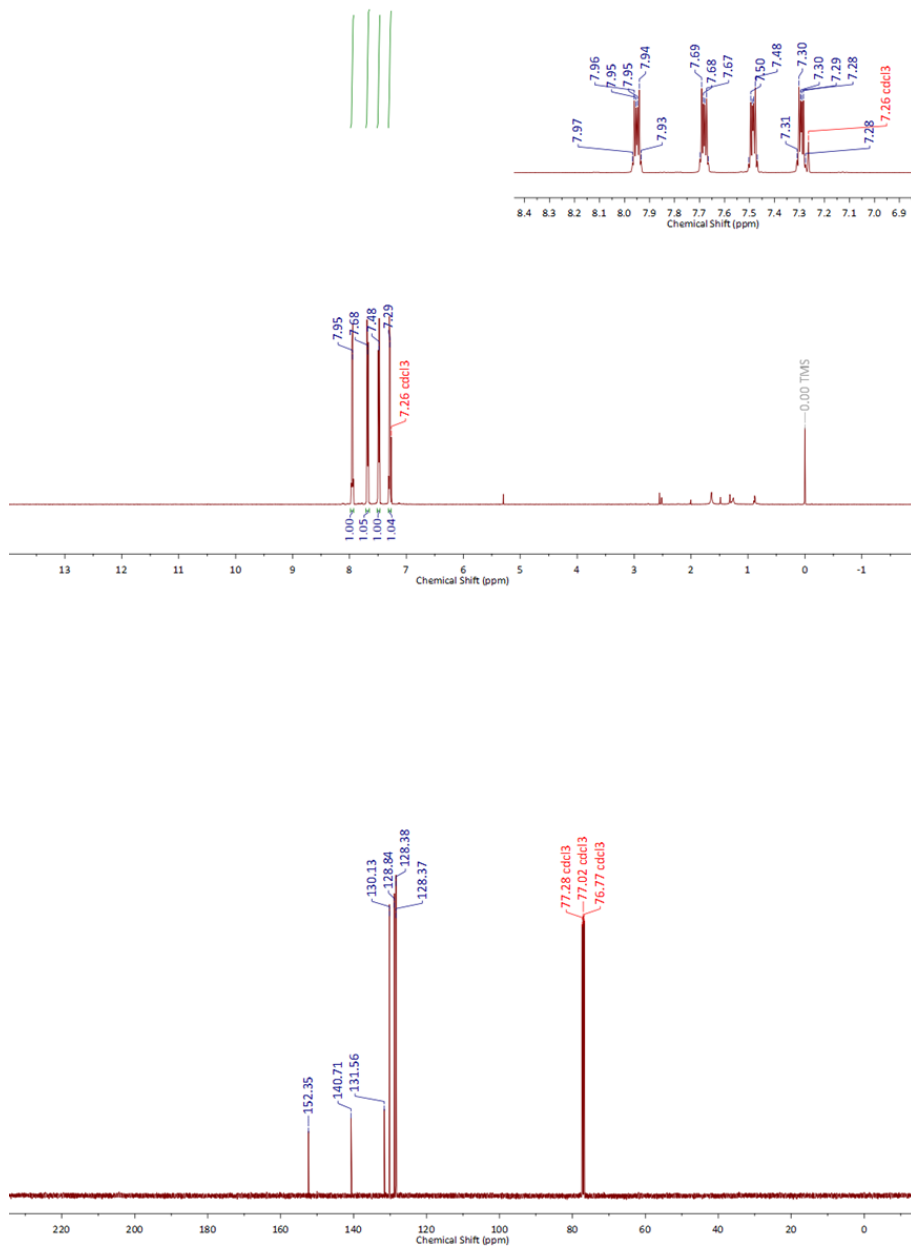


Figure 3.1. ¹H NMR (500 MHz, top) spectrum and ¹³C NMR (125 MHz, bottom) spectrum of PNZTA in CDCl₃ (*T* = 298 K)

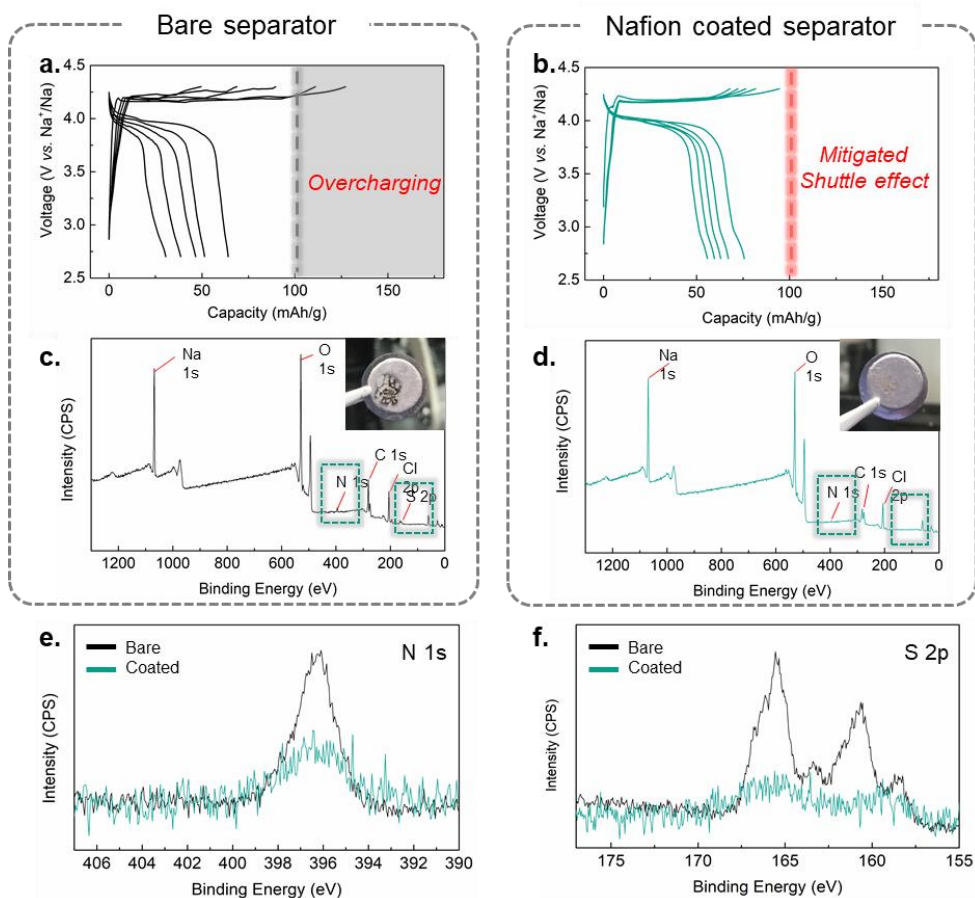


Figure 3.2. Preventing shuttle effect of PNZTA through separator engineering. a, b) Charge/discharge curves of *p*-type reaction of PNZTA utilizing celgard separator (a) and nafion coated separator (b). Overcharging due to the shuttle effect was mitigated after using nafion coated separator. c, d) XPS survey scan results and surface images for Na metal anode after charging the PNZTA half cells using celgard separator(c) and nafion coated separator (d). e, f) Comparison of XPS narrow scan results of N 1s (e) and S 2p (f) spectra from the results of c) and d). In the cell using only celgard separator, the nitrogen and sulfur which is originated

from PNZTA was found in the metal surface resulting in the contamination of metal surface. However, after using nafion coated separator, sodium metal retained a clean pristine surface after charging and none of nitrogen and sulfur was found in the surface, indicating the suppression of PNZTA migration from cathode to anode.

3.3 Results and discussions

3.3.1 Molecular design strategy for high voltage symmetric batteries

Herein, we propose a new general strategy for the design of bipolar organic materials based on *n*-type and *p*-type couples, taking advantage of their mutual electronic perturbation in a molecule without sacrificing the molecular weight toward high energy density symmetric cells.^{3,9} Specifically, we attempted to directly fuse an *n*-type redox motif with electron-withdrawing nature and a *p*-type redox center with electron-donating nature in a molecule. In such a way, it was intended that both *n*-type and *p*-type redox motifs mutually affect each other to alter the frontier molecular orbitals (FMOs) so that the bipolar redox activity can be displayed with a substantially widened highest occupied molecular orbital (HOMO) – lowest unoccupied molecular orbital (LUMO) energy gap, producing a high cell voltage. Moreover, the direct fusion was supposed to eliminate the need for an additional linker to hold the two redox centers in one molecule. It should be noted that the combination of two different types of organics has been generally implemented by a ‘p–linker–n’ strategy, where individual redox centers are simply linked *via* covalent bonds by a redox-inactive linker (Figure 3.3, right). This approach is the most intuitive synthetic method and has been adopted in the development of bipolar materials possessing the *p*-type and *n*-type active redox center together.^{25,40} With no apparent electronic conjugation, there exists minimal

perturbation of each redox center, and therefore the redox properties of each center are not altered or tailored. A reduction in the gravimetric energy density is usually caused by the presence of the redox-inactive linker in the structure.

We propose that the two redox components can be directly fused to produce a new π -extended platform by a so-called ‘*p-n* fusion’ strategy as illustrated in Figure 3.3a (left). In this case, the π -conjugation between the two redox centers would cause them to sensitively influence each other's redox chemistry, offering a route to alter the redox potentials. The *n*-type components are commonly electron-deficient, and thus can function as an electron-withdrawing functional group to the neighboring *p*-type redox center. Likewise, the electron-rich *p*-type components can serve as an electron-donating group to the *n*-type redox center. It implies that when the molecules are formed by the ‘*p-n* fusion’, the *p*-type and *n*-type redox centers would likely donate and withdraw the electron cloud mutually in the structure. When the *p*- and *n*-type motifs are properly chosen and fused, the mutual interaction is expected to elevate the redox potential of the *p*-type reaction while lowering the *n*-type redox potential. Furthermore, we postulated that this perturbation would become greater if the two motifs are brought closer in space within the fused molecule, as will be systematically verified in the following. It is also noteworthy that altering the redox potentials of molecules has been most frequently carried out by the use of functional groups;^{41,42} however, anchoring them in the mother molecules inevitably increases the overall molecular weight, and therefore, despite the enhancement of the redox potential, the gain in the energy

density remained marginal. It suggests that exploiting the mutual effects of the *p*- and *n*-type redox motifs in the fused molecule can be an alternative route which does not accompany the weight increase from the additional functional groups or linkers.

To implement this idea, we selected two well-known redox organic components, phenazine (PNZ) and thianthrene (TA), as a model *n*-type and *p*-type motif, respectively.^{43,44} Since there are various hypothetical molecules possible from the two motifs, we examined a series of molecules from the different fusion configurations/lengths with respect to the change in the energy levels of the HOMO and LUMO from density functional theory (DFT) calculations, as presented in Figure 3.4. It clearly indicates that as the distance between the redox centers of PNZ and TA gets shorter in the fused structures, the LUMO and HOMO levels notably increases and decreases, respectively. Since the LUMO and HOMO energy levels of the organic materials roughly reflect the redox potentials of *n*-type and *p*-type reactions, it suggests that the voltage in the symmetric batteries would become correspondingly elevated.^{45,46} The shift/separation of the energy level is attributable to the perturbations exerted on the redox-active FMOs,^{47,48} and its correlation with the distance proposes that the fused structure with the closest location of the two redox centers, *i.e.* the N-heterocyclic ring and the S-heterocyclic ring, respectively, would be the most suitable in achieving the highest cell voltage for symmetric batteries.

a. Molecular design strategy

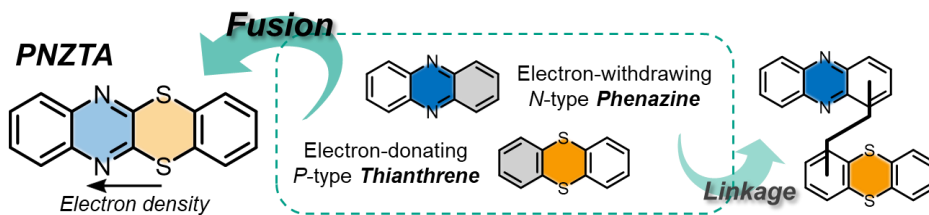


Figure 3.3. Molecular design strategy of PNZTA through the “P-linker-N” and “P-N fusion” of phenazine and thianthrene redox motifs.

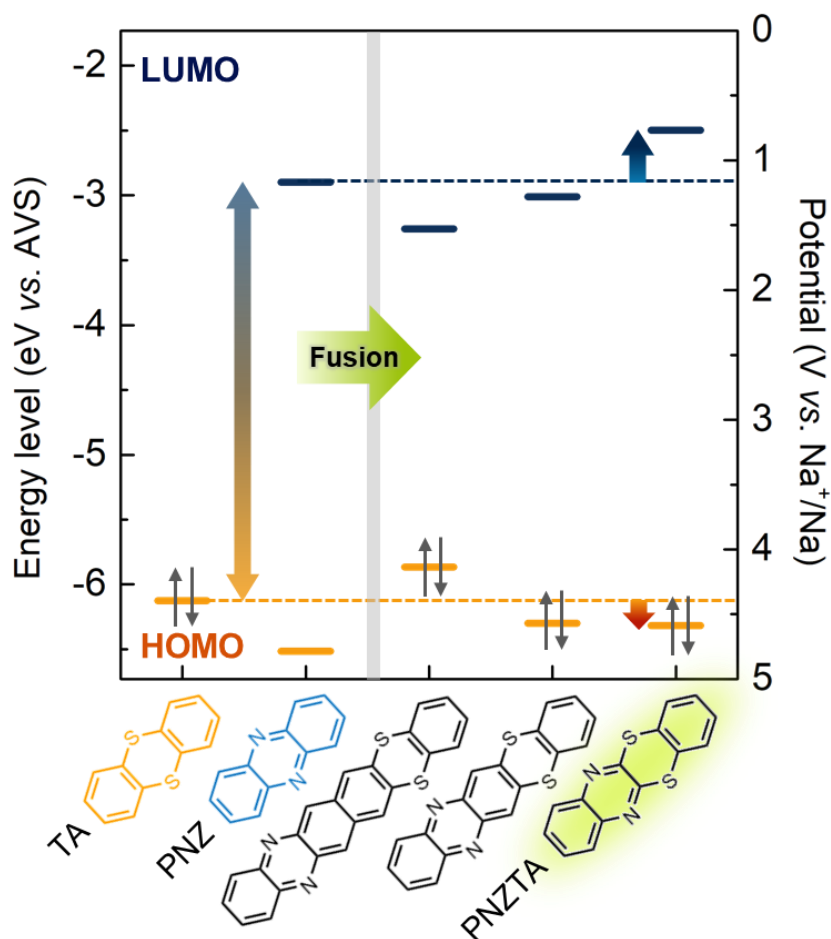


Figure 3.4. Calculated HOMO and LUMO level of TA, PNZ and various fused molecules of those motifs. The Na/Na⁺ redox potential was set to -1.73 V versus AVS because the standard hydrogen electrode (SHE) is -4.44 V versus AVS and Na/Na⁺ is -2.71 V versus SHE.

3.3.2 A new designed redox-active bipolar material, PNZTA

Based on this rationale, we targeted the molecule PNZTA in which an N-heterocyclic ring and an S-heterocyclic ring are fused adjacent to each other, as illustrated in Figure 3.3. The natural population analysis of the target PNZTA also supported that the charge density corresponding to ~ 0.06 electrons is polarized toward the PNZ motif from the TA side in PNZTA, manifesting the efficacy of our strategy to perturb the energy level of FMOs (Figure 3.5). It implies that the ‘less-electron-deficient’ *n*-type redox motif in PNZTA would display a lower reduction potential than that of the pristine PNZ, whereas the oxidation potential of the *p*-type redox motif would be higher than that of the pristine TA.^{41,49} In order to further verify the general applicability of our strategy, we additionally calculated the electronic structures of another hypothetically fused material utilizing dibenzo-1,4-dioxin (DD) or 10-methylphenothiazine (PTZ), a recently reported *p*-type redox center with an electron-donating nature, and PNZ (Figure 3.6 and 3.7).⁵⁰ The DFT calculations consistently revealed that as the redox-centers of DD and PNZ become closer in the fused structures, the LUMO and HOMO levels systematically increases and decreases, respectively. Moreover, the electron distributions were found to be shifted toward the electron-withdrawing PNZ motif from the DD region in PNZDD. The calculation results for fusion with PTZ and PNZPTZ also show the consistently shifted HOMO and LUMO energy levels. It indicates that the *p*-*n* fusion strategy may be adopted more universally in designing bipolar redox

materials by mutually tailoring the inherent electronic properties of *p* and *n*-type redox motifs.

Inspired by the theoretical findings, we synthesized the target PNZTA molecular compound, as described in Figure 3.28 and attempted to verify the redox activity and reversibility of PNZTA by the solution-based cyclic voltammetry (CV) measurements. Figure 3.9 evidently shows that PNZTA (green line) establishes the bipolar redox activity in an electrolyte system containing 0.1 M sodium perchlorate (NaClO₄) in acetonitrile (MeCN), displaying a reversible *n*-type reaction at -1.75 V and a *p*-type reaction at 1.2 V *versus* Ag/Ag⁺. It indicates that the reduction and oxidation capabilities were well preserved even after fusing the two redox motifs in a single molecule. Comparisons with the pristine PNZ and TA under the same CV conditions unveiled that the *n*-type redox potential of PNZTA decreased by 0.25 V compared with that of PNZ, whereas the *p*-type redox potential for PNZTA is higher by 0.3 V than that of TA, in a remarkable agreement with our prediction. The same voltage shifts were also observed in electrochemical systems using lithium-based electrolytes such as 0.1 M bis(trifluoromethane)sulfonamide lithium salt (LiTFSI) in MeCN in the CV experiments, as presented in Figure 3.10, signifying the intrinsic redox shifts of PNZTA regardless of the choice of the electrolyte. The galvanostatic test of the PNZTA electrode in a coin-type cell (Figure 3.11a, b) confirmed that the PNZTA electrode successfully undergoes reversible charge/discharge processes, exhibiting flat plateaus corresponding to the *p*-type and *n*-type reactions. Voltage shifts resulting from the fusion of the two

redox motifs were consistently observed in the galvanostatic test of the coin cell, whose differential capacity (dQ/dV) plot is depicted in the inset of Figure 3.9, in agreement with the CV results. The cycle performances of the PNZTA half-cell for the *n*-type and *p*-type reaction are plotted in Figure 3.11c, d. The capacity retention of PNZTA after 10 cycles for the *n*-type reaction was 54%, which was an improvement over the reference PNZ electrode (40%). For the *p*-type reaction, the PNZTA electrode also exhibited a slightly higher capacity retention of 45% compared with the TA electrode which showed 15% retention. This additional enhancement of the cycle performance is attributable to the reduced solubility of the fused molecular material (17 mM) compared with that of PNZ (95 mM) and TA (92 mM) in diethylene glycol dimethyl (DEGDME). We believe that the increased intermolecular force of the extended fused ring structure of PNZTA aids in the stability of the bulk material against the dissolution into the electrolyte solution, as described in detail in Figure 3.12. Nonetheless, further improvement of the performances is still required to achieve a level comparable to that of currently reported organic electrode materials by the optimization of the cell systems.^{51,52}

The bipolar redox activity of PNZTA could be elucidated by the analysis of the charge redistributions observed for PNZTA, $\text{PNZTA}^{\cdot-}$, and $\text{PNZTA}^{\cdot+}$ (Figure 3.13). The numbers indicated in Figure 3.13a are the sum of the atomic charges for the PNZ motif (blue) and TA motif (orange), respectively. It was found that 74.3% of the negative charge resides in the N-heterocyclic ring upon one-electron reduction of PNZTA, implying that PNZ functions as the main electron

reservoir during the discharge or the *n*-type reaction. On the other hand, when PNZTA is oxidized to produce a net +1 charge, the S-heterocyclic ring region takes up +0.818 charge, indicating that the TA motif is the main reaction site of the *p*-type reaction. Additionally, the bond lengths in the N-heterocyclic ring and S-heterocyclic ring were found to change noticeably in the *n*-type and *p*-type reaction, respectively, as plotted in Figure 3.14, which is consistent with the results of natural population analysis.

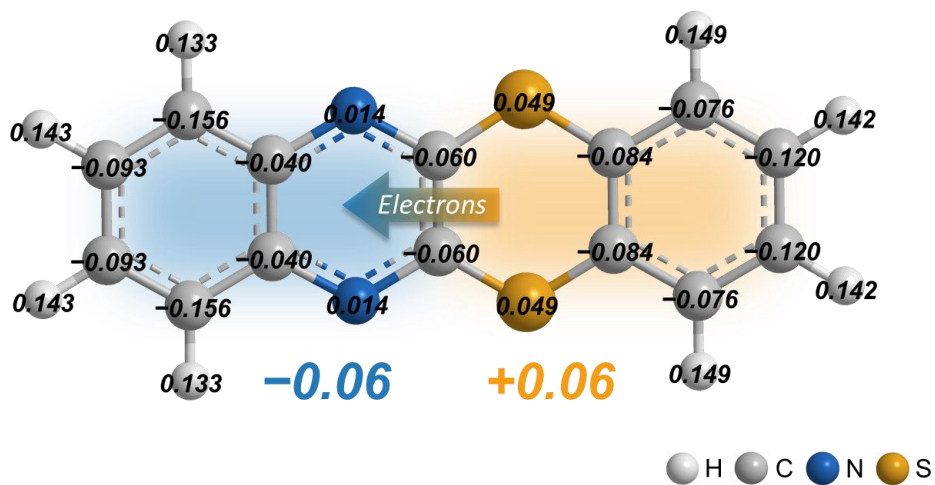


Figure 3.5. Charge distribution calculation of PNZTA using natural population analysis.

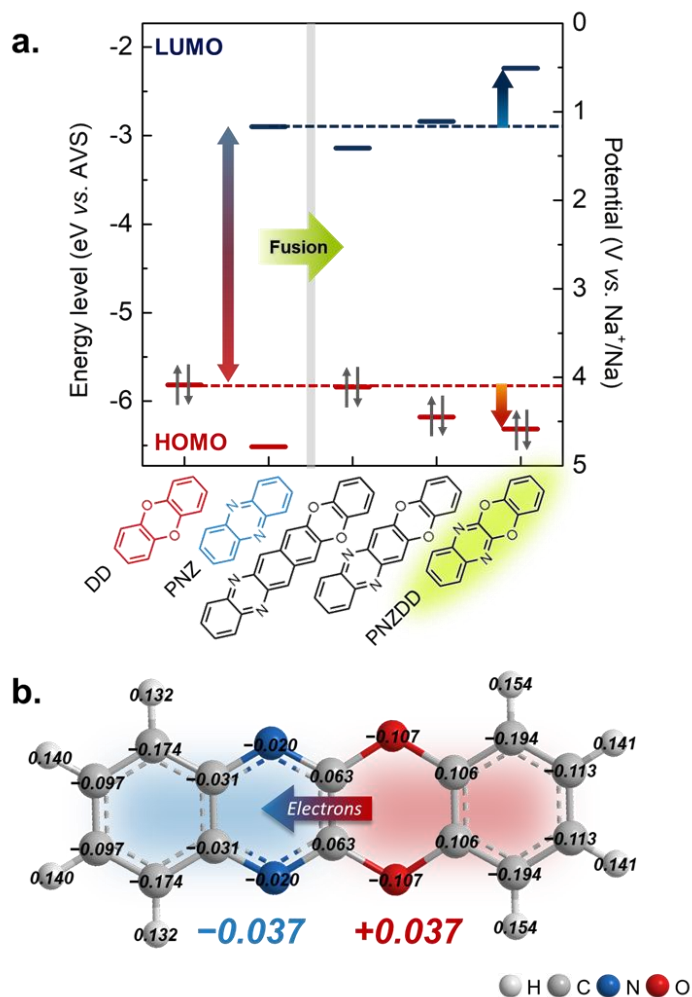


Figure 3.6. The *p-n* fusion of DD and PNZ. a) Calculated molecular orbital energies (HOMO and LUMO) of DD, PNZ and various fused molecules of those motifs. The Na/Na⁺ redox potential was set to -1.73 V versus AVS because the SHE is -4.44 V versus AVS and Na/Na⁺ is -2.71 V versus SHE. b) Charge distribution calculation of PNZDD using natural population analysis.

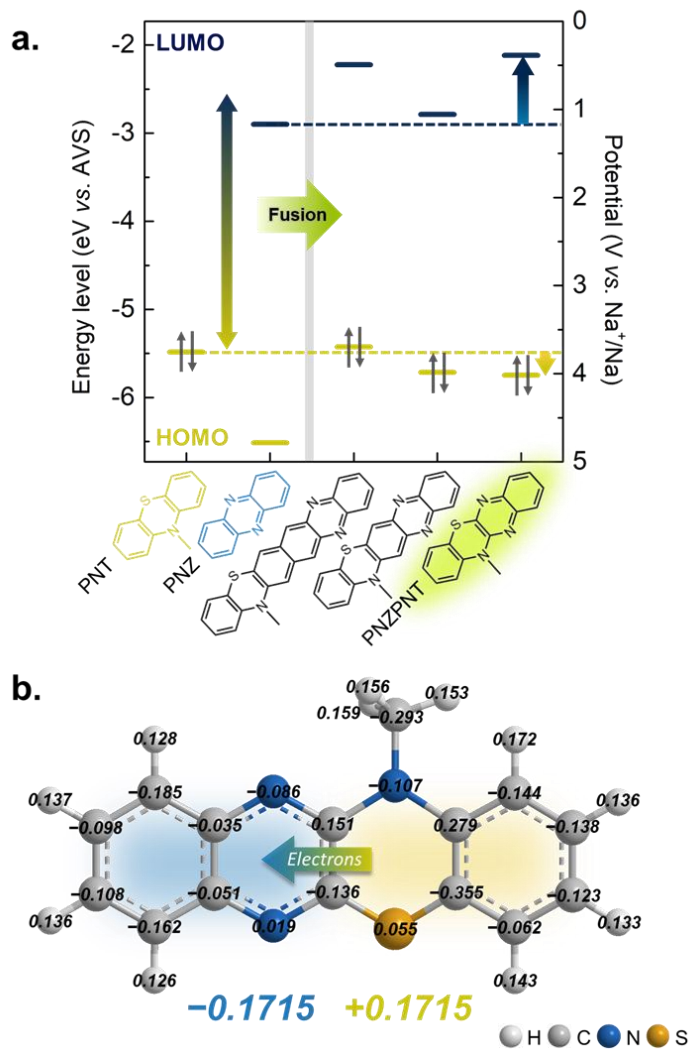


Figure 3.7. The p - n fusion of PTZ and PNZ. a) Calculated molecular orbital energies (HOMO and LUMO) of PTZ, PNZ and various fused molecules of those motifs. b) Charge distribution calculation of PNZPTZ using natural population analysis.

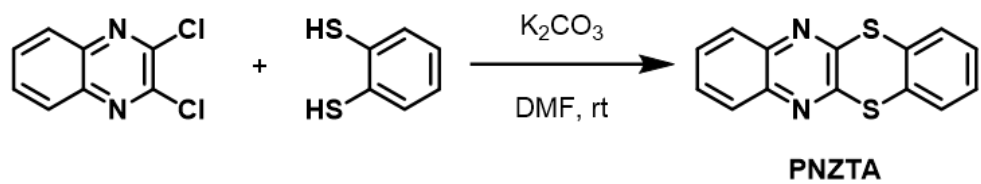


Figure 3.8. Synthetic scheme for PNZTA.

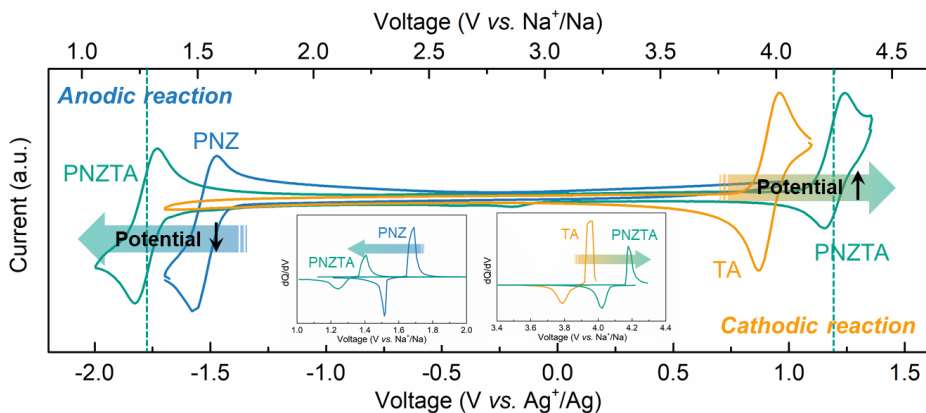
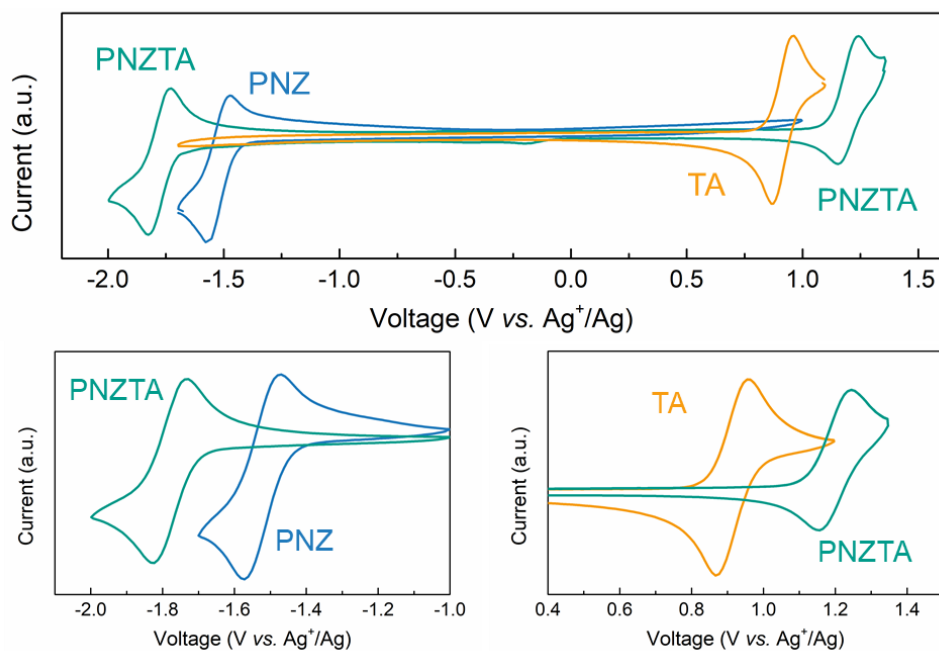


Figure 3.9. CV curves of PNZ (blue), TA (orange), and PNZTA (green), which presents bipolar redox activity with widened potential gap in the fused material. dQ/dV curves of PNZ, TA, and PNZTA, corresponding to the sodium half-cell charge/discharge profile, are presented in the inset.

a. 0.1 M NaClO₄ MeCN



b. 0.1 M LiTFSI MeCN

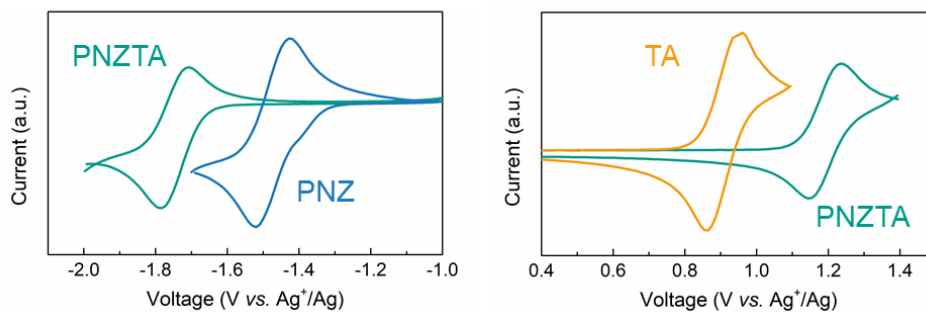


Figure 3.10. CV results of PNZ, TA and PNZTA in various electrolyte system. a) 0.1 M NaClO₄ in MeCN, b) 0.1 M LiTFSI in MeCN

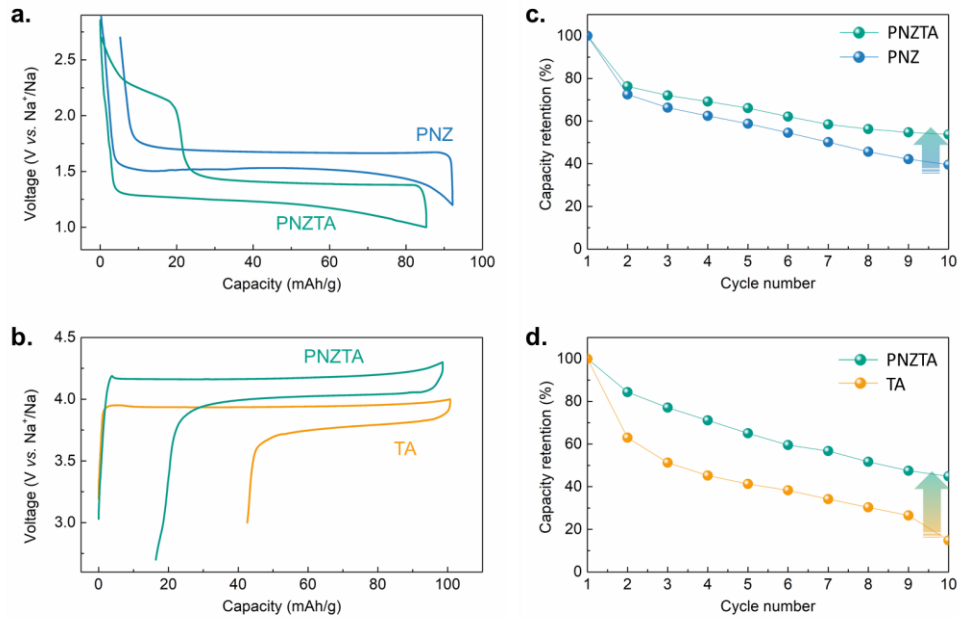


Figure 3.11. Galvanostatic charge/discharge profile and capacity retention curves of PNZ, TA, and PNZTA half-cell at a current density of $C/5$. a, c) The n -type redox reaction of PNZ and PNZTA. b,d) The p -type redox reaction of TA and PNZTA.

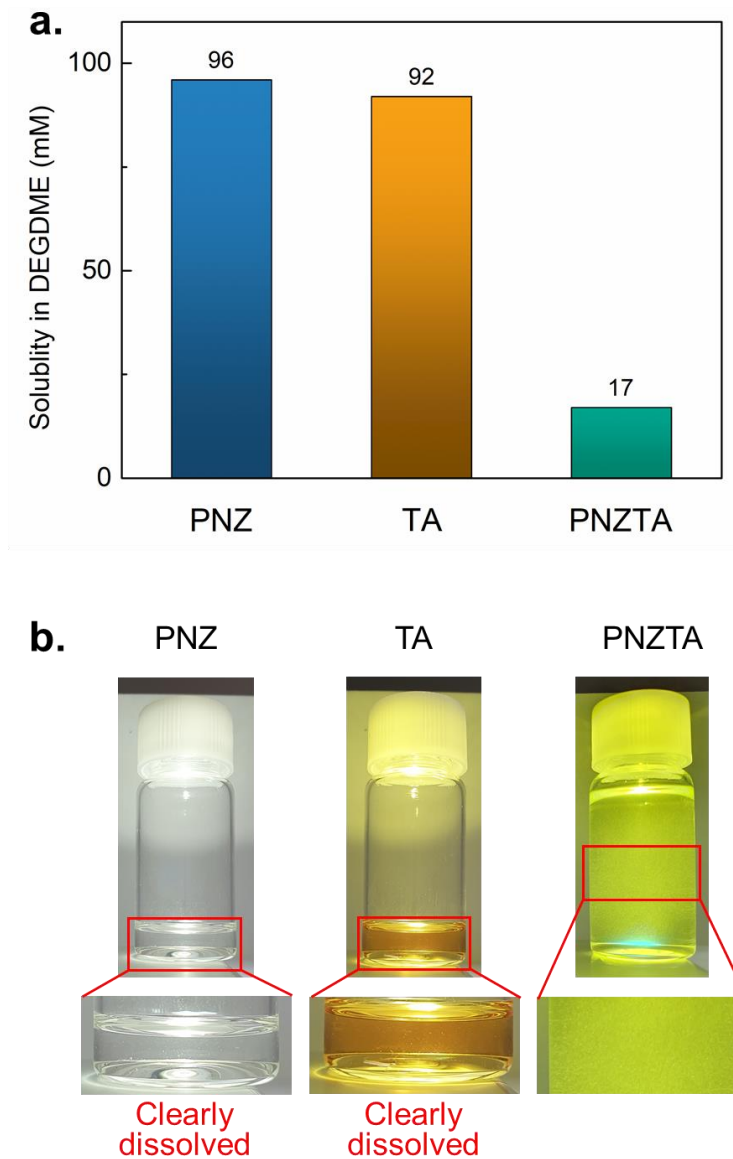


Figure 3.12. Solubility test for PNZ, TA and PNZTA. a) Powder solubility of PNZ, TA and PNZTA in DEGDEM solvent which was used in this paper b) Images of solvent after dissolving each material. PNZTA showed significantly low solubility than PNZ and TA.

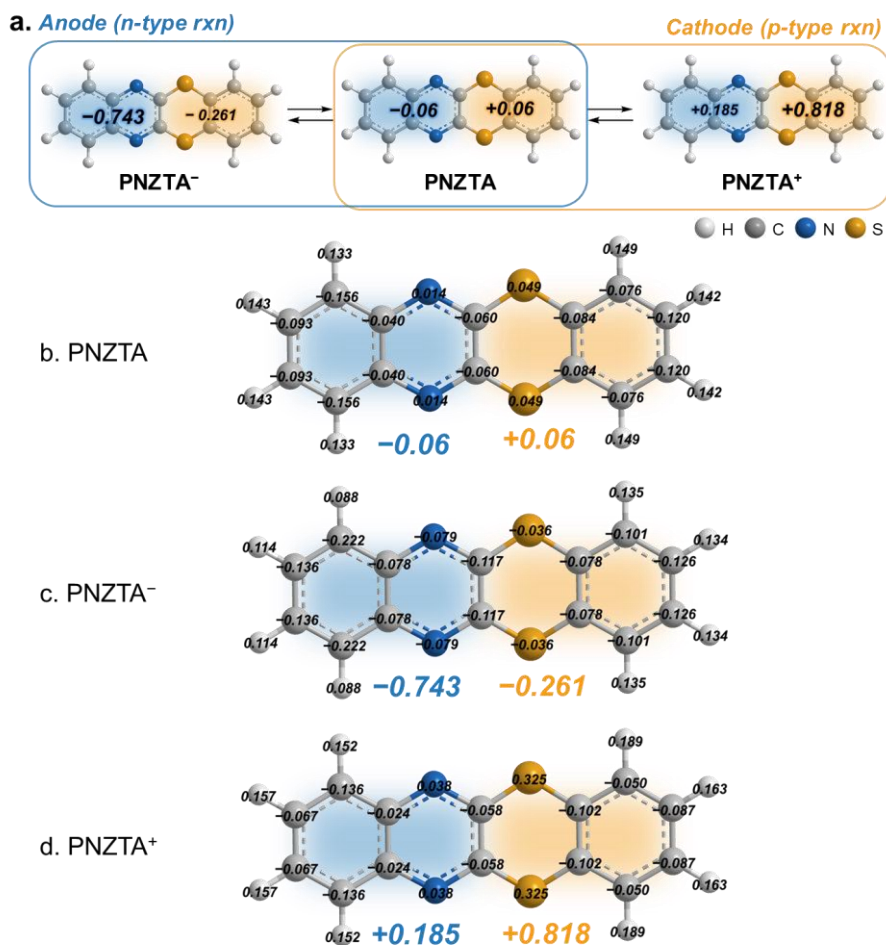


Figure 3.13. a) Expected reaction scheme for the n-type and p-type redox reaction and changes of the calculated charge distributions upon each reaction. b,c,d) Charge distribution calculations of PNZTA (b), PNZTA⁻(c), and PNZTA⁺(d) using natural population analysis. The numbers on each atom denotes the calculated atomic charges. The numbers under each molecule are the sum of atomic charges which corresponding to the phenazine motif (blue) and the thianthrene motif (orange), respectively.

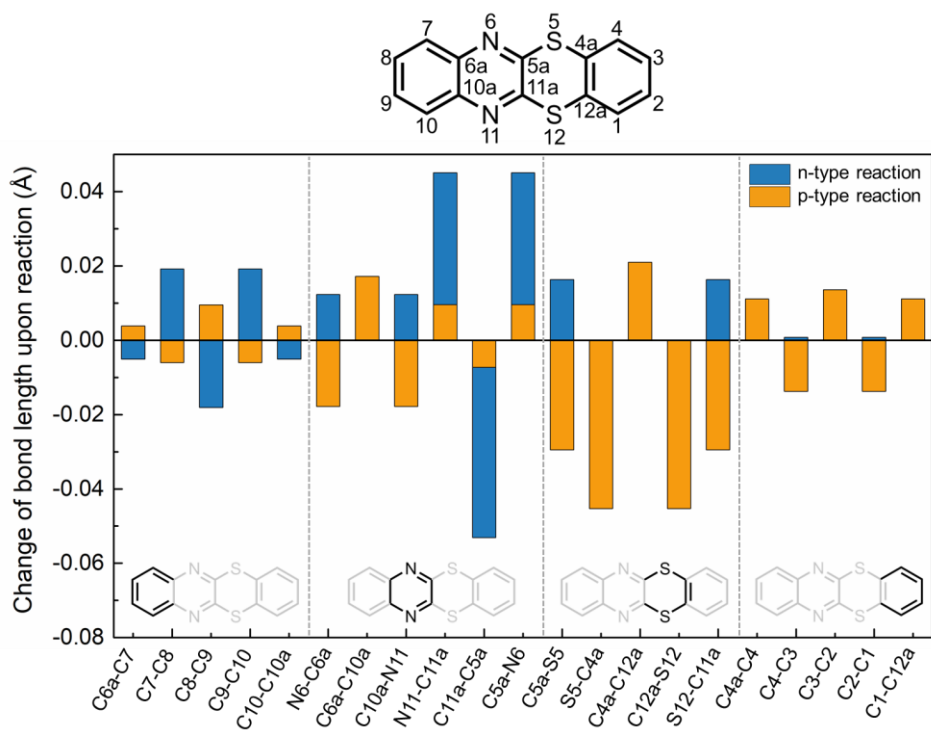


Figure 3.14. The bond length changes of PNZTA upon reduction (that is *n*-type reaction, blue bar) and oxidation (that is *p*-type reaction, orange bar)

3.3.3 Redox mechanism of PNZTA upon *n*-type reaction

We investigated the redox mechanism of the PNZTA electrode more closely by the ex situ characterization studies of the electrodes. Figure 3.15a shows the X-ray photoelectron spectroscopy (XPS) spectra for the pristine, reduced, and re-oxidized electrodes during the *n*-type reaction. Note that, for the *n*-type reaction, the galvanostatic protocol was set to first discharge and then re-charge within 1.0-2.7 V (vs. Na⁺/Na). The figure shows that the Na 1s peak, which was not observed for the pristine electrode, is detected upon reduction and disappears again with re-oxidation, which indicates the reversible insertion and deinsertion of sodium ions during the *n*-type reaction.^{53,54} The sodium insertion/deinsertion was accompanied by the changes in the binding nature of the nitrogen and sulfur atoms in PNZTA. The N 1s peak at 400.1 eV and the S 2p peaks at 165.8 and 164.6 eV corresponding to the S 2p_{1/2} and S 2p_{3/2} spin-orbit states are shifted to lower binding energy states upon reduction, which are reversed after the re-oxidation, suggesting that they are likely the redox sites during the *n*-type reaction, in consistent with the natural population analysis in Figure 3.13a. However, a closer inspection of the spectra revealed that the changes are slightly different for the N 1s and S 2p peak evolutions. The overlapped spectra of each peak in Figure 3.15a (bottom) illustrate that the overall shift of the N 1s peak was due to the broadening of the peak toward a lower binding energy, whereas the S 2p spectra simply shifted toward a lower energy without broadening upon reduction. The deconvolution of the N 1s peak unveiled that the peak broadening is ascribed to a new peak arising at 399.5 eV in

addition to the original peak at 400.1 eV. The additional peak at 399.5 eV is attributed, taken together with the changes of the Na 1s spectra, to the ionic interaction between the reduced nitrogen and intercalated sodium cations according to previous reports.^{8,50,54} On the other hand, the shift of the S 2p spectra without a significant broadening presumably reflects the delocalization of the injected electron upon discharge. Considering the above natural population analysis results, it suggests that the N-heterocyclic ring from the PNZ motif is the main sodium insertion site for the *n*-type reaction, while the delocalization of the charge also influences the bonding nature of sulfur in the TA motif. It is further supported by ex situ Fourier-transform infrared spectroscopy (FT-IR) analysis, which probes the change in the bonding nature of the structure during the *n*-type reaction. Figure 3.15b and Figure 3.16 depict that the absorptions at 1385, 1255, 1180, and 1110 cm⁻¹ corresponding to the vibrational modes involving nitrogen atoms markedly change during the *n*-type redox reaction. It shows that the double-bond character of N=C-C in the N-heterocyclic ring notably weakens upon the reduction of the electrode, which is reversed during the oxidation.

To further understand the structural transitions accompanying the *n*-type reaction, we conducted combined DFT and X-ray diffraction (XRD) studies at several states of charge (SOCs). Figure 3.15c shows the side view of the molecular structures of PNZTA and PNZTA⁻, which were predicted from the DFT calculations. The structure of the neutral PNZTA adopts a slightly bent conformation in the S-heterocyclic ring with an interplanar angle of 135°, which

agrees with our single-crystal X-ray structure analysis reporting an interplanar angle of 137.12° (Figure 3.17 and Table 3.1). After the reduction of PNZTA to PNZTA^- , a small change in the conformation angle was observed (interplanar angle = 131.7°); however, the overall bent configuration was maintained, implying the minimal structural change in the molecular crystal. This result is in consistent with the change of XRD patterns, as presented in Figure 3.15d, where the overall change in the main peaks of the pristine PNZTA electrode was not significant during the *n*-type reaction. Comparison of the peak position in Figure 3.15d (right) revealed that the main peak of PNZTA gradually shifts to smaller 2θ values upon sodium-ion insertion, indicating the expansion of the lattice when accommodating the sodium ions. A reversible lattice contraction was confirmed during the desodiation, displaying the continuous shift of the peaks to the original positions, which supports the intercalation behavior of sodium ions into the PNZTA crystal structure.

	PNZTA
Chemical formula	$C_{14}H_8N_2S_2$
Formula weight	268.34
Crystal system	triclinic
Space group	P-1
Color of crystal	fluorescence yellow
a (Å)	6.9896(3)
b (Å)	9.2152(4)
c (Å)	9.6542(3)
α (°)	100.010(3)
β (°)	94.635(3)
γ (°)	105.365(3)
Volume (Å ³)	585.19(4)
Z	2
R(int)	0.0281
Final R indices [$I > 2\sigma(I)$]	$R_1 = 0.0408$, $wR_2 = 0.1205$
Final R indices [all data]	$R_1 = 0.0418$, $wR_2 = 0.1216$
GOF	1.090

Table 3.1. Summary of X-ray crystallographic data.

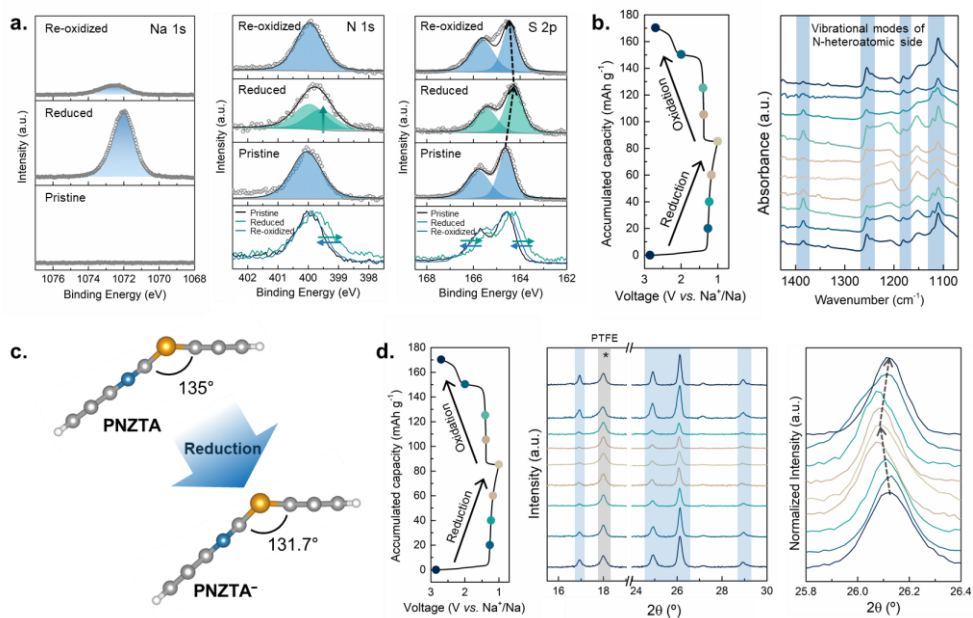
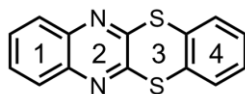


Figure 3.15. Investigation of redox mechanism for *n*-type redox reaction of PNZTA. a) Ex situ Na 1s, N 1s, and S 2p XPS spectra. b) Voltage-capacity profile of *n*-type reaction for PNZTA and corresponding eV FT-IR spectra. c) Side view of molecular structures of PNZTA and PNZTA⁻ with folding angle obtained by DFT calculation. d) Ex situ XRD patterns during the *n*-type redox reaction.



Wavenumber (cm ⁻¹)	Vibrational mode
433	Wagging of C-C-C, C-N=C, C-S-C, and C-C-C bonds in ring 1,2,3, and 4 respectively
612	In-plane scissoring of C-C-C bonds in ring 1
1125	In-plane symmetrical stretching of C-C-C bonds in between ring 3 and 4 In-plane asymmetrical stretching of C-C-S bonds in ring 3
1137	In-plane symmetrical stretching of C-C-C bonds in between ring 1 and ring 2 In-plane asymmetrical stretching of C-C-N bonds in ring 2
1152	In-plane scissoring of C-C-C bonds in ring 1 In-plane scissoring of C-N=C bonds in ring 2
1199	In-plane scissoring of C-C-H bonds in ring 1
1285	In-plane asymmetrical stretching of C-C=C bonds in ring 1 In-plane asymmetrical stretching of C-N=C bonds in ring 2
1392	In-plane asymmetrical stretching of C-C=C bonds in ring 1 In-plane asymmetrical stretching of C-C=N bonds in between ring 1 and 2

Figure 3.16. Peak assignments for FTIR spectra.

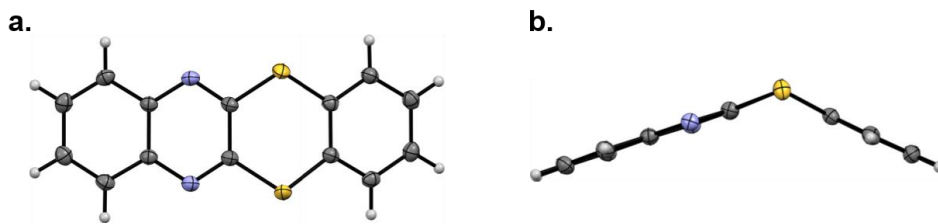


Figure 3.17. X-ray structure of PNZTA: a) top view and b) side view.

3.3.4 Redox mechanism of PNZTA upon *p*-type reaction

Subsequently, we probed the redox mechanism of the *p*-type reaction in the PNZTA electrode. Figure 3.18 shows the results of ex situ characterization studies carried out with the galvanostatic protocol set to first charge the PNZTA electrode, followed by the discharge within 4.3-2.7 V (*vs.* Na⁺/Na). The XPS spectra display a significant increase and decrease in the intensity of the Cl 2p peak upon oxidation and re-reduction, respectively (Figure 3.18a). The changes in the Cl 2p spectra indicate that the electrode reaction involving ClO₄⁻ ions takes place during the *p*-type reaction, as the oxidation of the PNZTA electrode entails the uptake of anions to compensate for the charge. Both S 2p and N 1s spectra showed that the original peaks were shifted toward higher binding energy states when the electrode was charged.¹² Moreover, new peaks appeared at higher binding energy in both S 2p and N 1s spectra, which is presumed to arise from newly formed radical cations during the oxidation.⁵⁵

DFT computational studies could elucidate the origin of this concurrent change of peaks in the S 2p and N 1s spectra. Figure 3.18b shows that the PNZTA molecule undergoes a significant conformational change upon the *p*-type redox reaction, illustrating essentially planar configurations (*i.e.*, an interplanar angle of 180°) with significant S=C double-bond character. Such a planar geometry of the molecule develops an extended π -conjugation area and promotes the charge delocalization over the PNZTA molecule.⁵⁶ We suspect that the simultaneous shift and peak formation of the S 2p and N 1s spectra during the *p*-type reaction is

attributed to the flattening of the molecule and resulting delocalization of the fused ring system. Ex situ FT-IR analysis also supports the anion incorporation during the *p*-type reaction (Figure 3.18c). A broad peak was detected at approximately 1070 cm^{-1} upon charging, corresponding to the vibrational mode of ClO_4^- , and diminished upon discharge, indicating the reversible incorporation and release of the ClO_4^- anions.^{57,58} The ex situ XRD study in Figure 3.18d shows that significant changes in the crystal structure occur during the *p*-type electrochemical reaction. It illustrates that the peak intensity of the pristine PNZTA markedly decreased upon charging, whereas new peaks evolved at 25.1° and 26.4° (green dotted box), indicating the formation of a new phase. While the identification of the new phase was not trivial, the origin of this new phase is suspected to be caused by the flattening of the PNZTA molecules upon oxidation.⁵⁹ Large conformational changes in the molecule level would energetically necessitate the rearrangement of molecules in a substantially different manner and lead to the phase transition involving the evolution of a new phase.⁶⁰

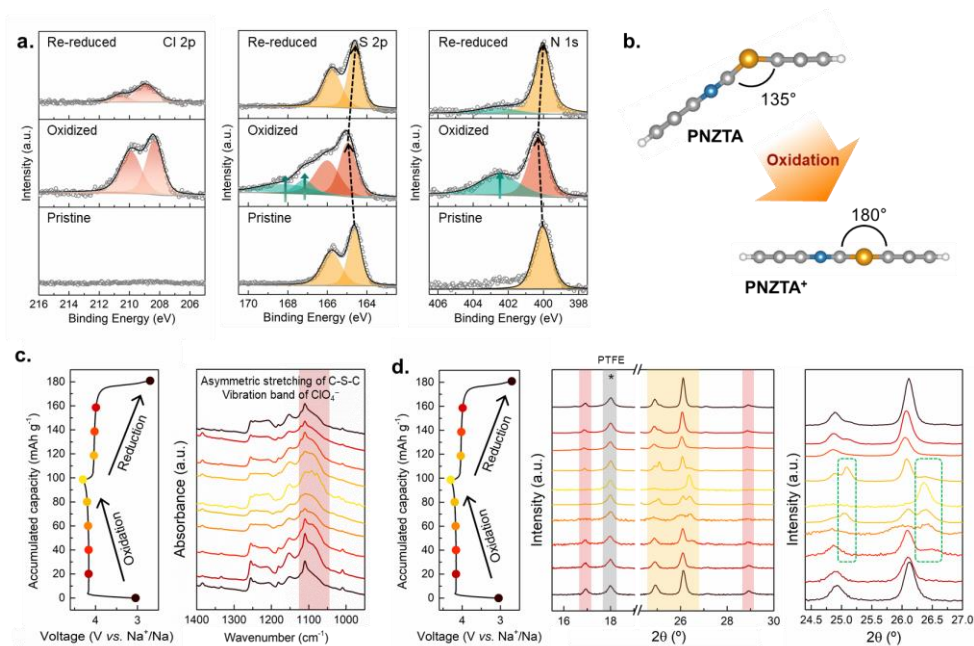


Figure 3.18. Investigation of redox mechanism for *p*-type redox reaction of PNZTA. a) Ex situ Cl 2p, S 2p, and N 1s XPS spectra. b) Side view of molecular structures of PNZTA and PNZTA⁺ with folding angle, which showed significant conformational change. c) Voltage-capacity profile of *n*-type reaction for PNZTA and corresponding FT-IR spectra. d) Ex situ XRD patterns during the *p*-type redox reaction.

3.3.5 Electrochemical performance of PNZTA symmetric cell

We finally assembled a symmetric cell employing PNZTA electrodes for both the cathode and anode and investigated its electrochemical performance in comparison to that of the reference cell. Figure 3.19a shows the galvanostatic charge/discharge curves after the activation cycle. The figure (top) depicts the electrochemical profile of a reference cell composed of the PNZ anode and TA cathode, and the bottom plot is that of a PNZTA symmetric cell. The reference cell (PNZ||TA) exhibits a voltage of 2.11 V, in consistent with the previous reports of each redox potentials, delivering an initial capacity of $39 \text{ mA h g}_{\text{cathode}}^{-1}$.^{43,44} On the other hand, we found that the PNZTA symmetric cell is capable of presenting a notably higher cell voltage of approximately 2.33 V. It indicates that the tailored redox potentials of *n*-type and *p*-type reactions could be obtained from the PNZTA electrode, in consistent with the CV results, leading to a higher cell voltage. Moreover, the symmetric cell could deliver a capacity of $63 \text{ mA h g}_{\text{cathode}}^{-1}$, which is 1.6 times greater than that of the pristine PNZ and TA electrodes, with an improved cycle stability. Since the fused PNZTA manifested improved cycle performance compared to the PNZ and TA, respectively in the half-cell, it is valid that the PNZTA symmetric cell showed better cycle performance than the PNZ||TA cell in the initial cycles.

The overall performance of the PNZTA symmetric cell was compared with those of previously reported symmetric cells, with respect to the cell voltage and corresponding energy densities in Figure 3.19b (see also Table 3.2). It

illustrates that the PNZTA symmetric cell exhibits one of the highest cell voltages among reported symmetric cells, including both inorganic and organic electrode materials.^{17-25,61-68} Compared with the performance of the cell built with PNZ and TA as the anode and cathode, respectively, the fused molecular structure of PNZTA could offer a two times higher energy density of $173 \text{ W h kg}_{\text{cathode}}^{-1}$ (when calculated based on the voltage and the capacity corresponding to one electron-transfer reaction per molecule). It should be noted that, although the chemical structure of PNZTA suggests the feasibility of multi-electron redox chemistry, further oxidation of $\text{PNZTA}^{+\cdot}$ or reduction of $\text{PNZTA}^{-\cdot}$ was limited by the electrochemical window of the electrolyte in our study (Figure 3.20). Nevertheless, we expect that the use of higher performing electrolytes with wide electrochemical windows would enable PNZTA to achieve the multi-electron transfer in a symmetric cell as well as to improve the cycle stability of the symmetric cell (Figure 3.21). In turn, the PNZTA symmetric cell would possess twice the energy density reported in this study, as indicated by the opaque star in Figure 3.19b.⁶⁹

Compounds	Average Voltage (V)	Capacity (mAh/g, based on the weight of one electrode)	Reference
$\text{Li}_7\text{V}_{15}\text{O}_{36}(\text{CO}_3)$	1.2	120	1
$\text{Na}_3\text{MnTi}(\text{PO}_4)_3$	1.3	57.9	2
$\text{Li}_{1.5}\text{Cr}_{0.5}\text{Ti}_{1.5}(\text{PO}_4)_3$	2.15	32	3
$\text{Na}_3\text{V}_2(\text{PO}_4)_3$	1.8	90.2	4
$\text{Na}_2\text{LiV}_2(\text{PO}_4)_3/\text{C}$	1.08	95	5
$\text{Na}_{0.8}\text{Ni}_{0.4}\text{Ti}_{0.6}\text{O}_2$	2.8	85	6
$\text{Na}_{0.6}\text{Cr}_{0.6}\text{Ti}_{0.4}\text{O}_2$	2.53	74	7
$\text{Na}_2\text{VTi}(\text{PO}_4)_3$	1.2	72	8
$\text{Na}_3\text{Co}_{0.5}\text{Mn}_{0.5}\text{Ti}(\text{PO}_4)_3$	1.4	43	9
$\text{Na}_3\text{V}_2(\text{PO}_4)_2\text{F}_3/\text{C}$	2.53	107	10
$\text{Li}_3\text{V}_2(\text{PO}_4)_3/\text{C}$	1.85	87	11
$\text{Na}_4\text{C}_8\text{H}_2\text{O}_6$	1.8	198	12
$\text{K}_3\text{C}_6\text{O}_6$	1.1	70	13
$\text{Na}_4\text{C}_6\text{O}_6$	0.65	167	14
$\text{Li}_4\text{C}_8\text{H}_2\text{O}_6$	1.8	208	15
$\text{C}_{52}\text{H}_{62}\text{N}_4\text{O}_{23}\text{Li}_4$	2.5	53	16
$\text{Li}_4\text{C}_6\text{O}_6$	0.65	178	17

Table 3.2. Performance of previous reported symmetric cells. The energy densities of the symmetric cells were estimated with respect to the weight of one electrode.

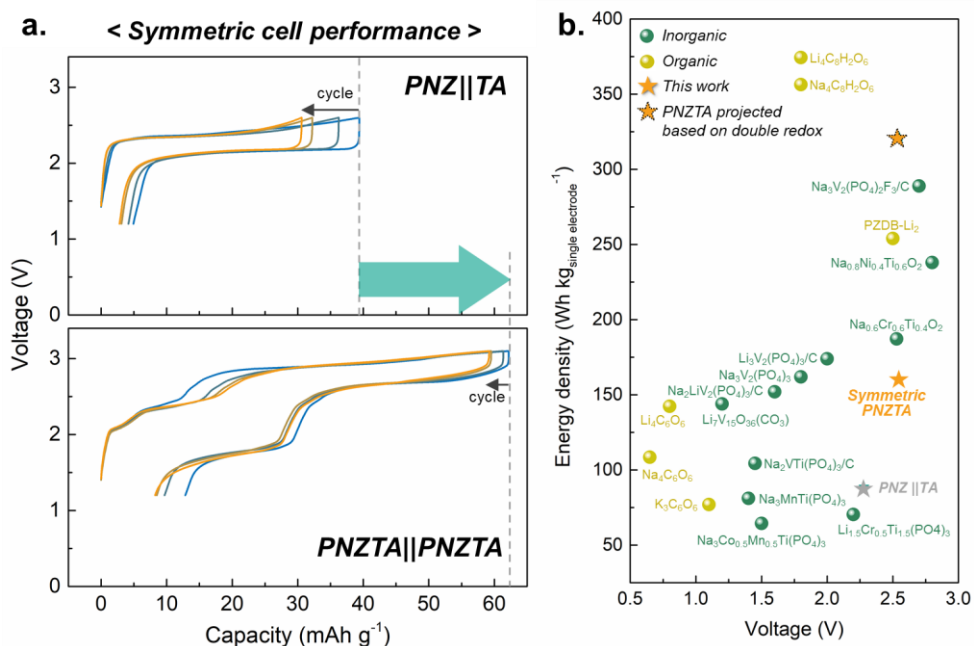


Figure 3.19. Electrochemical performance of the symmetric cell. (a) Comparison of charge–discharge curves of the battery using PNZ and TA as the cathode and anode, respectively, and that of the symmetric battery exploiting PNZTA as the active materials for both electrodes simultaneously. (b) Symmetric cell voltage and energy density plot of reported symmetric batteries utilizing inorganic (green) and organic (yellowish-green) active materials. The energy density was calculated as the product of the voltage of the symmetric cell and the capacity based on the weight of one electrode.

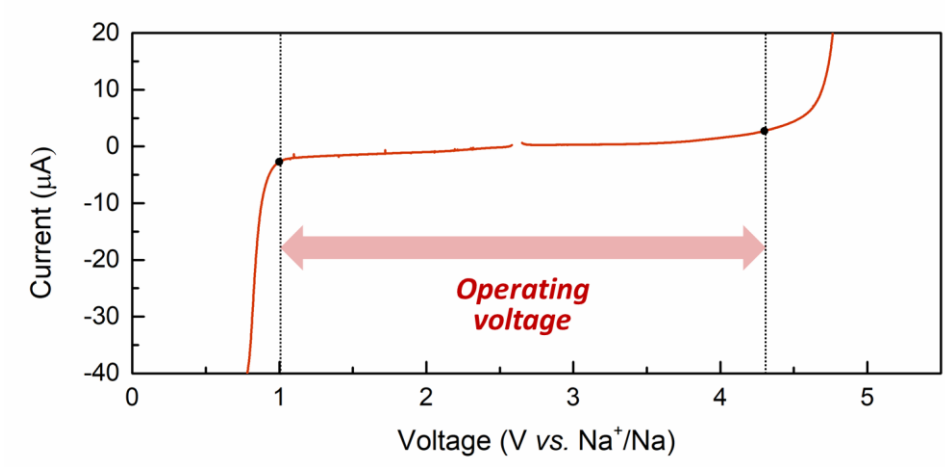


Figure 3.20. Linear sweep voltammetry (LSV) curves of Na metal / 3.5 m NaClO₄ in DEGDME / SUS cell.

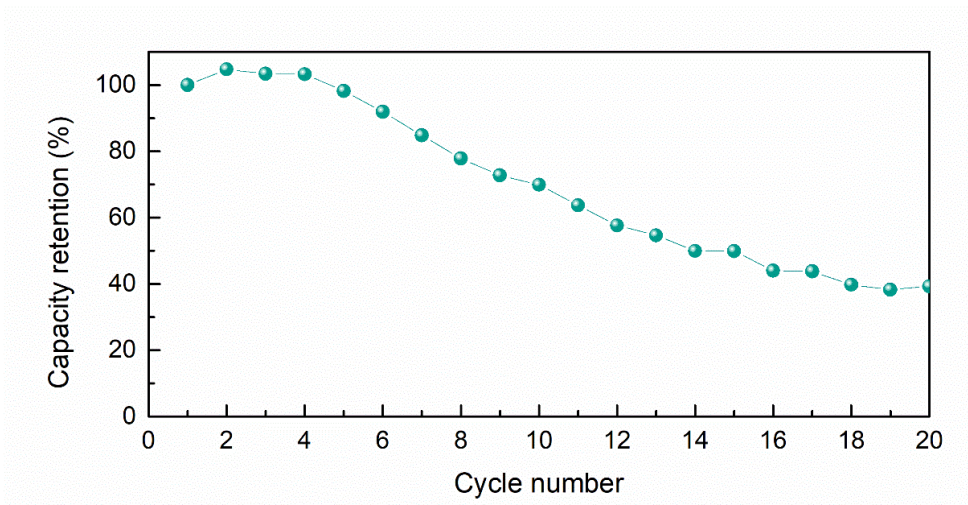


Figure 3.21. Capacity retentions of PNZTA symmetric cell after the activation cycle.

3.4 Concluding remarks

We proposed a new strategy to develop bipolar materials for high energy density symmetric batteries by fusing an *n*-type redox motif with electron-withdrawing character and a *p*-type redox motif with electron-donating character. A newly designed bipolar material, PNZTA, exhibited bipolar redox activity, enabling the assembly of a symmetric battery system. It was revealed that upon fusion, the charges were polarized toward the *n*-type redox center, resulting in a lower *n*-type redox potential and higher *p*-type redox potential than those of the individual redox motifs through the electron delocalization and inductive effects of the two motifs. We comparatively analyzed the *n*-type and *p*-type redox mechanism of PNZTA from the chemical and structural viewpoints. It was found that the N-heterocyclic ring, the main motif from PNZ, was responsible for the *n*-type redox reaction with the reversible sodium ion intercalation, while the main locus of the *p*-type redox reaction was detected in the S-heterocyclic ring. Additionally, a large structural transformation was identified during the *p*-type redox reaction, which was attributed to the significant changes in the molecular geometry upon oxidation. An all-organic symmetric cell exploiting the PNZTA compound was successfully demonstrated, delivering a cell voltage of 2.75 V, which is one of the highest cell voltages of reported symmetric batteries. Although, further development of a stable electrolyte and optimization of the electrode composition are required for the practical application of this system; this study not only provides a novel strategy for the design of bipolar materials for high-voltage symmetric batteries but also

offers the insight into the distinct n -type and p -type redox reactions in a same host material.

3.5 References

- 1 Larcher, D. & Tarascon, J. M. Towards greener and more sustainable batteries for electrical energy storage. *Nat. Chem.* **7**, 19-29, (2015).
- 2 Van Noorden, R. The rechargeable revolution: A better battery. *Nature* **507**, 26, (2014).
- 3 Lu, Y. & Chen, J. Prospects of organic electrode materials for practical lithium batteries. *Nat. Rev. Chem.* **4**, 127-142, (2020).
- 4 Lee, S., Hong, J. & Kang, K. Redox-Active Organic Compounds for Future Sustainable Energy Storage System. *Adv. Energy Mater.* **10**, 2001445, (2020).
- 5 Chen, H. *et al.* From Biomass to a Renewable LiXC6O6 Organic Electrode for Sustainable Li-Ion Batteries. *ChemSusChem* **1**, 348-355, (2008).
- 6 Hu, P. *et al.* Renewable-Biomolecule-Based Full Lithium-Ion Batteries. *Adv. Mater.* **28**, 3486-3492, (2016).
- 7 Lee, B. *et al.* Exploiting Biological Systems: Toward Eco-Friendly and High-Efficiency Rechargeable Batteries. *Joule* **2**, 61-75, (2018).
- 8 Kim, J. *et al.* Biological Nicotinamide Cofactor as a Redox-Active Motif for Reversible Electrochemical Energy Storage. *Angew. Chem. Int. Ed.* **58**, 16764-16769, (2019).
- 9 Lee, S. *et al.* Recent Progress in Organic Electrodes for Li and Na Rechargeable Batteries. *Adv. Mater.* **30**, 1704682, (2018).
- 10 Song, Z. & Zhou, H. Towards sustainable and versatile energy storage

- devices: an overview of organic electrode materials. *Energy Environ. Sci.* **6**, 2280-2301, (2013).
- 11 Armand, M. *et al.* Conjugated dicarboxylate anodes for Li-ion batteries. *Nat. Mater.* **8**, 120-125, (2009).
- 12 Lee, M. *et al.* Multi-electron redox phenazine for ready-to-charge organic batteries. *Green Chem.* **19**, 2980-2985, (2017).
- 13 Placke, T. *et al.* Perspective on Performance, Cost, and Technical Challenges for Practical Dual-Ion Batteries. *Joule* **2**, 2528-2550, (2018).
- 14 Sui, Y. *et al.* Dual-ion batteries: The emerging alternative rechargeable batteries. *Energy Storage Mater.* **25**, 1-32, (2020).
- 15 Wang, M. & Tang, Y. A Review on the Features and Progress of Dual-Ion Batteries. *Adv. Energy Mater.* **8**, 1703320, (2018).
- 16 Zhang, L., Dou, S. X., Liu, H. K., Huang, Y. & Hu, X. Symmetric Electrodes for Electrochemical Energy-Storage Devices. *Adv. Sci.* **3**, 1600115, (2016).
- 17 Guo, S. *et al.* High-performance symmetric sodium-ion batteries using a new, bipolar O3-type material, Na_{0.8}Ni_{0.4}Ti_{0.6}O₂. *Energy Environ. Sci.* **8**, 1237-1244, (2015).
- 18 Wang, Y., Zeng, J., Cui, X., Zhang, L. & Zheng, G. Separator-Integrated, Reversely Connectable Symmetric Lithium-Ion Battery. *Small* **12**, 1091-1097, (2016).
- 19 Gao, H. & Goodenough, J. B. An Aqueous Symmetric Sodium-Ion Battery

- with NASICON-Structured Na₃MnTi(PO₄)₃. *Angew. Chem. Int. Ed.* **55**, 12768-12772, (2016).
- 20 Chen, H. *et al.* Lithium Salt of Tetrahydroxybenzoquinone: Toward the Development of a Sustainable Li-Ion Battery. *J. Am. Chem. Soc.* **131**, 8984-8988, (2009).
- 21 Wang, S. *et al.* All Organic Sodium-Ion Batteries with Na₄C₈H₂O₆. *Angew. Chem. Int. Ed.* **53**, 5892-5896, (2014).
- 22 Zhao, Q. *et al.* Oxocarbon Salts for Fast Rechargeable Batteries. *Angew. Chem. Int. Ed.* **55**, 12528-12532, (2016).
- 23 Chi, X. *et al.* Tailored Organic Electrode Material Compatible with Sulfide Electrolyte for Stable All-Solid-State Sodium Batteries. *Angew. Chem. Int. Ed.* **57**, 2630-2634, (2018).
- 24 Wang, S. *et al.* Organic Li₄C₈H₂O₆ Nanosheets for Lithium-Ion Batteries. *Nano Lett.* **13**, 4404-4409, (2013).
- 25 Dai, G. *et al.* A Dual-Ion Organic Symmetric Battery Constructed from Phenazine-Based Artificial Bipolar Molecules. *Angew. Chem. Int. Ed.* **131**, 10007-10011, (2019).
- 26 Nafe, J. *et al.* Functionalization of Quinoxalines by Using TMP Bases: Preparation of Tetracyclic Heterocycles with High Photoluminescence Quantum Yields. *Chem. Eur. J.* **21**, 1102-1107, (2015).
- 27 Sheldrick, G. M. SHELXT—Integrated space-group and crystal-structure determination. *Acta Crystallogr. A* **71**, 3-8, (2015).

- 28 Sheldrick, G. M. Crystal structure refinement with SHELXL. *Acta Crystallogr. C* **71**, 3-8, (2015).
- 29 Dolomanov, O. V., Bourhis, L. J., Gildea, R. J., Howard, J. A. & Puschmann, H. OLEX2: a complete structure solution, refinement and analysis program. *J. Appl. Crystallogr.* **42**, 339-341, (2009).
- 30 Gaussian 09, Revision D. 01 (2009).
- 31 Lee, C., Yang, W. & Parr, R. G. Development of the Colle-Salvetti correlation-energy formula into a functional of the electron density. *Phys. Rev. B* **37**, 785-789, (1988).
- 32 Stephens, P. J., Devlin, F. J., Chabalowski, C. F. & Frisch, M. J. Ab initio calculation of vibrational absorption and circular dichroism spectra using density functional force fields. *J. Phys. Chem.* **98**, 11623-11627, (1994).
- 33 Becke, A. Density-functional thermochemistry. III. The role of exact exchange. *J. Chem. Phys.* **98**, 5648-5652, (1993).
- 34 Schäfer, A., Horn, H. & Ahlrichs, R. Fully optimized contracted Gaussian basis sets for atoms Li to Kr. *J. Chem. Phys.* **97**, 2571-2577, (1992).
- 35 Schäfer, A., Huber, C. & Ahlrichs, R. Fully optimized contracted Gaussian basis sets of triple zeta valence quality for atoms Li to Kr. *J. Chem. Phys.* **100**, 5829-5835, (1994).
- 36 Klaumünzer, B., Kröner, D. & Saalfrank, P. (TD-)DFT Calculation of Vibrational and Vibronic Spectra of Riboflavin in Solution. *J. Phys. Chem. B* **114**, 10826-10834, (2010).

- 37 Trasatti, S. The absolute electrode potential: an explanatory note. *Pure Appl. Chem.* **58**, 955-966, (1986).
- 38 Peljo, P. & Girault, H. H. Electrochemical potential window of battery electrolytes: the HOMO–LUMO misconception. *Energy Environ. Sci.* **11**, 2306-2309, (2018).
- 39 Nikiforidis, G., van de Sanden, M. C. M. & Tsampas, M. N. High and intermediate temperature sodium–sulfur batteries for energy storage: development, challenges and perspectives. *RSC Adv.* **9**, 5649-5673, (2019).
- 40 Winsberg, J. *et al.* TEMPO/Phenazine Combi-Molecule: A Redox-Active Material for Symmetric Aqueous Redox-Flow Batteries. *ACS Energy Lett.* **1**, 976-980, (2016).
- 41 Nishida, S., Yamamoto, Y., Takui, T. & Morita, Y. Organic Rechargeable Batteries with Tailored Voltage and Cycle Performance. *ChemSusChem* **6**, 794-797, (2013).
- 42 Vadehra, G. S., Maloney, R. P., Garcia-Garibay, M. A. & Dunn, B. Naphthalene Diimide Based Materials with Adjustable Redox Potentials: Evaluation for Organic Lithium-Ion Batteries. *Chem. Mater.* **26**, 7151-7157, (2014).
- 43 Tian, B. *et al.* Amino group enhanced phenazine derivatives as electrode materials for lithium storage. *Chem. Commun.* **53**, 2914-2917, (2017).
- 44 Speer, M. E. *et al.* Thianthrene-functionalized polynorbornenes as high-voltage materials for organic cathode-based dual-ion batteries. *Chem.*

- Commun.* **51**, 15261-15264, (2015).
- 45 Liang, Y., Zhang, P., Yang, S., Tao, Z. & Chen, J. Fused Heteroaromatic Organic Compounds for High-Power Electrodes of Rechargeable Lithium Batteries. *Adv. Energy Mater.* **3**, 600-605, (2013).
- 46 Lim, H.-D. *et al.* Rational design of redox mediators for advanced Li–O₂ batteries. *Nat. Energy* **1**, 16066, (2016).
- 47 Zhang, F. *et al.* Tailoring the Voltage Gap of Organic Battery Materials Based on a Multi-Electron Redox Chemistry. *ChemElectroChem* **7**, 1781-1788, (2020).
- 48 Li, G., Chang, W.-H. & Yang, Y. Low-bandgap conjugated polymers enabling solution-processable tandem solar cells. *Nat. Rev. Mater.* **2**, 17043, (2017).
- 49 Yokoji, T. *et al.* Steric Effects on the Cyclability of Benzoquinone-type Organic Cathode Active Materials for Rechargeable Batteries. *Chem. Lett.* **44**, 1726-1728, (2015).
- 50 Lee, S. *et al.* Charge-transfer complexes for high-power organic rechargeable batteries. *Energy Storage Mater.* **20**, 462-469, (2019).
- 51 Xie, J. *et al.* Synthesis and Exploration of Ladder-Structured Large Aromatic Dianhydrides as Organic Cathodes for Rechargeable Lithium-Ion Batteries. *Chem. Asian J.* **12**, 868-876, (2017).
- 52 Peng, C. *et al.* Reversible multi-electron redox chemistry of π -conjugated N-containing heteroaromatic molecule-based organic cathodes. *Nat.*

- Energy* **2**, 17074, (2017).
- 53 Sun, T. *et al.* A phenazine anode for high-performance aqueous rechargeable batteries in a wide temperature range. *Nano Res.* **13**, 676-683, (2020).
- 54 Lee, M. *et al.* Redox Cofactor from Biological Energy Transduction as Molecularly Tunable Energy-Storage Compound. *Angew. Chem. Int. Ed.* **52**, 8322-8328, (2013).
- 55 Kolek, M. *et al.* Mechanism of Charge/Discharge of Poly(vinylphenothiazine)-Based Li–Organic Batteries. *Chem. Mater.* **30**, 6307-6317, (2018).
- 56 Peintinger, M. F., Beck, J. & Bredow, T. Charged stacks of dithiin, diselenin, thianthrene and selenanthrene radical cations: long range multicenter bonds. *Phys. Chem. Chem. Phys.* **15**, 18702-18709, (2013).
- 57 Jouhara, A. *et al.* Tuning the Chemistry of Organonitrogen Compounds for Promoting All-Organic Anionic Rechargeable Batteries. *Angew. Chem. Int. Ed.* **58**, 15680-15684, (2019).
- 58 Chen, Y., Zhang, Y.-H. & Zhao, L.-J. ATR-FTIR spectroscopic studies on aqueous LiClO₄, NaClO₄, and Mg(ClO₄)₂ solutions. *Phys. Chem. Chem. Phys.* **6**, 537-542, (2004).
- 59 Liu, H. *et al.* Capturing metastable structures during high-rate cycling of LiFePO₄ nanoparticle electrodes. *Science* **344**, 1252817, (2014).

- 60 Kim, J. H., Lindeman, S. V. & Kochi, J. K. Charge-Transfer Forces in the Self-Assembly of Heteromolecular Reactive Solids: Successful Design of Unique (Single-Crystal-to-Single-Crystal) Diels–Alder Cycloadditions. *J. Am. Chem. Soc.* **123**, 4951-4959, (2001).
- 61 Chen, J.-J. *et al.* Design and Performance of Rechargeable Sodium Ion Batteries, and Symmetrical Li-Ion Batteries with Supercapacitor-Like Power Density Based upon Polyoxovanadates. *Adv. Energy Mater.* **8**, 1701021, (2018).
- 62 Inoishi, A., Nishio, A., Yoshioka, Y., Kitajou, A. & Okada, S. A single-phase all-solid-state lithium battery based on $\text{Li}_{1.5}\text{Cr}_{0.5}\text{Ti}_{1.5}(\text{PO}_4)_3$ for high rate capability and low temperature operation. *Chem. Commun.* **54**, 3178-3181, (2018).
- 63 Zhang, Y., Zhao, H. & Du, Y. Symmetric full cells assembled by using self-supporting $\text{Na}_3\text{V}_2(\text{PO}_4)_3$ bipolar electrodes for superior sodium energy storage. *J. Mater. Chem. A* **4**, 7155-7159, (2016).
- 64 Li, M. *et al.* A high rate capability and long lifespan symmetric sodium-ion battery system based on a bipolar material $\text{Na}_2\text{LiV}_2(\text{PO}_4)_3/\text{C}$. *J. Mater. Chem. A* **6**, 9962-9970, (2018).
- 65 Wang, Y., Xiao, R., Hu, Y.-S., Avdeev, M. & Chen, L. $\text{P}_2\text{-Na}_{0.6}[\text{Cr}_{0.6}\text{Ti}_{0.4}]\text{O}_2$ cation-disordered electrode for high-rate symmetric rechargeable sodium-ion batteries. *Nat. Commun.* **6**, 6954, (2015).
- 66 Wang, D. *et al.* Sodium vanadium titanium phosphate electrode for

- symmetric sodium-ion batteries with high power and long lifespan. *Nat. Commun.* **8**, 15888, (2017).
- 67 Wang, H., Chen, C., Qian, C., Liang, C. & Lin, Z. Symmetric sodium-ion batteries based on the phosphate material of NASICON-structured $\text{Na}_3\text{Co}_{0.5}\text{Mn}_{0.5}\text{Ti}(\text{PO}_4)_3$. *RSC Adv.* **7**, 33273-33277, (2017).
- 68 Yao, Y. *et al.* Assembly of $\text{Na}_3\text{V}_2(\text{PO}_4)_2\text{F}_3@C$ nanoparticles in reduced graphene oxide enabling superior Na^+ storage for symmetric sodium batteries. *RSC Adv.* **8**, 2958-2962, (2018).
- 69 Wu, F. *et al.* Highly Safe Ionic Liquid Electrolytes for Sodium-Ion Battery: Wide Electrochemical Window and Good Thermal Stability. *ACS Appl. Mater. Interfaces* **8**, 21381-21386, (2016).

Chapter 4. Investigation on fundamentals of p-type reaction for developing high voltage organic batteries

4.1 Research background

As the cost of raw materials for conventional lithium layer oxides such as nickel and cobalt has soared as well as the conventional technology reaches fundamental limits, price-stable and sustainable rechargeable battery systems have been highlighted as possible next-generation energy storage solutions^{1,2}. Among various candidates, rechargeable organic batteries have garnered substantial interest due to their utilization of transition-metal-free organic materials composed of earth-abundant elements including carbon, hydrogen, oxygen, nitrogen, and sulfur. Organic materials are not only economically preferable but also environmentally desirable because they emit far fewer greenhouse gases than inorganic materials during the production and recycling process, and even they can be derived from biomass or are biodegradable³⁻⁶. However, the development of organic cathode materials was overshadowed by transition-metal-based materials because of significantly lower working potential of most reported *n*-type materials. To develop redox-active organics that rival inorganic electrode materials in terms of energy density, many research groups have focused on *p*-type organic materials, which possess a high operating voltage (about 3.5 V vs. Li⁺/Li) upon a reversible oxidation reaction⁷⁻¹¹. Unlike transition-metal oxides, most reported *p*-type materials do not contain lithium ions in their pristine state, hence, anions in the

electrolyte are reversibly involved during the oxidation to compensate for the positively charged *p*-type materials. The electrochemical responses of the *p*-type material are substantially affected by the type of anions in the electrolyte because the anions used are not single atomic ions but have significant sizes with diverse shapes. Numerous reports have shown that the reaction pathway, operating voltage, and cycle stability can vary depending on the size and shape of the anion¹⁰⁻¹⁴. However, previously reported electrochemical properties according to anion are inconsistent and vary for each *p*-type material, and there is no explanation for these erratic outcomes. This is owing to a dearth of fundamental understanding regarding the process of *p*-type redox reaction and the function of anions in reactions.

So far, the mechanistic understanding of *p*-type organic compounds has mostly relied on the spectroscopic analysis generally employed in organic chemistry. Quantitative investigations such as X-ray photoelectron spectroscopy (XPS), Fourier transform infrared spectroscopy (FTIR), and electron energy loss spectroscopy (EELS) analyses for the charged and discharged electrodes have proved that anions in the electrolyte are reversibly entailed during the *p*-type redox reaction¹⁰⁻¹². However, most of these analyses rely on ex situ investigations, thus, the procedural and structural understanding of how a bulky anion can participate in the reaction has been completely overlooked. Moreover, due to the difficulty of obtaining high-quality single crystals for the determination of unknown crystal structures and the presence of several polymorphs^{12,15,16}, crystallographic studies during the operation of organic batteries was challenge. Nevertheless, as the crystal

structure of organic materials greatly affects the electrochemical properties of the organic electrode^{17,18}, the fundamental understanding of the electrochemical reaction mechanism of the solid *p*-type organic battery system is essential to strategically design and develop a best-performing *p*-type organic cathode material.

In this article, we scrutinize the reaction mechanism of a representative *p*-type organic material, 5,10-Dihydro-5,10-dimethyl phenazine (DMPZ), using a combination of the in situ observation on both crystallographic and morphologic analysis. Through the multiscale in situ analysis demonstrating the crystallographic transformation at the atomic scale and associated morphological changes at the micro-scale, we propose a unique redox reaction process distinct from the typical insertion mechanism of lithium-ion batteries. In situ X-ray diffraction (XRD) analysis demonstrates that the DMPZ electrode undergoes a two-phase reaction in which the portion of two distinct phases in the system varies depending on the state of charge (SOC). Accordingly, the crystallographic information of the DMPZ and its charged phase are obtained using the single crystal X-ray diffraction (SC-XRD) analysis. Two structures display entirely different molecular arrangements, indicating that the DMPZ electrode does not follow the typical two-phase reaction in which guest ions are inserted through the framework while preserving the crystal structure, as LiFePO_4 and $\text{Li}_4\text{Ti}_5\text{O}_{12}$ electrodes do¹⁹⁻²². To directly identify the reaction process accompanying such abrupt change, we devised a system that enables real-time monitoring of the redox reaction of DMPZ using an optical microscope. This optical observation reveals that the charged phase of DMPZ

evolves on the surface of the DMPZ particle through electrolytic dissolution followed by recrystallization, not through the insertion of anions into the DMPZ mother structure. It was also confirmed that the dissolved intermediate state is the key enabler of this reorganization of organic crystal upon the reversible reaction. This study reveals, for the first time, the reaction mechanism of *p*-type organic electrodes, especially in the structural aspect, as well as the role of anions, and offers insight into the strategic design of *p*-type organic batteries for the development of sustainable rechargeable batteries that replace conventional cathode materials.

4.2 Experimental Methods

4.2.1 Preparation and characterization of materials

: 5,10-Dihydro-5,10-dimethylphenazine (DMPZ, > 99%) was purchased from Tokyo Chemical Industry. Silver perchlorate (AgClO_4 , anhydrous) and Zn foil (0.25 mm thick, 99.98%) were purchased from Alfa Aesar. Zinc perchlorate hexahydrate ($\text{Zn}(\text{ClO}_4)_2 \cdot 6\text{H}_2\text{O}$), deionized water (H_2O), acetonitrile (MeCN, anhydrous, 99.8%) tetrahydrofuran, pentane, and diethyl ether were purchased from Sigma Aldrich.

Synthesis of 5,10-dihydro-5,10-dimethylphenaziniumyl perchlorate ($[\text{DMPZ}^+][\text{ClO}_4^-]$): Each of DMPZ (100 mg, 0.48 mmol) and AgClO_4 (98.60 mg, 0.48 mmol) was dissolved in anhydrous acetonitrile (30 mL). Two solution was mixed, which immediately turned dark green. The solution was stirred overnight. The precipitate was filtered, then dissolved in acetonitrile and re-precipitated with an addition of diethyl ether. The final precipitate was dried under room temperature vacuum to yield $[\text{DMPZ}^+][\text{ClO}_4^-]$ as a dark green solid.

4.2.2 Electrochemical measurements

The organic electrodes were fabricated by mixing 50 wt% redox-active organic materials, 35 wt% carbon black (Super P), and 15 wt% polytetrafluoroethylene binder (Sigma Aldrich). A polypropylene membrane (Celgard 3501) was used as an electrolyte and Zn foil (0.25 mm thickness) was

used as counter electrode. The electrolyte was prepared by 1 molarity (the number of moles of salt per total liters of solvent, denoted by M) of concentration marked by the abbreviation 1 M $\text{Zn}(\text{ClO}_4)_2$ in H_2O . For the cycle stability test, the 17 M $\text{Na}(\text{ClO}_4)_2 + 0.5 \text{ M } \text{Zn}(\text{ClO}_4)_2$ in H_2O electrolyte was used. The cell was assembled into a coin cell (CR2032, Hohsen). The galvanostatic process was conducted using a potentiogalvanostat (WBCS-3000, Wonatech, Korea) at 25 °C. DMPZ electrode was cycled in the voltage range of 1.3 – 0.5 V vs. Zn^{2+}/Zn .

4.2.3 In situ X-ray diffraction

In-situ X-ray diffraction experiments were conducted at room temperature using coin-cell type home-made cells with an xx mm diameter hole in its center. To maximize diffraction signal, thin Zn foil with 0.05 mm thickness was used. For electrochemical cycling, the current density was 10 mA g^{-1} with potential range of 1.3 – 0.5 V (vs. Zn^{2+}/Zn). During the cycling process, X-ray diffraction patterns were collected every 5 minutes using R-Axis IV (RIGAKU, Japan) with Cu $\text{K}\alpha$ radiation ($\lambda = 1.5406 \text{ \AA}$)

4.2.4 In situ optical microscope

A home-made cell was prepared to monitor the electrochemical reaction of DMPZ. The DMPZ crystal is placed on the carbon film, which enabled the DMPZ to electrically contact and be observed in real time during the electrochemical reaction. The Zn foil is positioned slightly away from the carbon

film, and each of carbon tape and Zn foil is connected to SUS mesh, which enabled to connect with electrochemical test system. The DMPZ crystal and Zn foil is immersed in the electrolyte and home-made cell is completely sealed. The optical microscope (ECLIPSE LV150N, Nikon, Japan) and the cell were placed in an Ar glove box.

4.2.5 Characterizations

The electrodes at the different states of charge were disassembled from coin cells and were rinsed with H₂O to remove the remaining salts. SEM observation was performed with a SIGMA Field-Emission Scanning Electron Microscope (Carl Zeiss, United Kingdom) with Pt coating. Electrochemical impedance spectroscopy (Model VSP-300, Bio-Logic Science Instruments, France) was performed with a pressurized cell and measured from 1 Hz to 1 MHz with an amplitude of 10 mV. UV-vis spectroscopy analysis was performed using V-770 (JASCO, Japan) with an optical glass cuvette (Quartz; Hellma). For the rotating ring disk electrode test, rotating disk and ring electrode with glassy carbon (PINE research), Ag/AgCl reference electrode (Qrins, Korea), Pt wire, and bi-potentiostat (Biologics, VSP-300) was employed. For the XRD measurement of various electrodes, a D2 Phaser (Bruker, Germany) with Cu K α radiation ($\lambda = 1.5406 \text{ \AA}$) was used.

4.3 Results and discussion

4.3.1 Building system for the mechanism study

The number of reported *p*-type redox-active organic motifs is significantly lower than *n*-type motifs since the research history of *p*-type materials is much shorter than *n*-type materials^{4,23,24}. The reported *p*-type motifs so far include dihydrohenazine derivatives^{10,25-27}, phenothiazine derivatives^{8,9}, phenoxazine derivatives^{8,11,28}, thiazine derivatives^{29,30} and 2,5-(dianilino)terephthalate¹². All of these compounds undergo reversible anion-participating oxidation reactions and exhibit a high operating voltage of 3.1-3.7 V vs. Li⁺/Li. In this study, we selected 5,10-dihydro-5,10-dimethylphenazine (DMPZ) to disclose the redox mechanism of *p*-type redox-active organic materials. DMPZ is a representative *p*-type material that has been assured of compatibility with diverse anions and of electrochemical stability to the extent that its redox activity is utilized in a variety of energy storage systems. As presented in Figure 4.1a, diazabutadien motif in heterocyclic system of DMPZ acts as a redox center exhibiting a theoretical capacity of 127 mAh g⁻¹. The DMPZ electrode was fabricated and operated in aqueous electrolyte to deter the troublesome dissolution problem which leads to the capacity loss and cycle degradation in organic battery systems. DMPZ is known to well dissolve in organic solvents as utilized as catholyte for non-aqueous flow batteries, which could be confirmed through the absorbance peak in UV-vis spectrum when we dissolved DMPZ in dichloromethane (DCM) and acetonitrile (MeCN) as presented in Figure 4.2a. However, DMPZ is completely insoluble in the aqueous electrolyte as shown

in Figure 4.1b. Even when UV-vis absorption was measured after immersion of DMPZ in the aqueous electrolyte followed by ultrasonication, the absorption peak corresponding to DMPZ was observed, demonstrating the insolubility of DMPZ. The peaks observed in the aqueous solvent containing DMPZ are attributed to the absorbance of charged DMPZ (Figure 4.2b), which is generated by the autooxidation of DMPZ³¹. Fig. 4.1c presents the charge/discharge profile of DMPZ in our system which shows explicit voltage plateaus at an average potential of 0.95 V (vs. Zn²⁺/Zn) and specific capacities of 107 mA g⁻¹ and 100 mAh g⁻¹ for initial charge and discharge, respectively.

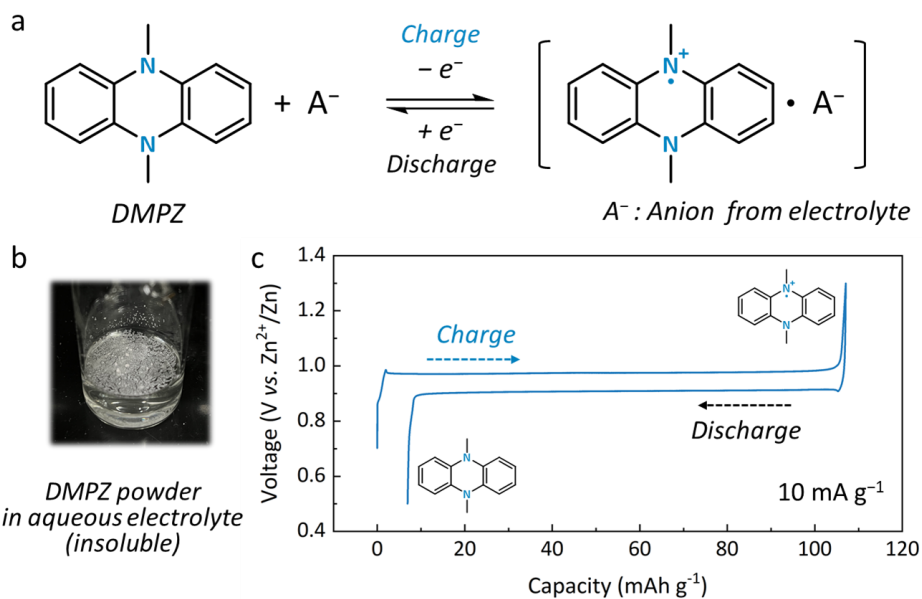


Figure 4.1. Electrochemical reaction of DMPZ in an aqueous system. a) Molecular structure and reaction formula of DMPZ. b) Photo image of DMPZ powder dispersed in aqueous electrolyte. c. Galvanostatic charge/discharge profile of DMPZ electrode in Zn cell at a current density of 10 mA g⁻¹.

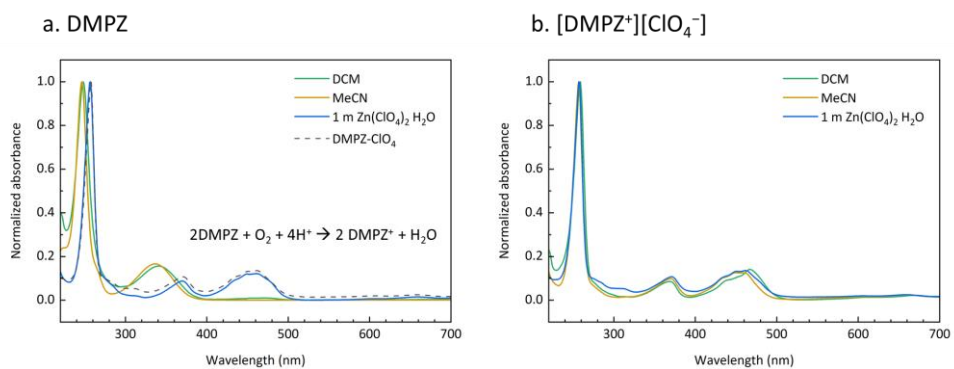


Figure 4.2. Normalized UV-vis absorption spectra of (a) DMPZ and (b) [DMPZ⁺][ClO₄⁻] in various aqueous and non-aqueous solvent

4.3.2 Crystallographic understanding during the *p*-type reaction

We first examined the structural evolution of the DMPZ electrode upon the reversible redox reaction using in situ XRD as presented in Figure 4.3a and Figure 4.4. Figure 4.4 shows overall XRD patterns ranging from 5° to 40° and the noticeable changes are summarized in Figure 4.3a. The characteristic peaks of the pristine electrode are represented by $2\theta = 11, 13.2, 20.2, 25.9,$ and 27.7° . Upon the charging which corresponds to the oxidation of the DMPZ electrode, the intensity of these peaks decreased while the new peaks at $2\theta = 19.4, 19.9,$ and 25° gradually evolved although some peaks at $2\theta = 15, 17.1, 22.3, 24.4$ slightly overlapped with the decreasing pristine peaks. This peak evolution occurred reversibly during the discharging process, and the peaks were restored to the identical state as the pristine peak after the discharge. These changes in peak patterns indicate that the DMPZ electrode undergoes a reversible two-phase electrochemical reaction, in which two different phases coexist upon the cycle, rather than the solid-solution reaction^{20,22}. This result is consistent with the conjecture deduced from the flat voltage plateau of the DMPZ electrode in Fig. 4.1c. Only two distinct organic phases exist during the charge and discharge varying their portion depending on the SOC, and it can be deduced that DMPZ and $[\text{DMPZ}^+][\text{ClO}_4^-]$ must be those two phases in our system.

To identify the crystal structure of DMPZ, SC-XRD analysis was conducted using the crystal grown by slow diffusion of antisolvent vapor into the DMPZ solution. The bottom panel in Figure 4.3b with beige color displays the

crystal structure of neutral DMPZ. Neutral DMPZ has a bent molecular structure with an interplanar angle of 144° along the two nitrogen atoms of the central heterocyclic ring. These six neutral DMPZ molecules are in a unit cell which is a hexagonal lattice system (space group P63/m) as presented in Figure 4.3b bottom image that is consistent with a previous report measured at 173 K ³². This structure is distinct from the other well-known anion-inserting materials such as graphite having a layered structure that facilitates the insertion of bulky anions. The calculated powder X-ray diffraction (PXRD) pattern based on the SC-XRD result (presented at the bottom of the DMPZ structure in Figure 4.3b) well matches the pattern of the pristine DMPZ electrode as displayed in Figure 4.5a, indicating that the DMPZ structure we exploited is identical to the structure determined by SC-XRD analysis.

For the first step in revealing the crystal structure of charged DMPZ, we chemically synthesized $[\text{DMPZ}^+][\text{ClO}_4^-]$ compound and obtained dark green powder. The PXRD pattern of the electrode made with chemically synthesized $[\text{DMPZ}^+][\text{ClO}_4^-]$ matched the peaks that were newly evolved upon the charging of the DMPZ electrode as assigned in Figure 4.3a and Figure 4.5b, implying that the electrochemically charged phase and the chemically synthesized compound are crystallographically identical. It is also supported by the overlapping charge/discharge profiles of the DMPZ electrode and the $[\text{DMPZ}^+][\text{ClO}_4^-]$ electrode, as shown in Figure 4.5c. Moreover, we successfully obtained the high-quality single crystal $[\text{DMPZ}^+][\text{ClO}_4^-]$ for SC-XRD analysis through the same

method used to obtain the DMPZ crystal. Figure 4.3b top panel presents the molecular structure of DMPZ⁺ and the crystal structure of [DMPZ⁺][ClO₄⁻]. It was confirmed that the calculated PXRD pattern matched the XRD patterns of the [DMPZ⁺][ClO₄⁻] electrode (Figure 4.5d). There are remarkable changes in crystal structure compared to pristine DMPZ. First, the DMPZ molecule turned out to be planar after oxidation. Along with the conformational transition, there are drastic changes in the crystallographical arrangement. While neutral DMPZ crystal has a structure in which three DMPZ molecules face each other, [DMPZ⁺][ClO₄⁻] belongs to the monoclinic system (space group C2/c) in which obliquely arranged DMPZ⁺ molecules are stacked in a zigzag manner with perchlorate anions positioned between them as demonstrated by SC-XRD. Such crystallographic difference cannot be explained based on the classical two-phase reaction based on the topotactic mechanism in which the arrangement of the framework is maintained and the phase boundary moves by the guest ions insertion/deinsertion^{22,33,34}.

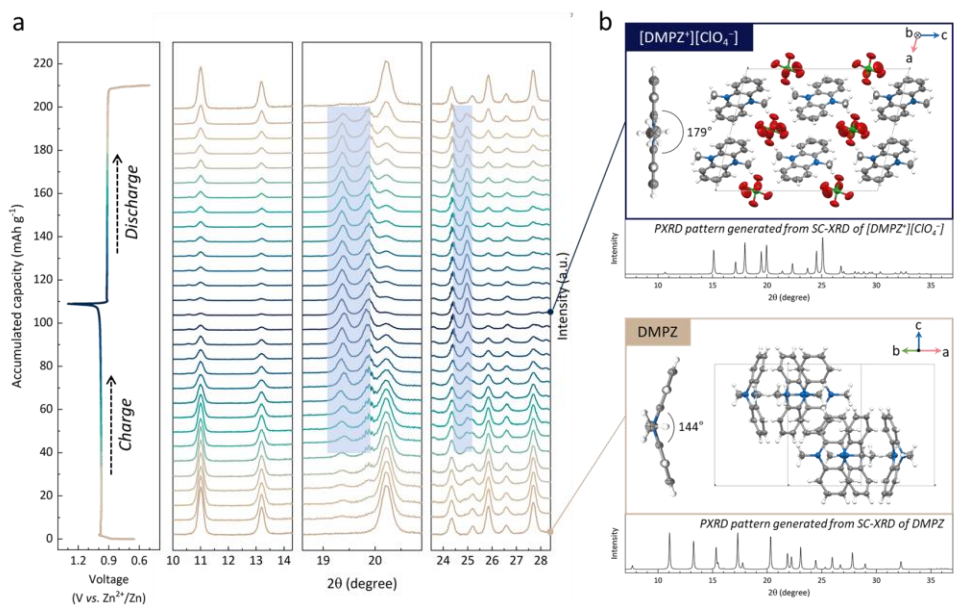


Figure 4.3. Structural evolution of DMPZ during charge/discharge process. a. Voltage profile of DMPZ electrodes cycled at 10 mA g⁻¹ and corresponding summarized in situ XRD patterns. The displayed patterns were collected every 45 minutes. The peaks in the blue box are new peaks that evolved upon charging. b. The molecular and crystal structure of DMPZ and [DMPZ⁺][ClO₄⁻] determined by SC-XRD at room temperature and corresponding PXRD patterns calculated from the SC-XRD result.

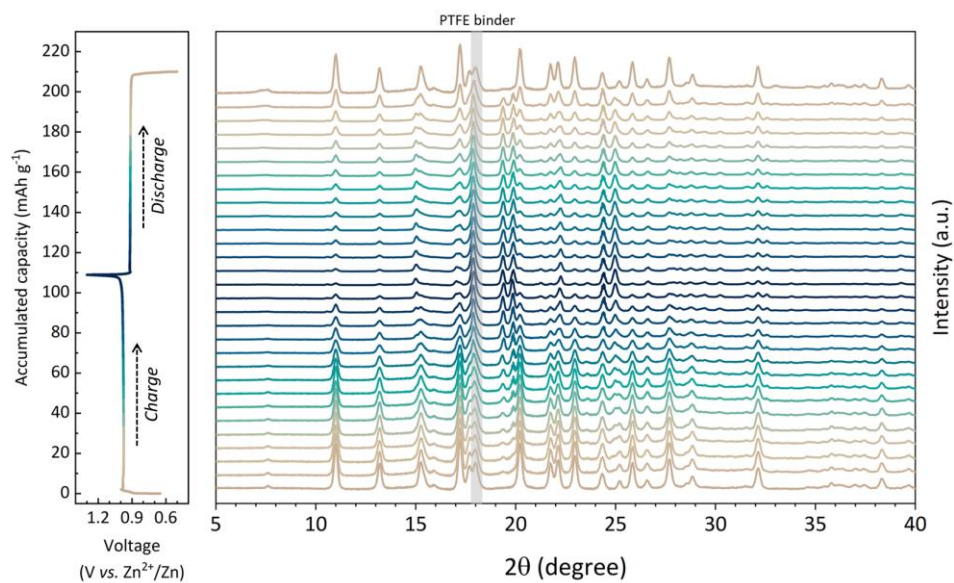


Figure 4.4. In situ XRD patterns of DMPZ electrodes cycled under a current rate of 10 mA g⁻¹ and corresponding voltage profile.

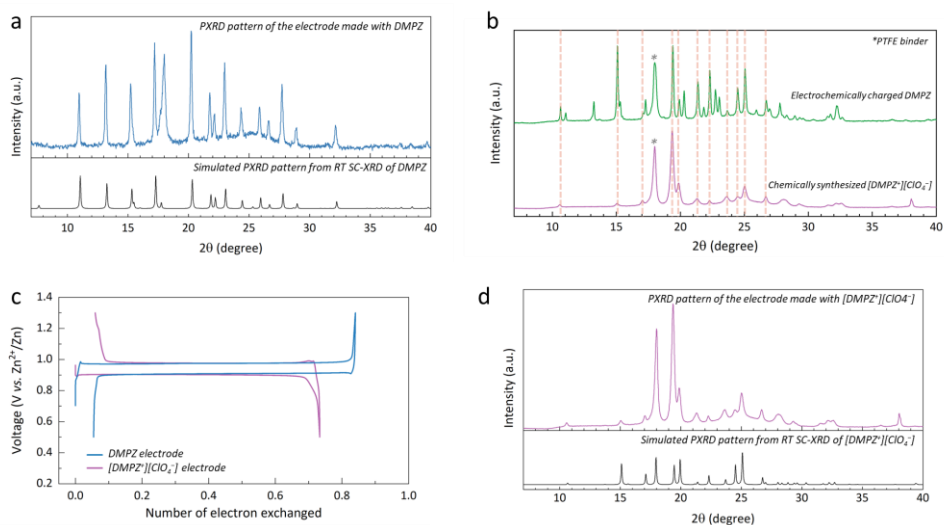


Figure 4.5. a. PXRD pattern of the DMPZ electrode (top) and simulated PXRD pattern based on SC-XRD result of DMPZ obtained at room temperature (bottom). b. PXRD pattern of the charged DMPZ electrode (top) and that of the electrode made with chemically synthesized $[\text{DMPZ}^+][\text{ClO}_4^-]$ (bottom). c. Normalized charge/discharge profile of DMPZ electrode (blue) and $[\text{DMPZ}^+][\text{ClO}_4^-]$ electrode (purple). d. PXRD pattern of the $[\text{DMPZ}^+][\text{ClO}_4^-]$ electrode (top) and simulated PXRD pattern based on SC-XRD result of $[\text{DMPZ}^+][\text{ClO}_4^-]$ obtained at room temperature (bottom).

4.3.3 Real-time monitoring of morphological evolution

Motivated by the unexpected revelation that the charged states of *p*-type materials have diametrically different crystal structures from the neutral ones, the real-time monitoring of the *p*-type reaction was performed using an optical microscope to observe the intermediate process of *p*-type reaction. Figure 4.6a illustrates the schematic of a homemade cell and microscope system that is capable of observing electrochemical reactions using DMPZ crystals under a microscope. The first image in Figure 3b shows a colorless neutral DMPZ crystal on an electrically conductive carbon tape. During the initial stage of galvanostatic charging, dark green nuclei are formed on the DMPZ crystal surface, which was proven to be $[\text{DMPZ}^+][\text{ClO}_4^-]$ by Raman spectroscopy as shown in Figure 4.7. Upon continued charging, as demonstrated in Figure 4.6b and Supplementary Video 1, surprisingly, we confirmed noticeable morphological changes from the surface. The dark green and frost-like crystalline phase gradually grows from the surface while the overall size of the colorless DMPZ particle gradually diminishes^{35,36}. The reaction takes place at the bottom contour side of the DMPZ crystal where all three of the DMPZ, electron, and anion can be supplied. This morphological evolution differs significantly from that observed in classical two-phase reactions in which the overall particle size and shape are preserved during ion insertion³⁷⁻³⁹. After deep charging of DMPZ as displayed in Figure 4.8, it was obviously observed that the overall contour of the particle was changed and the frost-like $[\text{DMPZ}^+][\text{ClO}_4^-]$ grows outward around the DMPZ crystal.

Since there is a disjunction in scale between the DMPZ crystal that was enlarged to hundreds of micro-scales for real-time observation and the DMPZ particles that undergo redox reaction in the realistic battery system in tens of micro-scale, we further probe the morphological changes using DMPZ particles with a size of tens of micrometers or less. The scanning electron microscope (SEM) image presented in Figure 4.9a shows the pristine DMPZ particles with a granular shape. The new phases have grown out on the surface at the beginning of the reaction as we marked in green in Figure 4.9b. Energy dispersive spectroscopy (EDS) confirmed that this newly grown phase is a DMPZ charged phases as exhibited in Figure 4.9d. This morphological evolution is consistent with that observed in the in situ optical monitoring. Subsequently, all the granular-shaped DMPZ turns to elongated and flattened morphology after continuous charging as presented in Figure 4.9c, which is analogous to that grown on the DMPZ crystal observed in the optical system.

Inspired by in situ and ex situ observation of morphological changes of DMPZ in modeled system, we attempted to explore the morphological change in realistic electrodes during the reaction by ex situ SEM characterization (Figure 4.6c-e and Figure 4.10). The pristine electrode as shown in Figure 4.6c consists of DMPZ particles with a size of about 5 μm which is marked as green color and conductive carbon particles with less than 200 nm. When charging begins, the $[\text{DMPZ}^+][\text{ClO}_4^-]$ nuclei are formed (Figure 4.10, 40 mAh g^{-1} charged electrode), and their size increases rapidly as charging proceeds. Finally, the flat

[DMPZ⁺][ClO₄⁻] phase is enlarged to unexpected hundreds of micrometer size and covers the surface of the electrode as shown in Figure 4.6d. Considering that the system in the coin cell is under vertical pressure, [DMPZ⁺][ClO₄⁻] is restricted to grow parallel to the surface, resulting in a horizontally stretched morphology analogous to that of plate-shaped materials having a preferred orientation under pressure⁴⁰. Once growing nuclei encounter adjacent nuclei, the phases overlap each other and evolve into large plate-shaped [DMPZ⁺][ClO₄⁻], as observed in Figure 4.6d. During re-discharging as presented in Figure 4.10, the [DMPZ⁺][ClO₄⁻] phase covering the surface gradually peels off and pores with a size of 1~5 μm were detected on the exposed electrode surface. It is assumed, based on their size, that the pores were originally filled with DMPZ particles. Neutral DMPZ particles appear near the remaining [DMPZ⁺][ClO₄⁻] phase in the half discharged electrode (Figure 4.11), and as discharging continued, the plate-like [DMPZ⁺][ClO₄⁻] phases vanished, leaving only granular DMPZ particles with the size of 2~10 μm (Figure 4.6e). One notable point is that the location of the DMPZ particles is changed after discharging compared to that of the pristine electrode, which can be deduced from the concurrent observation of pores and DMPZ particles at the discharged electrode. This morphological change behavior continued during subsequent cycles. (Figure 4.12). The observations of structural and morphological evolution using in situ and ex situ examination can be summarized as follows; i) the crystal structures of the pristine phase and the charged phase are completely different, ii) the *p*-type reaction does not proceed through an insertion reaction that the ions are inserted

into the stationary DMPZ framework, iii) but proceeds by the initial nucleation of charged phase followed by the growth of those nuclei, and iv) the DMPZ molecules are not held in place during the reaction, thereby large morphological change of particle is involved.

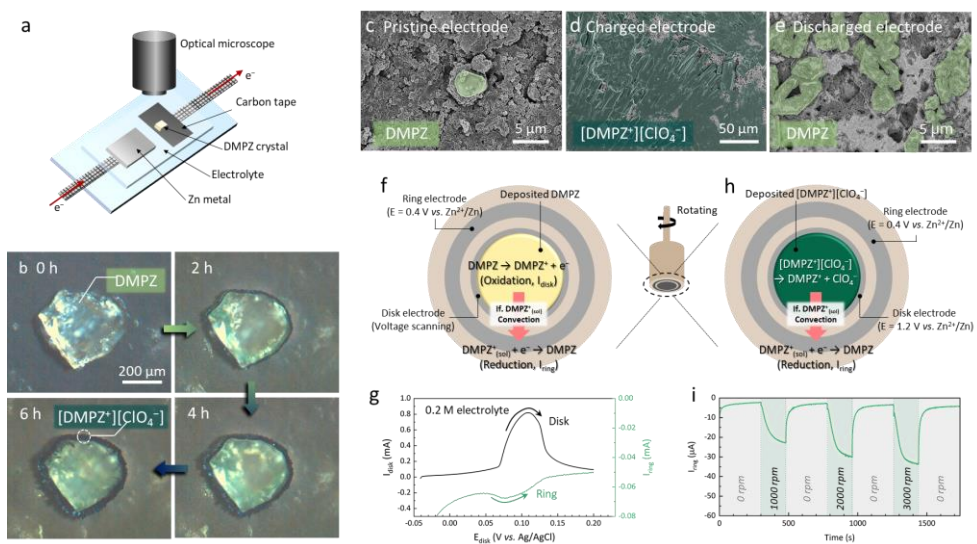


Figure 4.6. Morphological change of DMPZ during *p*-type reaction and the presence of solvated intermediate. a. Schematic illustration of the in situ optical system. b. In situ optical microscopy images of DMPZ crystal during the galvanostatic charging, which demonstrate the surface reorganization of DMPZ. c-f. Ex situ SEM images of the DMPZ electrode at different states of charge during the first cycle; pristine electrode (c), charged electrode (d), and discharged electrode (e). f. Schematic illustration of rotating ring disk electrode with DMPZ deposited to the disk electrode and related reaction occurring at each electrode. g. Current response obtained in the rotating ring disk electrode experiment presented in Figure 3e with 0.2 M $\text{Zn}(\text{ClO}_4)_2 \cdot \text{H}_2\text{O}$ electrolyte. The rotation rate of 1,000 rpm and a scan rate of 5 mV s^{-1} were used. h. Schematic illustration of rotating ring disk electrode with $[\text{DMPZ}^+][\text{ClO}_4^-]$ deposited to the disk electrode and related reaction occurring at each electrode. i. Current response from ring electrode obtained in the rotating

ring disk electrode experiment presented in Figure 4.6g with 0.2 M $\text{Zn}(\text{ClO}_4)_2 \cdot \text{H}_2\text{O}$ electrolyte. A pause for 5 minutes and a rotation for 3 minutes were repeated, and the rotation rpm was increased to 1000, 2000, and 3000 rpm.

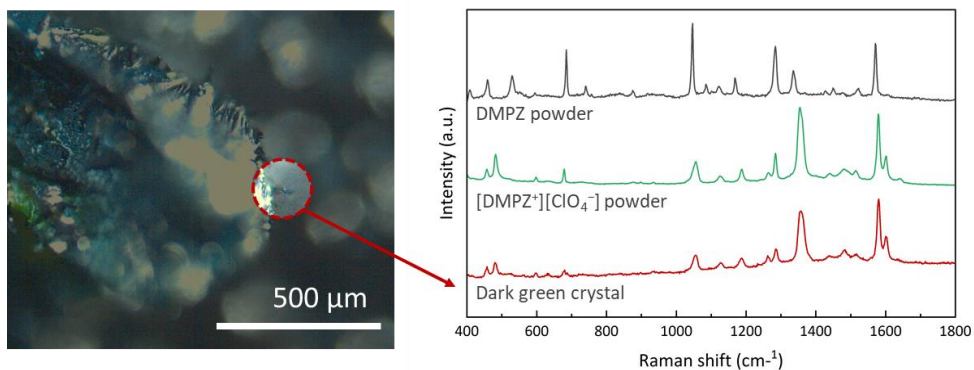


Figure 4.7. Raman spectra of DMPZ powder, $[\text{DMPZ}^+][\text{ClO}_4^-]$ powder and dark green phase grown on the crystalline DMPZ surface after charging in the homemade cell presented in Figure 3a with 1 M $\text{Zn}(\text{ClO}_4)_2 \cdot \text{H}_2\text{O}$ electrolyte. Raman spectra of the dark green phase is identical to that of the $[\text{DMPZ}^+][\text{ClO}_4^-]$ powder.

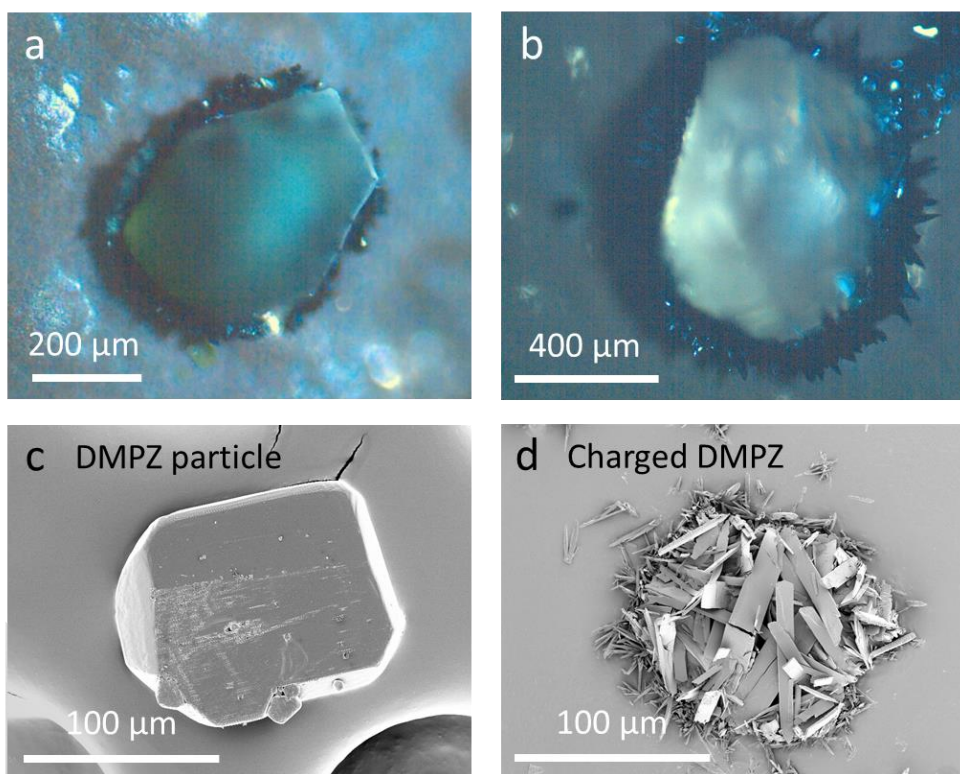


Figure 4.8. a,b. Optical microscope image of DMPZ crystal after deep charging ((a) for 24 hours and (b) for 15 hours) c. SEM images of DMPZ particle on the carbon tape with the size of hundred micrometers. d. SEM images of the charged DMPZ particle in 1 M Zn(ClO₄)₂ H₂O electrolyte.

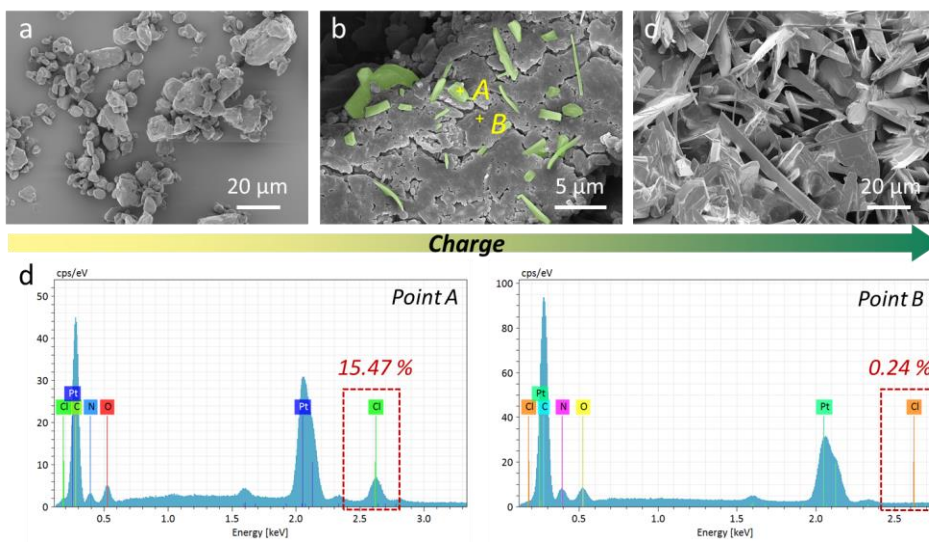


Figure 4.9. a. SEM image of DMPZ powder. b. Magnified SEM image of the DMPZ particle surface after 2 minutes of galvanostatic charging in 1 M Zn(ClO₄)₂ H₂O electrolyte. c. SEM image of DMPZ powder after 5 hours of galvanostatic charging in 1 M Zn(ClO₄)₂ H₂O electrolyte. d. EDS results in each point indicated in Figure S5b. EDS results demonstrate that the area marked in green color in Figure S6b is the charged DMPZ phase.

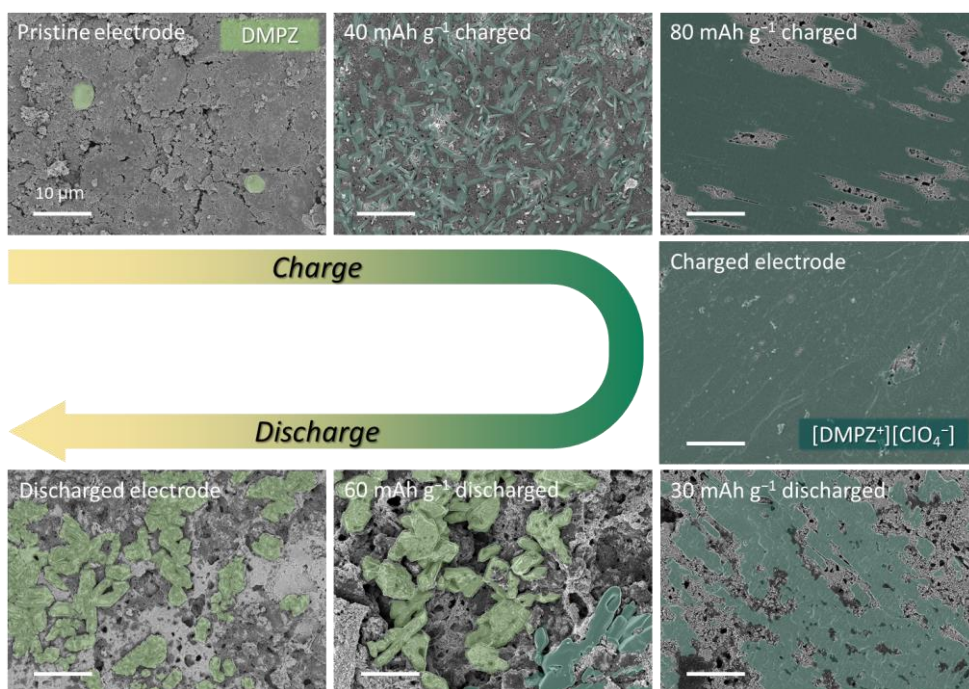


Figure 4.10. Ex situ SEM images of DMPZ electrode at different states of charge during the first cycle in 1 M $\text{Zn}(\text{ClO}_4)_2 \cdot \text{H}_2\text{O}$ electrolyte. Note that scale bars in each image represent different lengths. Light green colored particles indicate DMPZ and dark green colored particles indicate $[\text{DMPZ}^+][\text{ClO}_4^-]$

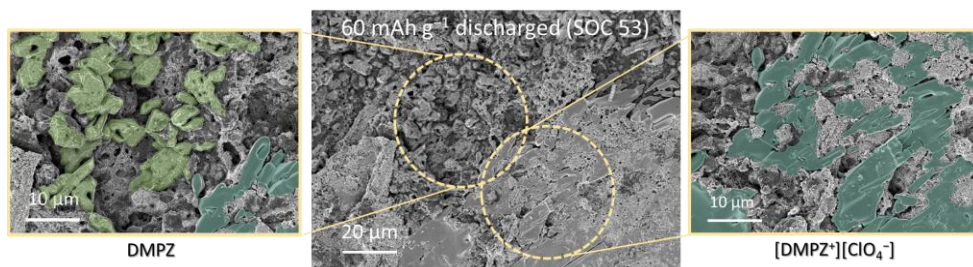


Figure 4.11. Magnified SEM image of half discharged electrode after charge to 1.3 V vs. Zn²⁺/Zn. DMPZ particles are located near the [DMPZ⁺][ClO₄⁻] that is peeling off during the discharge.

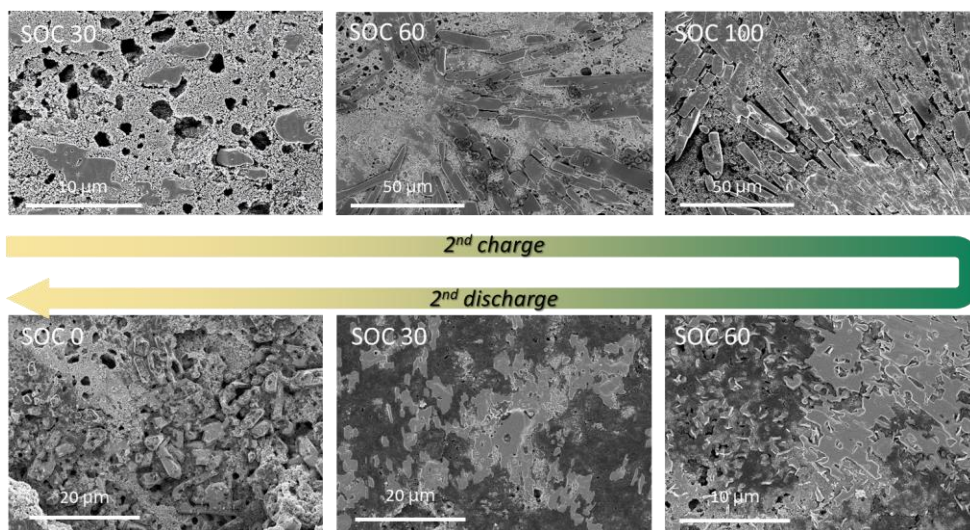


Figure 4.12. Ex situ SEM images of DMPZ electrode at different states of charge during the second cycle in 1 M $\text{Zn}(\text{ClO}_4)_2 \cdot \text{H}_2\text{O}$ electrolyte.

4.3.4 The presence of solvated intermediate phase

The reaction progress that we observed is closely akin to that of the lead-acid battery system. The lead-acid battery is one of the most mature rechargeable battery systems and has been used in a wide range of applications including transport vehicles, backup power supplies for telecommunication, and grid energy storage⁴¹⁻⁴³. The system, which consists of a lead (Pb) plate for an anode, a lead dioxide ($\text{Pb}^{(\text{IV})}\text{O}_2$) plate for a cathode, and a sulfuric acid solution for an electrolyte, is based on the reaction in which Pb and PbO_2 are oxidized and reduced to lead sulfate ($\text{Pb}^{(\text{II})}\text{SO}_4$), respectively. Similar to the case of the DMPZ and $[\text{DMPZ}^+][\text{ClO}_4^-]$, Pb and PbO_2 and their oxidized/reduced phase PbSO_4 have an entirely different crystallographic structure, which has a cubic ($\text{Fm}\bar{3}\text{m}$), tetragonal (β phase, $\text{P4}_2/\text{mmn}$), and orthorhombic (Pnma) structure respectively^{41,42,44}. Based on the prior knowledge of the reaction mechanism of lead-acid batteries, we are aware that such transformation into a completely different structure cannot occur through a direct solid-to-solid transition^{42,43,45}. Thus, we hypothesized that our observation is indicative of the presence of the intermediate phase that enables such phase transformation as in a lead-acid battery system, and we were able to demonstrate this supposition utilizing the rotating ring-disk electrode (RRDE) study. To identify the intermediate phase of the oxidation reaction, the DMPZ was deposited on the disk electrode and oxidized in 0.2 M $\text{Zn}(\text{ClO}_4)_2$ in H_2O electrolyte. Figure 4.6f is the schematics displaying the reaction occurring at the disk and ring

electrode. The disk potential was scanned with the rate of 5 mV s^{-1} and the ring potential was fixed at $-0.6 \text{ V vs. Ag/AgCl}$ ($0.4 \text{ V vs. Zn}^{2+}/\text{Zn}$) with a fast rotating speed of 1,000 rpm. DMPZ starts to be oxidized at the disk electrode with the increasing potential generating the disk current (I_{disk}). At this moment, if there is soluble $\text{DMPZ}^+_{(\text{sol})}$ intermediate state, it may drift out toward the ring disk due to the convection made by the fast electrode rotation and it is reduced in the ring electrode generating the ring current (I_{ring}). Figure 4.6g showed that a significant amount of reduction current was detected at the ring electrode simultaneously with the oxidation current from DMPZ in the disk electrode, validating the presence of solvated intermediate species, which is $\text{DMPZ}^+_{(\text{sol})}$. The ratio of oxidation charge to reduction charge was calculated at various rotation rate of the electrode. Since the intermediate species oxidized at the disk electrode drift out toward the ring and are lost, the total reduction charge from the disk electrode ($Q_{\text{disk, reduction}}$) would be less than the total oxidation charge from the disk electrode ($Q_{\text{disk, oxidation}}$) when the potential of the disk electrode is increased reversibly. It was confirmed that the $Q_{\text{disk,oxidation}}/Q_{\text{disk,reduction}}$ decreased as the rotation rate of the electrode increased as calculated in Figure 4.13d. This is because the more solvated intermediate phase is lost from the disk electrode as a result of the faster convection rate, and this variation supports the existence of soluble intermediate species. Given that, more than 90% of the oxidized species was reversibly reduced despite high convection rate of 3000 rpm, suggesting that the duration time for these solvated intermediates was short.

Meanwhile, when the RRDE test is performed in 1 M electrolyte keeping other experimental conditions same, we could not detect any ring current (Figure 4.14a-c). Even when the rotating rate was increased to 3,000 rpm for fast convection to carry the DMPZ^+ to the ring electrode, no ring current was detected and the $Q_{\text{disk,oxidation}}/Q_{\text{disk,reduction}}$ ratio was unaffected by the increase in rotation rate (Figure 4.14d). Considering the precipitation process of $\text{DMPZ}^+_{(\text{sol})} + \text{ClO}_4^-_{(\text{sol})} \rightarrow [\text{DMPZ}^+][\text{ClO}_4^-]$, solvated DMPZ^+ phase is immediately precipitated just after the oxidation before reaching to ring in the 1 M electrolyte due to higher ClO_4^- concentration, while it can be sustained until reaching the ring disk in the 0.2 M electrolyte. As calculated in Figure 4.15 using UV-vis absorption spectra, $[\text{DMPZ}^+][\text{ClO}_4^-]$ has extremely low solubility of 2.275 mM in water which corresponds to the solubility product constant of 5.176×10^{-6} . In 0.2 M and 1 M electrolyte systems, the solubility of $[\text{DMPZ}^+][\text{ClO}_4^-]$ is extremely low at 2.59 μM and 12.94 μM , respectively, validating the RRDE results that ring current could only be observed at low concentration electrolyte. Namely, the $\text{DMPZ}^+_{(\text{sol})}$ state only exists momentarily under the battery operating condition that uses 1 M electrolyte.

To identify the intermediate phase in the discharge process of $[\text{DMPZ}^+][\text{ClO}_4^-]$, RRDE test was conducted depositing $[\text{DMPZ}^+][\text{ClO}_4^-]$ on the disk electrode. As schematically illustrated in Figure 4.16a, the potential of disk electrode was scanned with the rate of 5 mV s^{-1} , while the ring potential was fixed at 0.3 V vs. Ag/AgCl (1.3 V vs. Zn^{2+}/Zn) to observe solvated DMPZ intermediates.

However, in this case, no oxidation current was measured at the ring electrode when $[\text{DMPZ}^+][\text{ClO}_4^-]$ is reduced at the disk electrode despite the fast rotation rate of 1000-3000 rpm. Moreover, unlike when DMPZ^+ intermediate was detected, the $Q_{\text{disk,oxidation}}/Q_{\text{disk,reduction}}$ ratio was maintained even when the rotation rate increased, demonstrating that there are no solvated DMPZ intermediate as depicted in Figure 4.16b-d

We hypothesized that the lattice reconstruction during the discharge reaction also go through the solvated $\text{DMPZ}^+_{(\text{sol})}$ intermediates. To demonstrate this hypothesis, we redesigned the RRDE experiment condition as depicted in Figure 4.6h. $[\text{DMPZ}^+][\text{ClO}_4^-]$ was deposited on the disk electrode, and the constant potential of 0.2 V vs. Ag/AgCl (1.2 V vs. Zn^{2+}/Zn) was applied, which did not activate any redox reaction. The potential of -0.6 V vs. Ag/AgCl (0.4 V vs. Zn^{2+}/Zn) was applied at the ring electrode so that it could be reduced if DMPZ^+ intermediate phase is approached. We monitored the ring current while intermittently rotating the electrode for 3 minutes and pausing it for 5 minutes (Figure 4.6i). As a result, the ring current was only detected when the electrode is rotating, and the current was increased as the rotation speed increased. It proves that the solvated DMPZ^+ intermediate can be reduced to DMPZ . Moreover, it can be found that $\text{DMPZ}^+_{(\text{sol})}$ is generated from $[\text{DMPZ}^+][\text{ClO}_4^-]$ without any redox reaction by the dissolution. $\text{DMPZ}^+_{(\text{sol})}$ phase can be continuously produced at the disk electrode on the basis of Le Chatelier's principle because $\text{DMPZ}^+_{(\text{sol})}$ moves out to the ring electrode, allowing for continuous reduction at the ring electrode.

This RRDE test reveals that the discharge reaction of $[\text{DMPZ}^+][\text{ClO}_4^-]$ also passed through the solvated DMPZ^+ intermediate state as in the charging process.

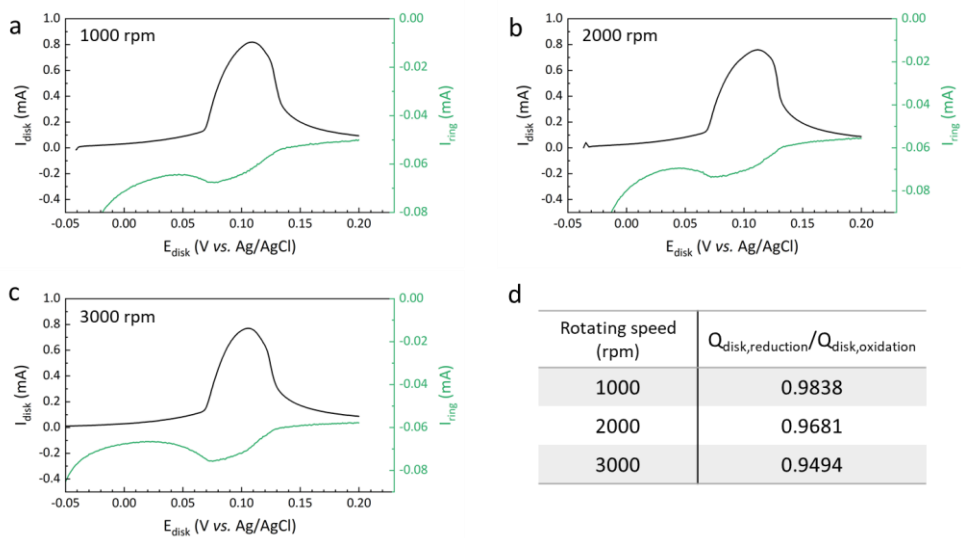


Figure 4.13. a-c. RRDE experiment results in 0.2 M $\text{Zn}(\text{ClO}_4)_2 \cdot \text{H}_2\text{O}$ electrolyte with various rotating rate. a. 1,000 rpm. b. 2,000 rpm. c. 3,000 rpm. d. The ratio of oxidation charge to reduction charge in each rotation rate. The oxidation and reduction charge was calculated by the integrating the positive and negative areas of the current-time curve of the linear sweep voltammetry of the disk electrode.

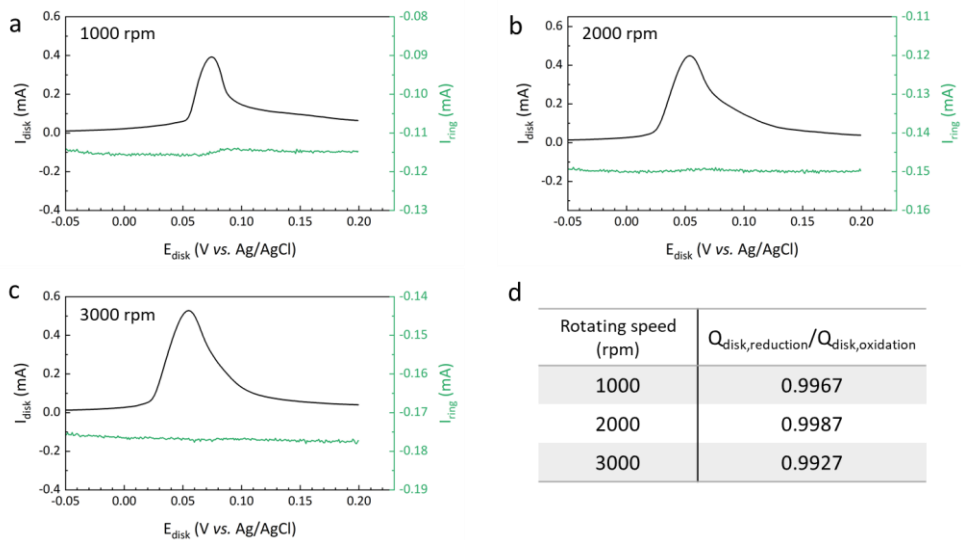
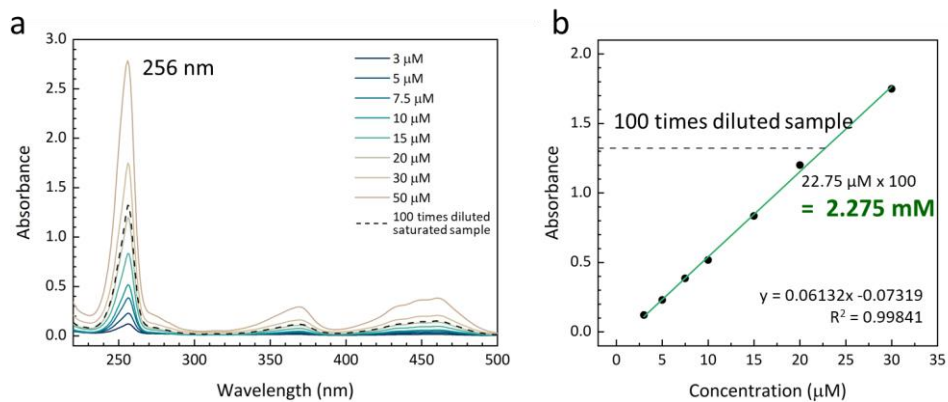


Figure 4.14. RRDE experiment results in 1 M $\text{Zn}(\text{ClO}_4)_2 \cdot \text{H}_2\text{O}$ electrolyte with various rotating rate. a. 1,000 rpm. b. 2,000 rpm. c. 3,000 rpm. d. The ratio of oxidation charge to reduction charge in each rotation rate.



Figures 4.15. a. UV-vis absorption spectra of [DMPZ⁺][ClO₄⁻] with various concentrations dissolved in water and b. corresponding Beer-Lambert calibration curve. Calculated solubility product (K_{sp}) based on the UV-vis absorption spectra is 5.176×10^{-6} .

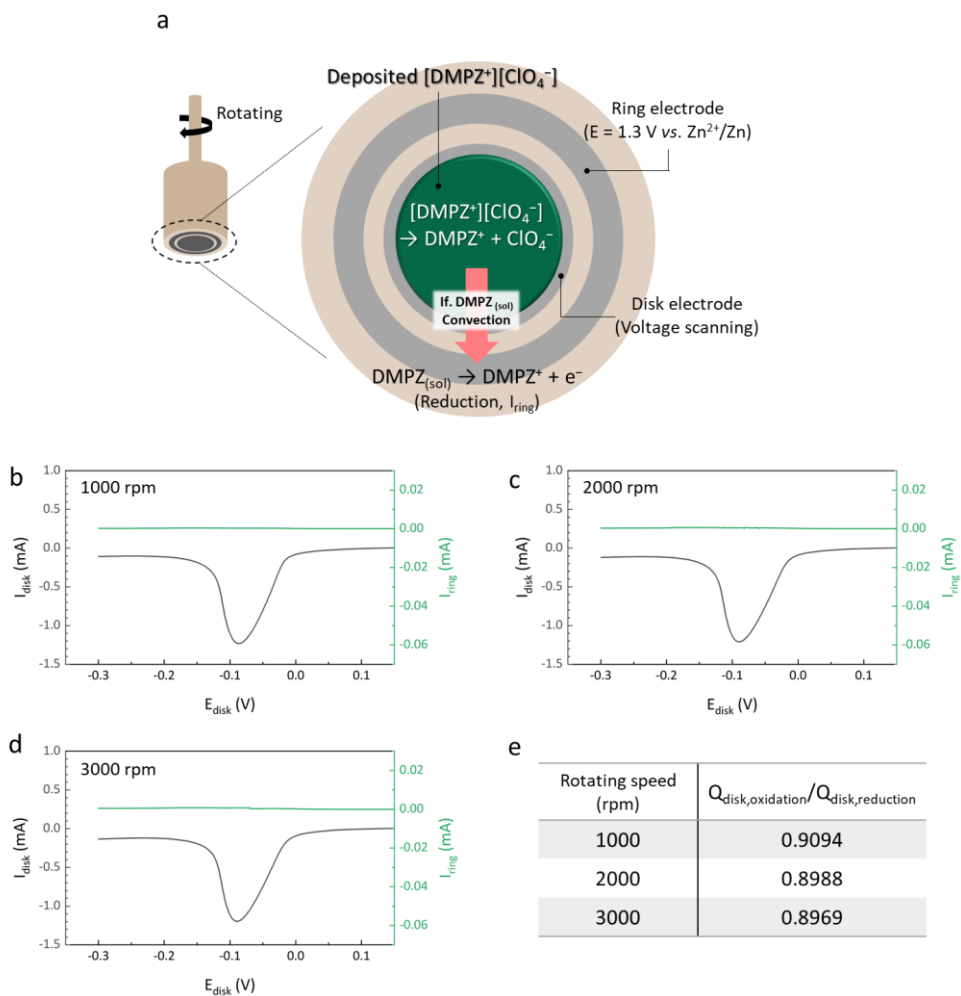


Figure 4.16. a. Schematic illustration of rotating ring disk electrode with $[\text{DMPZ}^+][\text{ClO}_4^-]$ deposited to the disk electrode and related reaction occurring at each electrode. b-d. Current response of RRDE experiment in 0.2 M $\text{Zn}(\text{ClO}_4)_2$ H_2O electrolyte with various rotating rate. b. 1,000 rpm. c. 2,000 rpm. d. 3,000 rpm. e. The ratio of oxidation charge to reduction charge in each rotation rate.

4.3.5 Proposed mechanism of *p*-type redox reaction

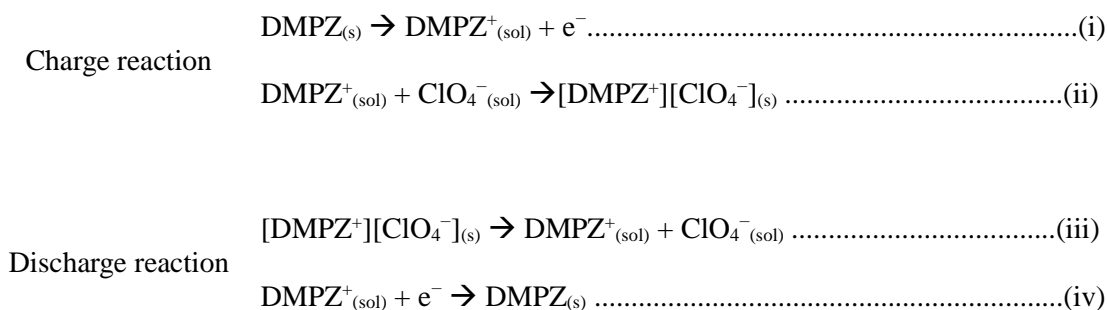
On the basis of the investigations in this work, we propose *p*-type redox mechanisms for DMPZ, as illustrated in Figure 4.17a. During the charging, DMPZ molecules on the particle surface are oxidized to DMPZ⁺, which then undergo electrolytic dissolution into the electrolyte. This is because DMPZ⁺ has a completely different conformation from DMPZ, making it unstable to be anchored in the rigid structure. Therefore, the state in which it is solvated by electrolyte molecules is energetically more stable, as DMPZ⁺ is soluble. The prominent hump at the beginning of charging in the charge/discharge profile (Figure 4.1c) indicates the overpotential due to this activation process to extricate DMPZ from the complete and stable surface structure. When the concentration of DMPZ^{+(sol)} near the particle surface reaches its solubility limit, DMPZ⁺ is precipitated with ClO₄⁻ in the electrolyte to form [DMPZ⁺][ClO₄⁻] nuclei. Because charged DMPZ has extremely low solubility of about 10⁻⁶ M, the DMPZ^{+(sol)} intermediate state only survives for a very short time. Solvated DMPZ⁺ is continuously produced as DMPZ⁺ precipitates, and [DMPZ⁺][ClO₄⁻] nuclei grow gradually as these solvated DMPZ⁺ precipitates on the surface of the preformed [DMPZ⁺][ClO₄⁻] nuclei. On the other hand, this process is reversed during discharge process. Solvated DMPZ⁺ is formed near the electrode due to the dissolution of the charge phase [DMPZ⁺][ClO₄⁻]. Since DMPZ⁺ in the [DMPZ⁺][ClO₄⁻] crystal requires a enormous activation energy to be reduced to DMPZ⁰ via conformational change in the dense solid, it is energetically preferable that solvated DMPZ⁺ be reduced on

the electrode surface instead. Neutral DMPZ is immediately precipitated to form nuclei, and these DMPZ nuclei gradually grow through continuous solution mediated reduction.

To explore the kinetic properties of the nucleation and growth process of $[\text{DMPZ}^+][\text{ClO}_4^-]$ and DMPZ in charge and discharge process, respectively, we conducted chronoamperometry experiment as displayed in Figure 4.18⁴⁶. The potential of 1.06 V *vs.* Zn^{2+}/Zn which is above the DMPZ oxidation potential was applied, and the current response was recorded to investigate the charge process. Figure 4.18a exhibits the exponentially increasing current response originating from the initial nucleation of $[\text{DMPZ}^+][\text{ClO}_4^-]$ and the subsequent decreasing current resulting from the overlap of neighboring nuclei at the maximum current (I_m). Figure 4.18b presents the current (I/I_m) and time (t/t_m) transients (CTT) curve which is regarded as a fit of four classical models of electrochemical deposition⁴⁷⁻⁴⁹. The current response from the DMPZ electrode shows the best fit to the three-dimensional instantaneous (3DI) nucleation and growth model, which indicates instantaneous nucleation and volume diffusional controlled growth. For the investigation of the discharge process, the potential of 0.87 V was applied to the electrode charged to 1.3 V at 10 mA g^{-1} (Figure 4.18c). As the charge process, CTT curve correspond to the nucleation and growth of DMPZ was best fit to 3DI model. Due to the solvated intermediate of $\text{DMPZ}^+_{(\text{sol})}$, DMPZ can be reconstructed during the charge and discharge through the solution mediation process along 3D directions and this experimental results agree well with the proposed mechanism in

Figure 4.17a⁵⁰.

We further explored the kinetic properties of the *p*-type reaction occurring through these multi-steps reactions. The overall reaction process of charge and discharge can be summarized as follows.



The notable difference is the reaction step where the charge transfer takes place. In the charge process, charge transfer reaction occurs via solid to solution state (reaction i), whereas it occurs via solution to solid state (reaction iv) in the discharge process. This asymmetry of the reaction leads to the difference in charge transfer kinetic during the redox reaction. To compare the distinct kinetics during the charge and discharge, we examined the exchange current of each reaction which could be obtained using Butler-Volmer equation. Figure 4.19a and b present the linear sweeping voltammetry using the half charged electrode and half discharged electrode, respectively. Using the Butler-Volmer equation, the exchange current (i_0) of each reaction was obtained through the tangent slope of the current-voltage plot at the point where overpotential is zero. As a result, the exchange

current of reduction reaction ($i_{0, \text{reduction}}$) was calculated one order higher than that of the oxidation reaction ($i_{0, \text{oxidation}}$). That is, the charge transfer kinetic of the reaction from solution to solid phase is greater than the reaction from solid to solution phase. This distinction affects the battery overpotential when it is operated at a high current rate. Figure 4.19c presents the average charge and discharge voltage when the DMPZ electrode is operated at various current rates in the range of 10-200 mA g⁻¹. It was confirmed that the increase of the overpotential with the increase of current rate is smaller for the discharge reaction than the charge reaction. In addition, comparing the overpotential of charge and discharge reaction at the GITT (galvanostatic intermittent titration technique) measurements as depicted in Figure 4.19d, the discharge overpotential was smaller than charge overpotential, verifying the faster charge transfer reaction during the discharge.

The DMPZ electrode allowed us to show an outstanding electrochemical performance based on the new understanding of the *p*-type redox reaction. The reversible capacity of 99 mAh g⁻¹ was obtained after a few initial activation cycles at a current density of 50 mA g⁻¹ (0.4C). Figure 4.20a presents the power capability of the electrode cycled at various current rates. The DMPZ electrode shows remarkable rate performance, delivering a specific capacity of 98, 96, 91, and 76 mAh g⁻¹ at the current density of 100, 200, 400, and 1,000 mA g⁻¹. Especially, the DMPZ electrode exhibited capacity utilization of 77% at a very high current rate of 1,000 mA g⁻¹ (7.9C) compared with that at 50 mA g⁻¹. Even at the high current rate, although the overpotential increases as the current rate increases, the charge-

discharge profile depicted in Figure 4.20b showed well maintained flat plateau, demonstrating the obtained capacity at high current rate is come from the redox reaction of DMPZ. It was generally accepted that the organic electrodes have poor rate capability because of their low electrical conductivity^{4,24}. However, according to the mechanism proposed in this study, because the charge transfer reaction occurs through the electrolytic dissolution of DMPZ at the surface, the reaction is unhindered by the bulk property of organic material, thereby resulting in a remarkable performance. The DMPZ electrode also exhibits exceptional cycle stability as illustrated in Figure 4.17c. When the electrode was cycled at a current rate of 300 mA g⁻¹ (2.4C), 70% of the initial capacity could be retained after 3,000 cycles, corresponding to the degradation rate of 0.012% per cycle, maintaining the flat charge/discharge profile (Figure 4.21). Through the XRD pattern (Figure 4.22a) and SEM image (Figure .22b) of the electrode after the 200th cycle, it was confirmed that the crystallinity of DMPZ and [DMPZ⁺][ClO₄⁻] was well maintained after the cycle, and the morphological changes also proceeded in the same way as the changes seen in the 1st cycle in Figure 4.6d,e. The coulombic efficiency was maintained above 99.5% over 3,000 cycles, demonstrating that the reorganization of DMPZ is highly reversible despite the drastic structural and morphological changes upon the redox reaction.

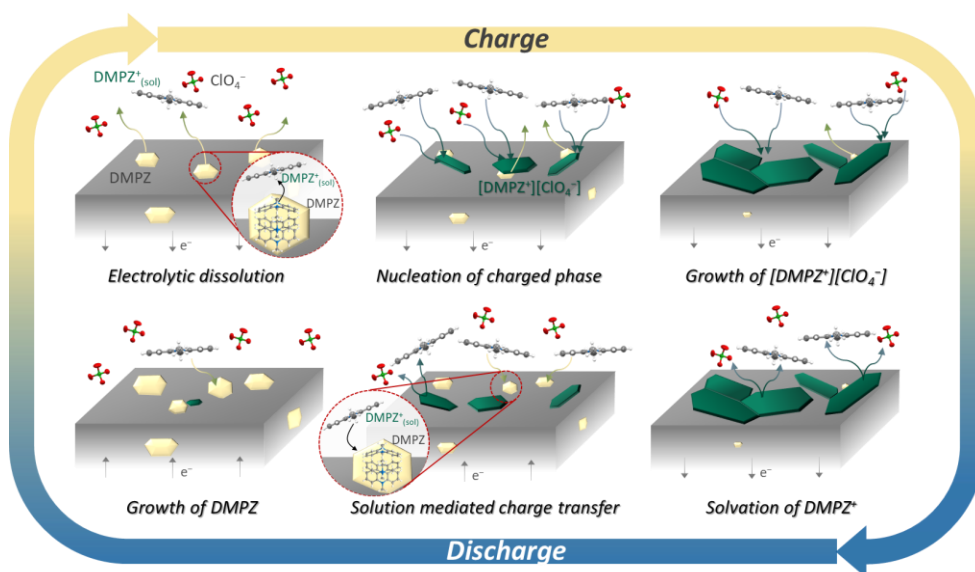
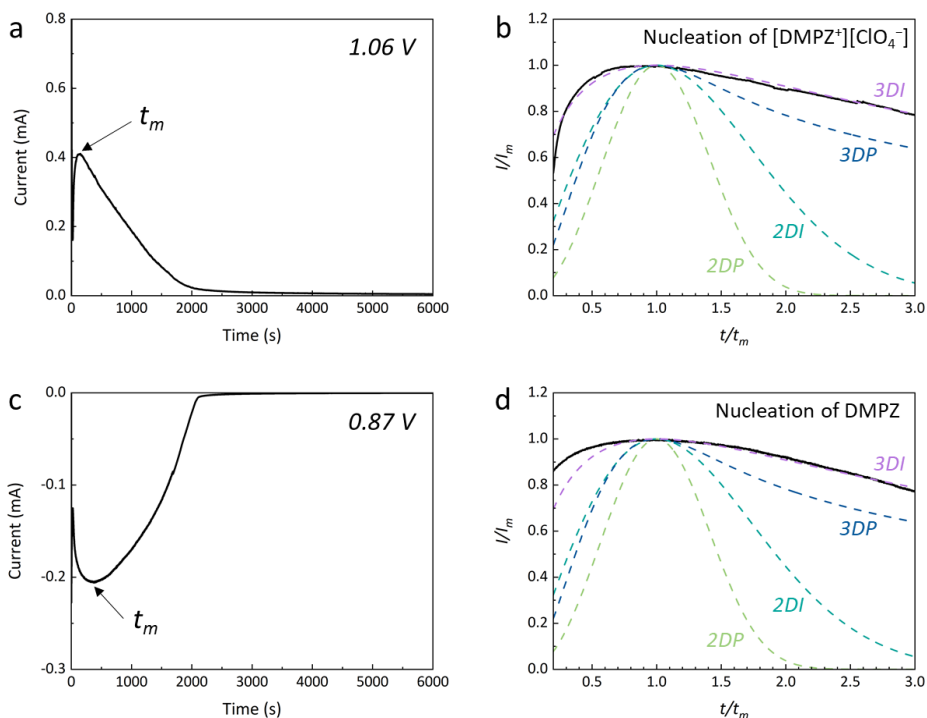


Figure 4.17. Proposed *p*-type redox mechanism of DMPZ. Schematic illustration of proposed *p*-type redox reaction for DMPZ. DMPZ at the particle surface undergoes electrolytic dissolution during the charging. Dissolved DMPZ^+ is precipitated and forms $[\text{DMPZ}^+][\text{ClO}_4^-]$ nuclei as it reaches its solubility limit near the surface. Precipitation facilitates additional dissolution of DMPZ^+ , enabling the continuous charging. The reaction proceeds as the $[\text{DMPZ}^+][\text{ClO}_4^-]$ grows continuously. For the discharge process, the dissolution of $[\text{DMPZ}^+][\text{ClO}_4^-]$ occurs first to produce the solvated DMPZ^+ intermediates. This solvated DMPZ^+ undergoes the solution mediated charge transfer reaction at the electrode and reduced DMPZ is immediately precipitated on the electrode. As the charge process, precipitation of DMPZ induces additional production of solvated DMPZ^+ , and the discharge reaction proceeds as the DMPZ nuclei grows.



e. Progressive: Density of nuclei increases with time

Instantaneous: Constant nuclei density (nucleation rate $\gg 1/t$)

2D growth: Incorporation of adatoms into the lattice interface (BFT models)

$$\frac{I}{I_m} = \left(\frac{t}{t_m}\right)^2 \exp\left[-\frac{2}{3}\left(\frac{t^3 - t_m^3}{t_m^3}\right)\right] \dots\dots 2DP$$

$$\frac{I}{I_m} = \left(\frac{t}{t_m}\right) \exp\left[-\frac{1}{2}\left(\frac{t^2 - t_m^2}{t_m^2}\right)\right] \dots\dots 2DI$$

3D growth: A volume diffusional controlled growth (SH models)

$$\frac{I}{I_m} = \left(\frac{1.2254}{t/t_m}\right)^{1/2} \left[1 - \exp\left(-\frac{2.3367 t^2}{t_m^2}\right)\right] \dots\dots 3DP$$

$$\frac{I}{I_m} = \left(\frac{1.9542}{t/t_m}\right)^{1/2} \left[1 - \exp\left(-\frac{1.2564 t}{t_m}\right)\right] \dots\dots 3DI$$

Figure 4.18. a. Chronoamperograms of DMPZ charging at 1.06 V (vs. Zn^{2+}/Zn) in 1 M $Zn(ClO_4)_2 \cdot H_2O$ electrolyte. b. Current (I/I_m) and time (t/t_m) plots of four classical models and experimental data for DMPZ at 1.06 V. c.

Chronoamperograms of $[\text{DMPZ}^+][\text{ClO}_4^-]$ which is made by charging DMPZ to 1.3 V (vs. Zn^{2+}/Zn) at 10 mA g^{-1} discharging at 0.87 V (vs. Zn^{2+}/Zn) in 1 M $\text{Zn}(\text{ClO}_4)_2$ H_2O electrolyte. d. Current ($\mathbf{I_m}$) and time ($\mathbf{t_m}$) plots of four classical models and experimental data for $[\text{DMPZ}^+][\text{ClO}_4^-]$ at 0.87 V. e. Four classical models of electrochemical deposition

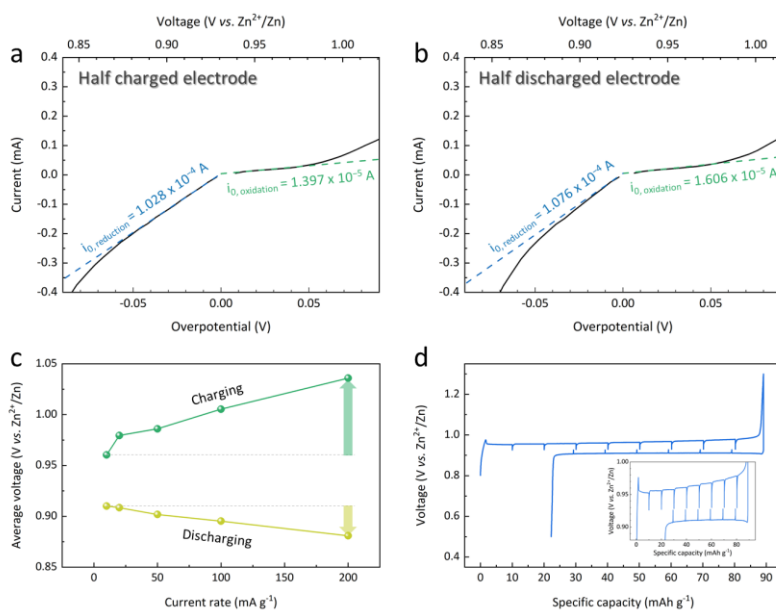


Figure 4.19. a, b. Current-overpotential profile of half charged electrode (a) and half discharged electrode (b) obtained through the linear sweep voltammetry to the positive and negative scan direction. The exchanged current was obtained based on the Butler-Volmer equation. If the overpotential η is small enough, the Butler-Volmer equation $i = i_0[\exp[-\alpha z F \eta / RT] - \exp[(1 - \alpha) z F \eta / RT]]$ to $i = -i_0 F \eta / RT$ according to the Taylor series. i : current, i_0 : exchange current, α : charge transfer coefficient, z : number of electrons involved in the reaction, F : Faraday constant, R : gas constant, T : absolute temperature, η : overpotential. Based on this simplified equation, the exchange current of oxidation and reduction reactions was obtained through the reciprocal of tangent slope at the point where overpotential is zero on each of the positive scan and negative scan curves. c. Average voltage of galvanostatic charge and discharge at various current rate. d. GITT profile of the DMPZ cell and its enlarged profile (inset).

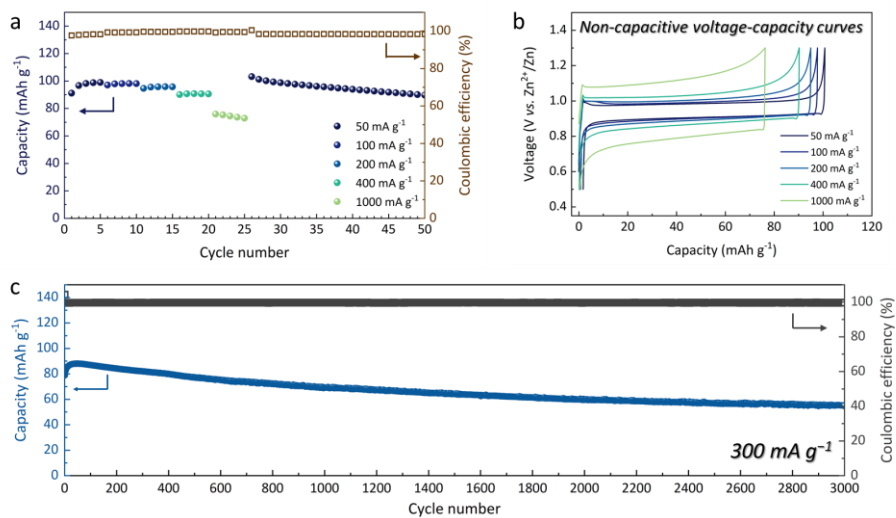


Figure 4.20. a. Capacity retention at various current densities from 50 mA g⁻¹ to 1,000 mA g⁻¹. b. Charge/discharge profile of DMPZ electrode at various current densities. c. Capacity retention and coulombic efficiency of DMPZ electrode at 300 mA g⁻¹.

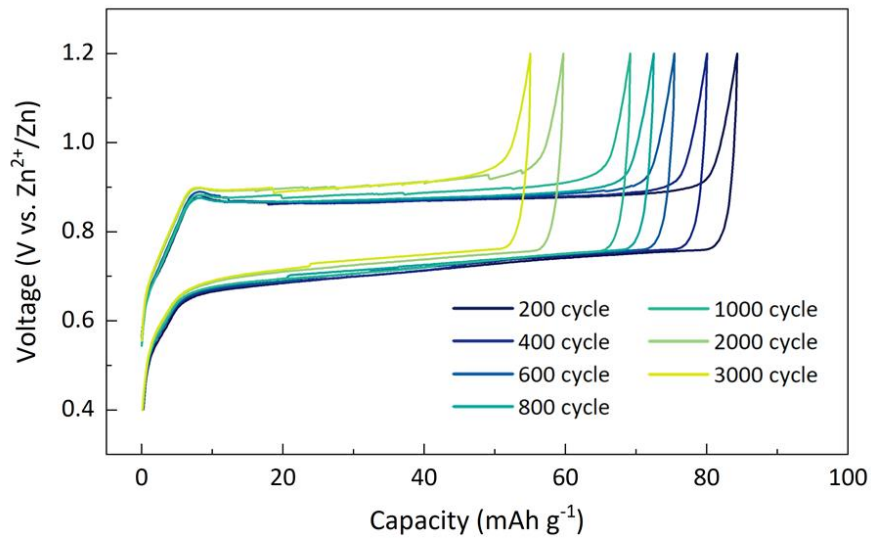


Figure 4.21. Charge/discharge profile of DMPZ electrode after prolonged cycles.

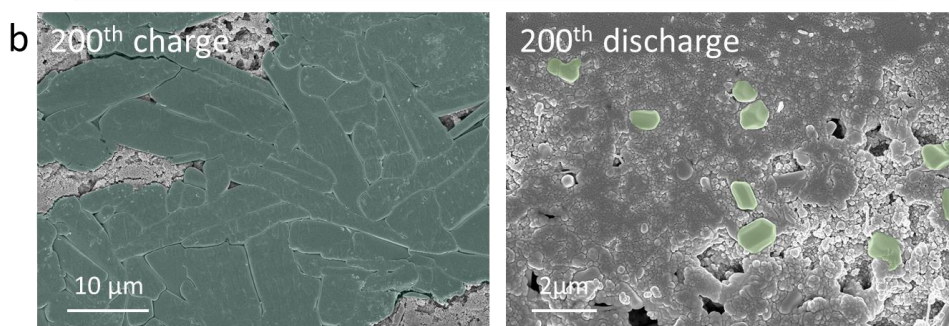
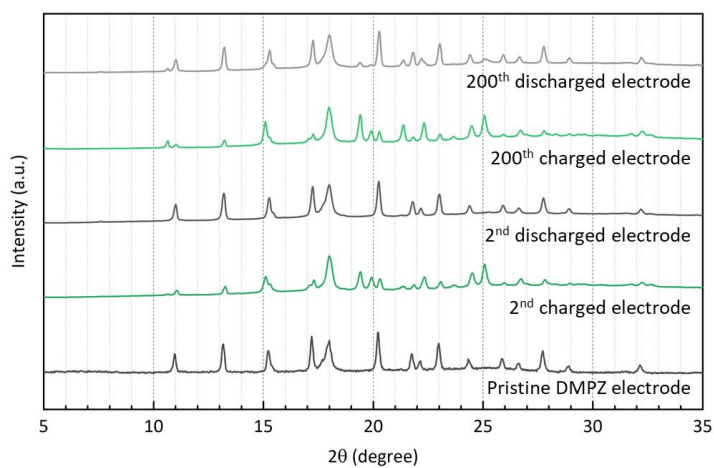


Figure 4.22. a. Ex situ XRD patterns of the electrode after 2nd and 200th charged and discharged. b. SEM images of the electrode after 200th charge and discharge.

4.4 Concluding remarks

We explored the *p*-type reaction mechanism that involves anion participation using in situ analysis. In situ and single crystal XRD analysis reveals that the *p*-type material undergoes the two-phase reaction, and most representative *p*-type materials have completely different crystallographic structures in their neutral phase and oxidized phase. We obtained further insight materializing such drastic structural change through the real-time monitoring of the *p*-type reaction of DMPZ that the reaction is based on the reorganization reaction. By confirming the intermediate state of solvated DMPZ^+ based on the RRDE test, we were able to conclude that the charging of *p*-type reaction occurs via the electrolytic dissolution followed by the precipitation of $[\text{DMPZ}^+][\text{ClO}_4^-]$, whereas dissolution of $[\text{DMPZ}^+][\text{ClO}_4^-]$ occurs prior to the solution-mediated charge transfer reaction of $\text{DMPZ}^+_{(\text{sol})}$ during the discharge of *p*-type reaction. Remarkable rate capability and high reversibility that exceeds the ordinary perception of organic materials could also be explained based on the proposed mechanism. This study reveals for the first time a mechanism for the *p*-type redox reaction that was veiled so far, thereby shedding light on the development and design of *p*-type organic materials with a high energy density that can replace conventional transition metal-based inorganic materials.

4.5 Reference

- 1 Turcheniuk, K., Bondarev, D., Singhal, V. & Yushin, G. Ten years left to redesign lithium-ion batteries. *Nature* **559**, 467-470, (2018).
- 2 Lee, S. & Manthiram, A. Can Cobalt Be Eliminated from Lithium-Ion Batteries? *ACS Energy Lett.* **7**, 3058-3063, (2022).
- 3 Poizot, P. *et al.* Opportunities and Challenges for Organic Electrodes in Electrochemical Energy Storage. *Chem. Rev.* **120**, 6490-6557, (2020).
- 4 Lu, Y. & Chen, J. Prospects of organic electrode materials for practical lithium batteries. *Nat. Rev. Chem.* **4**, 127-142, (2020).
- 5 Poizot, P., Dolhem, F. & Gaubicher, J. Progress in all-organic rechargeable batteries using cationic and anionic configurations: Toward low-cost and greener storage solutions? *Curr. Opin. Electrochem.* **9**, 70-80, (2018).
- 6 Kim, J. *et al.* Organic batteries for a greener rechargeable world. *Nat. Rev. Mater.*, (2022).
- 7 Kye, H., Kang, Y., Jang, D., Kwon, J. E. & Kim, B.-G. p-Type Redox-Active Organic Electrode Materials for Next-Generation Rechargeable Batteries. *Adv. Energy Sustainability Res.* **3**, 2200030, (2022).
- 8 Lee, S. *et al.* Utilizing Latent Multi-Redox Activity of p-Type Organic Cathode Materials toward High Energy Density Lithium-Organic Batteries. *Adv. Energy Mater.* **10**, 2001635, (2020).
- 9 Kolek, M. *et al.* Ultra-high cycling stability of poly(vinylphenothiazine) as a battery cathode material resulting from π - π interactions. *Energy Environ.*

- Sci.* **10**, 2334-2341, (2017).
- 10 Lee, M. *et al.* Multi-electron redox phenazine for ready-to-charge organic batteries. *Green Chem.* **19**, 2980-2985, (2017).
- 11 Lee, K. *et al.* Phenoxazine as a high-voltage p-type redox center for organic battery cathode materials: small structural reorganization for faster charging and narrow operating voltage. *Energy Environ. Sci.* **13**, 4142-4156, (2020).
- 12 Deunf, É. *et al.* Reversible anion intercalation in a layered aromatic amine: a high-voltage host structure for organic batteries. *J. Mater. Chem. A* **4**, 6131-6139, (2016).
- 13 Deunf, É., Jiménez, P., Guyomard, D., Dolhem, F. & Poizot, P. A dual-ion battery using diamino-rubicene as anion-inserting positive electrode material. *Electrochem. Commun.* **72**, 64-68, (2016).
- 14 Luo, Y. *et al.* A High-Power Aqueous Zinc–Organic Radical Battery with Tunable Operating Voltage Triggered by Selected Anions. *ChemSusChem* **13**, 2239-2244, (2020).
- 15 Wang, J. *et al.* Conjugated sulfonamides as a class of organic lithium-ion positive electrodes. *Nat. Mater.* **20**, 665-673, (2021).
- 16 Wei, Z. *et al.* Reversible intercalation of methyl viologen as a dicationic charge carrier in aqueous batteries. *Nat. Commun.* **10**, 3227, (2019).
- 17 Sieuw, L. *et al.* Through-Space Charge Modulation Overriding Substituent Effect: Rise of the Redox Potential at 3.35 V in a Lithium-Phenolate

- Stereoelectronic Isomer. *Chem. Mater.* **32**, 9996-10006, (2020).
- 18 Bernard, L. *et al.* Influence of Polymorphism on the Electrochemical Behavior of Dilithium (2, 3-Dilithium-oxy)-terephthalate vs. Li. *Inorganics* **10**, 62, (2022).
- 19 Padhi, A. K., Nanjundaswamy, K. S., Masquelier, C., Okada, S. & Goodenough, J. B. Effect of Structure on the $\text{Fe}^{3+} / \text{Fe}^{2+}$ Redox Couple in Iron Phosphates. *J. Electrochem. Soc.* **144**, 1609-1613, (1997).
- 20 Padhi, A. K., Nanjundaswamy, K. S. & Goodenough, J. B. Phospho-olivines as Positive-Electrode Materials for Rechargeable Lithium Batteries. *J. Electrochem. Soc.* **144**, 1188-1194, (1997).
- 21 Scharner, S., Weppner, W. & Schmid-Beurmann, P. Evidence of Two-Phase Formation upon Lithium Insertion into the $\text{Li}_{1.33}\text{Ti}_{1.67}\text{O}_4$ Spinel. *J. Electrochem. Soc.* **146**, 857-861, (1999).
- 22 Li, D. & Zhou, H. Two-phase transition of Li-intercalation compounds in Li-ion batteries. *Mater. Today* **17**, 451-463, (2014).
- 23 Song, Z. & Zhou, H. Towards sustainable and versatile energy storage devices: an overview of organic electrode materials. *Energy Environ. Sci.* **6**, 2280-2301, (2013).
- 24 Lee, S. *et al.* Recent Progress in Organic Electrodes for Li and Na Rechargeable Batteries. *Adv. Mater.* **30**, 1704682, (2018).
- 25 Dai, G. *et al.* Manipulation of conjugation to stabilize N redox-active centers for the design of high-voltage organic battery cathode. *Energy*

- Storage Mater.* **16**, 236-242, (2019).
- 26 Huang, L. *et al.* π -Extended Dihydrophenazine-Based Polymeric Cathode Material for High-Performance Organic Batteries. *ACS Sustain. Chem. Eng.* **8**, 17868-17875, (2020).
- 27 Peterson, B. M., Gannett, C. N., Melecio-Zambrano, L., Fors, B. P. & Abruña, H. Effect of Structural Ordering on the Charge Storage Mechanism of p-Type Organic Electrode Materials. *ACS Appl. Mater. Interfaces* **13**, 7135-7141, (2021).
- 28 Otteny, F. *et al.* Poly(vinylphenoxazine) as Fast-Charging Cathode Material for Organic Batteries. *ACS Sustain. Chem. Eng.* **8**, 238-247, (2020).
- 29 Speer, M. E. *et al.* Thianthrene-functionalized polynorbornenes as high-voltage materials for organic cathode-based dual-ion batteries. *Chem. Commun.* **51**, 15261-15264, (2015).
- 30 Kim, J. *et al.* A p-n fusion strategy to design bipolar organic materials for high-energy-density symmetric batteries. *J. Mater. Chem. A* **9**, 14485-14494, (2021).
- 31 Crouse, J. D., Nielsen, L. B., Jørgensen, S., Kjaergaard, H. G. & Wennberg, P. O. Autoxidation of Organic Compounds in the Atmosphere. *J. Phys. Chem. Lett.* **4**, 3513-3520, (2013).
- 32 Holzapfel, M., Lambert, C., Selinka, C. & Stalke, D. Organic mixed valence compounds with N,N-dihydrodimethylphenazine redox centres. *J.*

- Chem. Soc., Perkin trans. II*, 1553-1561, (2002).
- 33 B. Araujo, R., S. de Almeida, J., Ferreira da Silva, A. & Ahuja, R. Insights in the electronic structure and redox reaction energy in LiFePO₄ battery material from an accurate Tran-Blaha modified Becke Johnson potential. *J. Appl. Phys.* **118**, 125107, (2015).
- 34 Hu, J., Huang, W., Yang, L. & Pan, F. Structure and performance of the LiFePO₄ cathode material: from the bulk to the surface. *Nanoscale* **12**, 15036-15044, (2020).
- 35 Batail, P., Boubekour, K., Fourmigué, M. & Gabriel, J.-C. P. Electrocrystallization, an Invaluable Tool for the Construction of Ordered, Electroactive Molecular Solids. *Chem. Mater.* **10**, 3005-3015, (1998).
- 36 Antonello, S., Dainese, T., Pan, F., Rissanen, K. & Maran, F. Electrocrystallization of Monolayer-Protected Gold Clusters: Opening the Door to Quality, Quantity, and New Structures. *J. Am. Chem. Soc.* **139**, 4168-4174, (2017).
- 37 Van der Ven, A., Bhattacharya, J. & Belak, A. A. Understanding Li Diffusion in Li-Intercalation Compounds. *Acc. Chem. Res.* **46**, 1216-1225, (2013).
- 38 Chen, G., Song, X. & Richardson, T. J. Electron Microscopy Study of the LiFePO₄ to FePO₄ Phase Transition. *Electrochem. Solid State Lett.* **9**, A295, (2006).
- 39 Lim, J. *et al.* Origin and hysteresis of lithium compositional

- spatiodynamics within battery primary particles. *Science* **353**, 566-571, (2016).
- 40 Malifarge, S., Delobel, B. & Delacourt, C. Quantification of preferred orientation in graphite electrodes for Li-ion batteries with a novel X-ray-diffraction-based method. *J. Power Sources* **343**, 338-344, (2017).
- 41 Ruetschi, P. Review on the lead—acid battery science and technology. *J. Power Sources* **2**, 3-120, (1977).
- 42 Yang, J. *et al.* Review on the research of failure modes and mechanism for lead—acid batteries. *Int. J. Energy Res.* **41**, 336-352, (2017).
- 43 Sauer, D. U. *et al.* Charging performance of automotive batteries—An underestimated factor influencing lifetime and reliable battery operation. *J. Power Sources* **168**, 22-30, (2007).
- 44 Antao, S. M. Structural trends for celestite (SrSO₄), anglesite (PbSO₄), and barite (BaSO₄): Confirmation of expected variations within the SO₄ groups. *Am. Mineral.* **97**, 661-665, (2012).
- 45 Takehara, Z.-i. Dissolution and precipitation reactions of lead sulfate in positive and negative electrodes in lead acid battery. *J. Power Sources* **85**, 29-37, (2000).
- 46 Paunovic, M. & Schlesinger, M. *Fundamentals of electrochemical deposition.* (john wiley & sons, 2006).
- 47 Bewick, A., Fleischmann, M. & Thirsk, H. Kinetics of the electrocrystallization of thin films of calomel. *Trans. Faraday Soc.* **58**,

- 2200-2216, (1962).
- 48 Scharifker, B. & Hills, G. Theoretical and experimental studies of multiple nucleation. *Electrochim. Acta* **28**, 879-889, (1983).
- 49 Scharifker, B., Rugeles, R. & Mozota, J. Electrocrystallization of copper sulphide (Cu₂S) on copper. *Electrochim. Acta* **29**, 261-266, (1984).
- 50 Li, Z., Zhou, Y., Wang, Y. & Lu, Y.-C. Solvent-Mediated Li₂S Electrodeposition: A Critical Manipulator in Lithium–Sulfur Batteries. *Adv. Energy Mater.* **9**, 1802207, (2019).

Chapter 5. Conclusion

Growing concerns about global environmental pollution have triggered the development of sustainable and eco-friendly energy storage chemistries. Conventional lithium-ion batteries have achieved a great deal of success in meeting the growing energy demand as a representative energy storage system in recent decades. However, since the main components rely on transition metals such as cobalt and nickel, the search for alternatives to address the environmental and sustainability problems has been vigorously devoted. In that regard, organic rechargeable batteries are considered promising next-generation systems that could meet the demands of this age. Since the research of organic rechargeable batteries is still immature compared to the inorganic-based system, a systematic research approach is required from strategic ROM design to expand the utility of ROMs to fundamental study for the groundbreaking leap of the performance of organic rechargeable batteries. In this thesis, systematic research was conducted to promote the development of eco-friendly organic rechargeable batteries.

Exploring new ROMs is the first step of the systematic development process. When searching for appropriate materials, I focused on the biological energy transduction system. Since it shares an identical fundamental working principle of reversible electron transfer with a rechargeable battery system, redox cofactors involved in the electron transport system in the cell ensure the reversibility to be used as ROMs. Among various redox cofactors, the well-known

nicotinamide cofactor, which had not been utilized as a ROM because the redox center part was not neutral as other redox motifs, was explored for the first time. Through the molecular modification process, a nicotinamide cofactor-inspired new redox motif, mNAD was designed. Especially, the anion anchoring process was the key step that enables us to preserve a positive charge and successfully mimic the redox reaction of nicotinamide cofactor. All the mNAD-X series in combination with various halide anions were successfully introduced, showing reversible capacities in a lithium-ion battery, and its reversibility was demonstrated by the combined calculation and experimental analysis. The new approach presented in this study opened up the possibility for the discovery of unexplored ROMs.

For the next step of the advancement of eco-friendly rechargeable batteries, an all-organic battery system was developed. In addition to the greenness of organic material itself, I attempted to exploit a symmetric battery system that can significantly reduce the electrode manufacturing process in half utilizing the unique ROM groups of bipolar-type materials that can be simultaneously used as anode and cathode. However, the limitation of the symmetric batteries reported so far was a low cell voltage. To solve this problem, a molecular redesign strategy was devised to design bipolar ROMs with a large HOMO/LUMO gap. Through the direct fusion to expand the conjugation of each *p*-type redox motif with electron-donating nature and *n*-type redox motif with electron-withdrawing nature, the new bipolar-type ROMs were designed. A new PNZTA, a combination of phenazine and thiantherene was synthesized and it showed bipolar redox activity with lower

reduction potential and higher oxidation potential than that of phenazine and thianthrene, respectively. Finally, the symmetric cell with a PNZTA electrode exhibited improved operating potential, capacity, and cycling stability that the cell with each monomer and it was fairly high voltage among the reported symmetric batteries. This simple and universal approach of fusion provides a novel strategy for the design of outperforming bipolar materials.

As well as discovering and renovating the ROMs, understanding the scientific aspects of electrochemical reactions occurring in battery systems is crucial. However, there is a lack of in-depth studies on the reaction mechanism of *p*-type ROMs, which have been in the spotlight recently due to their intrinsically high voltage. Since *p*-type ROMs involve the insertion of anions during the reaction, insight into how large anions such as perchlorate and hexafluorophosphate interact with organic structure may play an important role in determining the performance of *p*-type organic batteries. To uncover the reaction mechanism in the battery of *p*-type ROMs, combined multi-scale in situ monitoring was conducted with DMPZ electrode which is a representative of *p*-type ROM to directly observe the electrochemical reaction. Through in situ X-ray diffraction, single crystal X-ray diffraction analysis, and in situ optical microscope monitoring, it was revealed that *p*-type ROMs undergo the redox reaction through an electrolytic dissolution followed by the nucleation and growth process. Owing to the lattice reconstruction process based on the intermediate solvated charged phase, unexpected superior rate capability was also demonstrated with DMPZ electrode.

This foundational study could serve as the first step of the guideline to strategically design and develop a best-performing *p*-type organic cathode material.

In this dissertation, multidisciplinary research strategy, 1) exploring new ROMs, 2) redesigning ROMs, and 3) in-depth studying of the basic reaction mechanism with the aim of developing eco-friendly organic rechargeable batteries was introduced. Although there are still remaining challenges for the practical application, I expect that all of the approaches and efforts described in this dissertation will contribute to the advancement of next-generation energy storage systems and provide significant research insight for the scientific understanding of organic rechargeable batteries.

국 문 초 록

최근 급증하는 에너지 수요와 가속화되는 환경 문제를 해결하기 위해 전세계적으로 탄소중립이 주요 화두로 떠오른 가운데, 화석연료에서 태양력, 풍력 및 수력 발전과 같은 재생 가능한 에너지 원으로의 에너지 전환을 시도하고 있다. 이러한 재생 에너지는 간헐적으로 생산되는 특징으로 인해 에너지 저장 시스템이 필연적으로 필요하다. 이 중 리튬이온 배터리는 높은 에너지 밀도와 뛰어난 수명 안정성을 가지고 있어 휴대용 기기에서 대용량 에너지 저장 장치에 이르기까지 다양한 분야에서 활용되고 있는 핵심 에너지 저장 기술이다. 하지만 종래의 이차전지의 핵심 양극 소재인 전이금속 산화물은 니켈, 코발트와 같이 한정된 원재료를 사용하고 있어 자원 무기화로 인한 가격 폭등 위험에 노출되어 있을 뿐만 아니라, 무거운 중량으로 인해 에너지 밀도 향상에 한계가 있어 최근 지속 가능성에 대한 우려가 커지고 있다. 이로 인해 전이금속을 포함하지 않는 에너지 저장 시스템 개발에 대한 관심이 높아지고 있으며, 산화 환원 활성 유기 물질을 활물질로 사용하는 유기 이차전지가 유망한 대안으로 떠오르고 있다. 유기 전극 소재는 원료 수급에 제한이 적고 생산 및 재활용 과정에서 발생하는 온실 가스의 양이 전이금속 산화물 소재에 비해 현저히 적을 뿐만 아니라 화학적 개조 가능성으로

그 활용도를 확장시킬 수 있다는 장점이 있어 지속 가능한 친환경 전지 시스템으로 각광 받고 있다.

본 학위 논문에서는 친환경적인 고성능의 유기물 이차 전지를 개발하기 위해, 새로운 산화환원 활성 모티프의 발굴 및 설계를 위한 소재 디자인 전략을 제안한다. 또한 유기 이차 전지의 도약을 위해 실시간 분석 기법을 사용하여 유기 활물질의 전기 화학 반응 메커니즘에 대한 기초 연구를 수행한다.

2장에서는 새로운 산화환원 활성 유기 물질을 개발하기 위한 분자 설계 전략을 소개한다. 생물학적 에너지 트랜스덕션 과정과 이차 전지의 에너지 저장 시스템 사이의 유사성에 영감을 받아 잘 알려진 산화환원 보조인자인 니코틴아미드 아데닌 다이뉴클레오타이드(nicotinamide adenine dinucleotide)의 활성 모티프를 이차전지의 산화환원 활성 물질로 응용하였다. 전하를 띠고 있는 니코틴 아마이드 보조 인자의 모티프를 음이온으로 고정함으로써 리튬 이온 이차전지 시스템에서 활성 전극 역할을 할 수 있음을 입증하였다. 이 장에서는 자연계의 산화환원 활성 모티프를 모방하여 에너지 저장 소재를 개발하는 새로운 접근 방식을 보여 준다.

3장에서는 보다 더 친환경적인 고성능 유기 이차 전지의 개발을 위한 분자 설계 전략을 도입한다. 전-유기(all-organic) 대칭 전지는 양극과 음극에 동일한 유기 재료를 사용하는 시스템으로, 생산 비용을 현저

하게 절감하여 환경 측면에서 유리한 시스템이다. 그러나 대부분의 대칭형 이차전지는 산화 반응과 환원 반응 사이의 전위차가 작기 때문에 낮은 전압을 갖고 있다. 이 장에서는 환원 반응과 산화 반응의 전위차가 큰 양극성 물질을 만들기 위한 새로운 분자 설계 전략인 p-n 융합을 제안했다. p형과 n형 산화 환원 모티프의 파이 전자 시스템을 직접 결합 시킴으로써 상호 간의 전자 섭동 효과를 극대화시킬 수 있었다. 융합된 분자는 단독의 p형 물질보다 더 낮은 HOMO 에너지 준위, 단독의 n형 물질보다 더 높은 LUMO 에너지 준위를 나타냄을 제일 원리 계산을 통해 증명하였다. 계산 결과를 바탕으로 제작한 화합물인 새로운 PNZTA는 이차전지 시스템에서 성공적인 양극성 활성을 나타냄을 확인하였다. 더욱이, PNZTA를 활용한 대칭 전지의 작동 전압은 각 단독 n형, p형 물질로 제작된 전지의 전압보다 향상되었음을 확인하였다.

4장에서는 다양한 실시간 분석 기술을 도입하여 p형 산화 환원 활성 물질의 반응 메커니즘을 규명하였다. P형 유기 소재는 기존의 전이 금속 산화물 소재에 견줄 만한 높은 전압을 갖고 있어 최근 주목받고 있는 소재군이다. p형 유기물은 산화 반응을 먼저 진행하며 양전하를 띠게 되기 때문에 리튬 또는 나트륨 대신 과염소산염, 육불화인산염과 같이 크기가 큰 음이온이 전하 보상을 위해 반응에 참여한다. 실시간 관찰 분석 기술을 사용하여 부피가 큰 음이온이 전극 구조 내에 어떻게 삽입되는지에 대한 반응 메커니즘을 처음으로 규명하였다. 반응 과정에서의 구

조적·형태학적 변화를 모니터링한 결과를 바탕으로, 유기 분자는 산화 환원 과정에서 분자의 형태 변화를 겪게 되고, 이로 인해 단순한 음이온 삽입 반응으로 유기 전극의 충·방전이 진행되는 것이 아니라, 용매화된 중간상을 거치면서 반응이 진행됨을 밝혔다. 이 학위 논문에서 진행된 유기물 이차 전지의 설계 전략 및 기초적 에너지 저장 과정에 대한 심층적 분석은 유기물 이차전지 시스템을 이해하기 위한 학문적 통찰력을 제공하고 고성능의 유기물 이차전지 개발에 대한 가이드 라인을 제시해 줄 것이다.

주요어: 이차 전지, 유기물 이차 전지, 산화 환원 유기물, 전기 화학, 유기 화학

학 번: 2017-22566